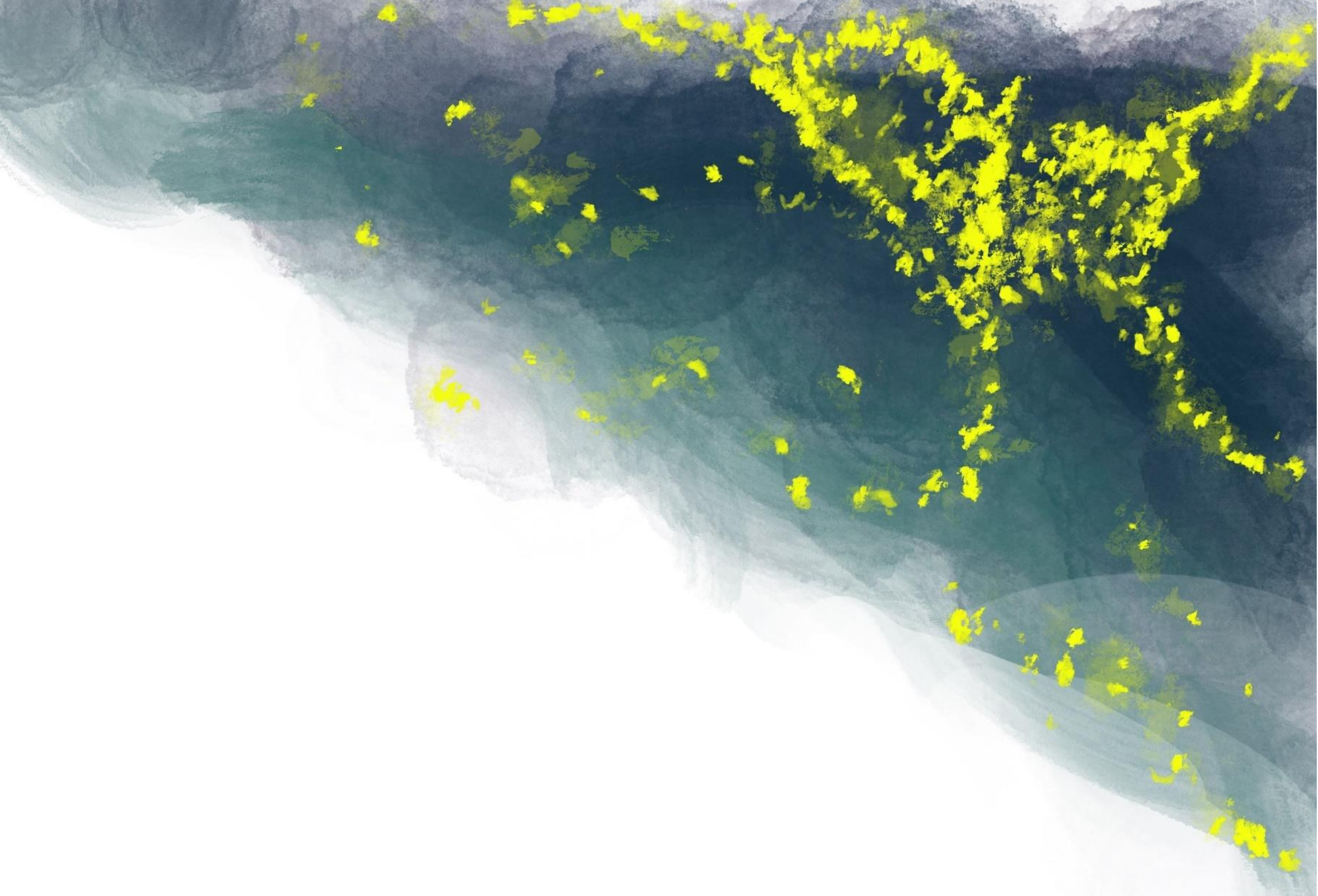

Radiolabelling, monitoring and preclinical evaluation of urease-powered nanomotors as potential theranostic agent for bladder cancer

Cristina Simó Costa

eman ta zabal zazu

Universidad
del País Vasco

Euskal Herriko
Unibertsitatea

Donostia 2022

CIC biomaGUNE
MEMBER OF BASQUE RESEARCH
& TECHNOLOGY ALLIANCE

EXCELENCIA
MARÍA
DE MAEZTU
07/2018 - 06/2022

eman ta zabal zazu
Universidad del País Vasco
Euskal Herriko Unibertsitatea

Radiolabelling, monitoring and preclinical evaluation of urease-powered nanomotors as potential theranostic agent for bladder cancer

PhD thesis

to obtain the Doctor of Philosophy degree
in *Synthetic and Industrial Chemistry*
at the University of the Basque Country (UPV/EHU)

by

Cristina Simó Costa

Donostia 2022

Thesis supervisors: Dr. Jordi Llop Roig (Radiochemistry and Nuclear Imaging Group, CIC biomaGUNE) and Dr. Sergio Enrique Moya (Soft Matter Nanotechnology Group, CIC biomaGUNE)

University Tutor: Dr. María Esther Lete Expósito (Department of Organic Chemistry II, Faculty of Science and Technology, University of the Basque Country (UPV/EHU))

List of Abbreviations and Acronyms

APTES	3-aminopropyl)triethoxysilane
ATP	Adenosine Triphosphate
AuNP	Gold Nanoparticle
BC	Bladder Cancer
BCG	Bovis Bacillus Calmette-Guérin
BFC	Bifunctional Chelator
BSA	Bovine Serum Albumin
CT	Computed Tomography
CTAB	Hexadecyltrimethylammonium bromide
DNA	Deoxyribonucleic acid
DLS	Dynamic Light Scattering
EPR	Enhanced Permeability and Retention
FAP	Fibroblast Activation Protein
FDA	Food and Drug Administration
FDG	Fluorodeoxyglucose
FITC	Fluorescein Isothiocyanate
FL	Fluorescence
GA	Glutaraldehyde
GOx	Glucose Oxidase
HPMA	*N*-(2-hydroxypropyl)methacrylamine
ICP-MS	Inductively Coupled Plasma Mass Spectrometry
I.V.	Intravenous
I. Vesic.	Intravesical
LET	Linear Energy Transfer
LOR	Line of Response
MB49	Murine Bladder Cell Carcinoma
MIBC	Muscle-Invasive Bladder Cancer
MMC	Mitomycin C
MNM	Micro- and Nanomotor

MPS	Mononuclear Phagocyte System
MRI	Magnetic Resonance Imaging
MSNP	Mesoporous Silica Nanoparticle
NP	Nanoparticle
NMIBC	Non-Muscle-Invasive Bladder Cancer
NTV	Normalised Tumour Volum
PA	Photoacoustic
PBS	Phosphate Buffer Saline
PEG	Polyethyleneglycol
PET	Positron Emission Tomography
PSMA	Prostate-Specific Membrane Antigen
Radio-HPLC	Radio-High-Performance Liquid Chromatography
Radio-TLC	Radio-Thin Layer Chromatography
RES	Reticuloendothelial system
RF	Radiofrequency
RNT	Radionuclide Therapy
SE-DWI	Spin-Echo based Diffusion Weighted Imaging
SPECT	Single Positron Emission Computed Tomography
SSTR	Somatostatin Receptor
$T_{1/2}$	Half-life
TEM	Transmission Electron Microscopy
TEOA	Triethanolamine
TEOS	Tetraethyl orthosilicate
TFA	Trifluoroacetic Acid
T stage	Depth Tumour Invasion
US	Ultrasound
VOI	Volume of Interest
WHO	World Health Organization

Table of Content

Summary

According to the World Health Organization (WHO), cancer is one of the major causes of death worldwide. Bladder cancer (BC) is the ninth most common malignancy with at least half a million of cases diagnosed globally each year. Despite having a survival rate of 77%, conventional treatments based on transurethral resection of the bladder tumour, followed by intravesical instillation of immunotherapeutic and/or chemotherapeutic drugs, are not highly effective since recurrence appears in the 30-70% of the patients within 5 years. Limitations of this local administration are related to the lower permeability of the urothelium, making it difficult to drugs to reach the tumour tissue, or drug dilution due to the entrance of fresh urine. Therefore, new therapeutic approaches are required to improve specificity and minimize recurrence and progression.

The recent emergence of nanotechnology has opened new strategies for the development of nanomaterials systems to increase therapeutic efficacy and minimize side effects in cancer treatment. In this context, nanomaterials can be designed to improve stability, circulation time, and preferentially accumulate at the target site. Nevertheless, penetration on tissues and cellular barriers is a major challenge that need to be addressed as it is reported that only 0.7% of the injected nanomaterials reach their target *in vivo* after parenteral administration. In this sense, micro- and nanomotors (MNMs) have emerged as a new generation of nano-size drug delivery systems, which combine the properties of traditional nanocarriers with the capacity to self-propel in a specific media. Particularly, enzyme-powered nanomotors have gained much attention to be used in biomedical applications since their propulsion is promoted by biocompatible fuels. For instance, urease-powered nanomotors have a huge potential as drug delivery systems for the diagnosis and/or treatment of bladder cancer since their motion is promoted by the conversion of urea (present in urine) into carbon dioxide and ammonia.

In the current PhD thesis, we have worked on the development of radiolabelling strategies to enable the visualization of urease-powered nanomotors using nuclear imaging techniques, and on assessing the tumour accumulation and therapeutic capacity of urease-powered nanomotors when their self-propelling capacities are active in an orthotopic mouse model of bladder cancer.

The work performed in this PhD thesis has been divided in three main parts, which result in the three experimental chapters. Firstly, we worked on the development of two radiolabelling strategies to incorporate fluorine-18 (^{18}F) and iodine-124 (^{124}I) to the urease nanomotors structure. Then, *in vitro* monitor of both ^{18}F-urease and ^{124}I-urease nanomotors was investigate using Positron Emission Tomography (PET) imaging in water (not self-propelled capacity) and urea solution (active self-propelled capacity). The resulting PET imaging obtained in 3D phantoms revealed a prominent effect on the motion of urease nanomotors in the presence of urea solution. The *in vivo* biodistribution and stability of ^{18}F-urease and ^{124}I-urease nanomotors was investigated after intravenous administration in healthy mice, showing the suitability of PET imaging to track nanomotors *in vivo* and that radiolabelling strategy with ^{18}F was more convenient because of their *in vivo* radiochemical stability. A mixing effect resulting in a homogenous distribution within a healthy bladder was observed upon intravesical administration of ^{18}F-urease nanomotors in urea. These results are included in Chapter 3.

In view of the promising results obtained in Chapter 3, the second part of the PhD thesis was focused on the evaluation of the capacity of urease nanomotors to accumulate in tumour tissue using an orthotopic mouse model of bladder cancer. Hence, female mice were inoculated with a murine bladder cell carcinoma (MB49) to develop tumour within the bladder. Magnetic Resonance Imaging (MRI) was used to evaluate the presence and growth of the tumour within the bladder, proving the usefulness of the technique to monitor tumour size. PET imaging was conducted after intravesical administration of ^{18}F-urease nanomotors and controls, confirming the higher tumour uptake for ^{18}F-urease nanomotors when urea was used as the vehicle. Complementary *ex vivo* techniques, such as Inductively Coupled Plasma-Mass Spectrometry (ICP-MS), histological analysis and immunofluorescence, were applied to corroborate *in vivo* PET results. Moreover, immunofluorescence showed tumour penetration of urease nanomotors administered in urea. These results are described in Chapter 4.

Due to the increased tumour accumulation of urease nanomotors when urea is used as vehicle in bladder tumour, the last part of the PhD thesis pursued the possibility of using urease nanomotors as carriers for the radionuclide therapy. With that aim, a radiolabelling strategy to incorporate iodine-131 (^{131}I) to urease nanomotors was developed. Bladder tumour-bearing animals were randomised for subsequent radiotherapy studies according to tumour size as determined by MRI. Single Positron Emission Computed Tomography (SPECT) acquisitions were performed after intravesical administration of ^{131}I-urease nanomotors in both water and urea solution, confirming the presence of radioactive signal within the bladder. Therapeutic effect was determined by post-treatment MRI sessions, showing a positive impact of self-propelling capacity of urease nanomotors on tumour progression. The results obtained in Chapter 5 are just a preliminary study of the potential use of urease-powered nanomotors as therapeutic radiopharmaceuticals for bladder cancer therapy, and further experiments are required in the future.

Resumen

A pesar de los avances recientes, el cáncer sigue siendo una de las principales causas de muerte en el mundo. Concretamente, el cáncer de vejiga es el noveno cáncer más común, en el que se diagnostican globalmente medio millón de casos cada año. A pesar de tener una tasa del 77% de supervivencia, la recurrencia suele aparecer en el 30-70% de los pacientes en un plazo de 5 años. Los casos diagnosticados, se clasifican normalmente como cáncer de vejiga superficial, que se encuentra en el revestimiento de la vejiga, o cáncer de vejiga invasivo, que invade la pared muscular de la vejiga y tiene riesgo de generar metástasis en otros órganos. La mayoría de los casos (75%) se diagnostican como cáncer de vejiga superficial, cuyo tratamiento consiste en una resección transuretral, seguida de quimioterapia (mitomicina C, MMC) y/o inmunoterapia (bacilo de Calmette-Guérin, BCG) intravesical en función del grado del tumor. Mientras que, en los casos de cáncer invasivo, el tratamiento es la extirpación total de la vejiga (cistectomía radical).

La estructura fisiológica de la vejiga está diseñada para proteger la superficie de la vejiga de agentes terapéuticos. Es por eso por lo que los actuales tratamientos no son del todo efectivos, ya que hay una penetración insuficiente y adhesión débil del medicamento en la vejiga. A demás, el tiempo de vida del medicamento es bastante corto, debido a la generación continua de orina, de manera que se requieren continuas cateterizaciones para mantener una dosis alta y efectiva. Es necesario pues desarrollar nuevas estrategias terapéuticas para mejorar el confort del paciente, además de minimizar la recurrencia y progresión del tumor.

En los últimos años, los nuevos avances en el área de la nanotecnología han recibido mucho interés por su impacto en el tratamiento de varias enfermedades. Una de las aplicaciones más estudiadas es la utilización de nanomateriales como herramientas para incrementar la eficacia y minimizar efectos secundarios en el tratamiento del cáncer. De hecho, los nanomateriales pueden contener los medicamentos en su interior y ser diseñados con varias funcionalidades con el fin de mejorar la estabilidad, la solubilidad del medicamento encapsulado, el tiempo de circulación y la acumulación en el tejido u órgano de destino. Sin embargo, uno de los principales desafíos de estos nanosistemas es la penetración en tejidos y barreras celulares. De hecho, un estudio publicado reveló que sólo el 0.7% de la dosis inyectada de nanomaterial llega a su sitio objetivo después de una administración sistémica. Por este motivo, ha surgido una nueva generación de nano-vehículos, llamados micro- y nanomotores, que son capaces de auto-propulsarse en un medio determinado. Estos nuevos materiales combinan las propiedades de los nanomateriales tradicionales con la capacidad de auto-movimiento. Dentro de este campo,

y con el objetivo de utilizarlos en aplicaciones biomédicas, los nanomotores diseñados con enzimas se han posicionado como una buena estrategia, ya que su propulsión se realiza a partir de combustibles compatibles con los sistemas biológicos. Por ejemplo, los nanomotores funcionalizados con ureasa, cuya auto-propulsión es promovida por la conversión de urea (presente en la composición de la orina) en dióxido de carbono y amoniaco, podrían ser utilizados como vehículos de medicamentos para el diagnóstico y/o tratamiento del cáncer de vejiga.

En esta tesis doctoral, se han desarrollado varias estrategias de marcaje radioactivo para nanomotores funcionalizados con ureasa, con el fin de permitir su monitorización *in vitro* e *in vivo* mediante técnicas de imagen nuclear. Además, se ha evaluado la capacidad de acumulación en tejido tumoral y efecto terapéutico de los nanomotores de ureasa tras su administración intravesical en animales portadores de cáncer de vejiga.

El trabajo llevado a cabo en este doctorado se ha dividido en tres partes, que corresponden a los capítulos experimentales 3,4 y 5 de este documento. En la primera parte del trabajo (Capítulo 3), se presenta el desarrollo de dos estrategias de radiomarcaje para los nanomotores funcionalizados con ureasa, con el objetivo de incorporar dos isótopos emisores de positrones en su estructura, el yodo-124 (^{124}I) y el flúor-18 (^{18}F). En el caso del radiomarcaje con ^{124}I, la reacción se produjo vía absorción directa del ^{124}I con las nanopartículas de oro presentes en la superficie de los nanomotores (Figura 1a). Es una reacción que ha sido previamente descrita con altos rendimientos, ya que existe una gran afinidad entre el yodo y el oro. De hecho, el rendimiento radioquímico obtenido fue del 71 ± 2%, con una pureza radioquímica superior al 99%.

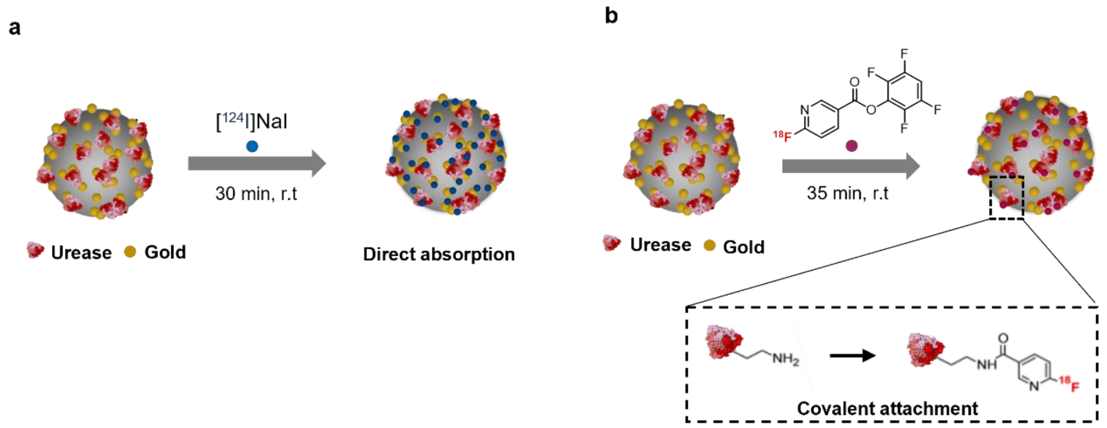

Figura 1. a) Radiomarcaje de los nanomotores de ureasa vía absorción directa del ^{124}I en las nanopartículas de oro. b) Radiomarcaje de los nanomotores de ureasa vía reacción entre el [^{18}F]F-PyTFP y los grupos amino presentes en la enzima.

Por otro lado, se desarrolló una nueva metodología de marcaje de nanomotores con ^{18}F, basada en la reacción entre un éster activado, previamente marcado con ^{18}F ([^{18}F]F-PyTFP) y los grupos amino presentes en las enzimas funcionalizadas en la superficie de los nanomotores (Figura 1b). El rendimiento radioquímico en este caso fue del 30% en relación con el compuesto [^{18}F]F-PyTFP, con una pureza radioquímica superior al 99%.

Una vez marcados los nanomotores, se llevó a cabo un estudio *in vitro* utilizando Tomografía por Emisión de Positrones (PET, de sus siglas en inglés), para estudiar el movimiento colectivo de los nanomotores en estructuras con diferentes grados de complejidad (Figura 2). El estudio mostró claramente que independientemente de la estructura utilizada, cuando los nanomotores de ureasa están en presencia de urea son capaces de llegar al final del canal, ya que tienen sus propiedades motoras activas, mientras que, en presencia de agua, la mayoría de los nanomotores se mantienen en el punto de partida. Esto se observó tanto para los nanomotores de ureasa marcados con ^{18}F como con ^{124}I.

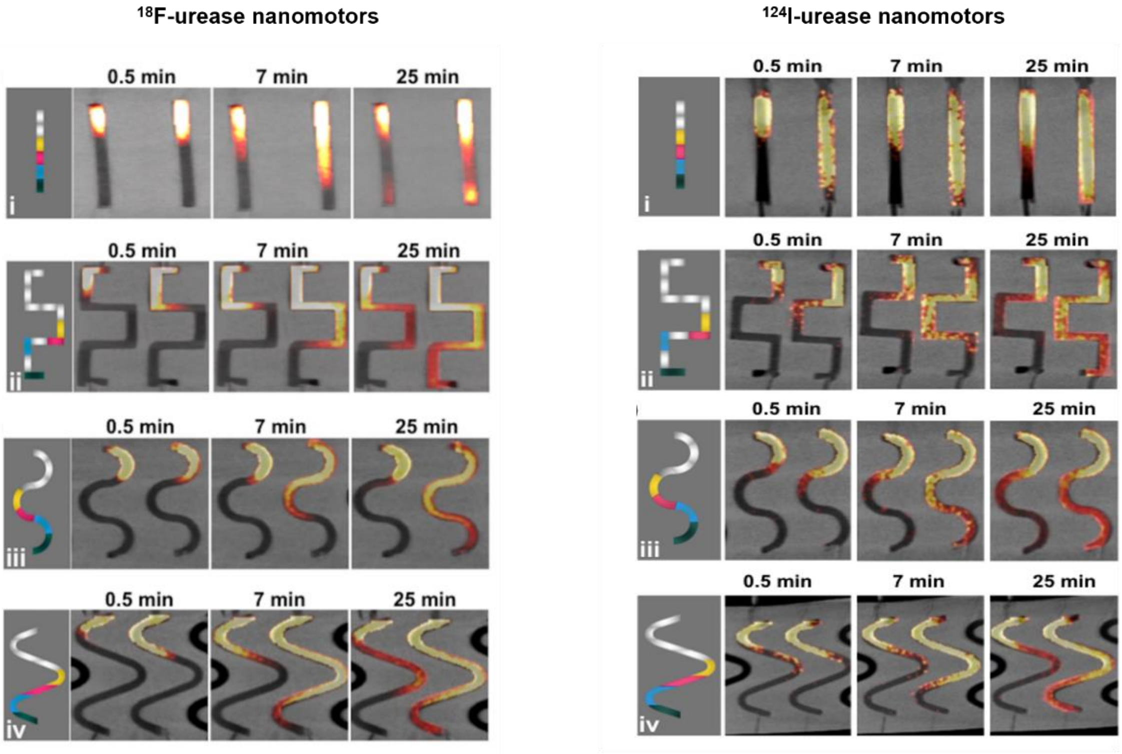

Figura 2. Imágenes PET (proyecciones coronales) obtenidas a los minutos 0.5, 7 y 25 tras la administración de los nanomotores de ureasa marcados con ^{18}F y ^{124}I en las diferentes estructuras. Para cada estructura, un canal se llenó con agua (izquierda) y el otro con una solución 300 mM de urea (derecha).

Una vez confirmado que el movimiento de los nanomotores de ureasa incrementa en presencia de urea y que el PET es una buena herramienta para el seguimiento y cuantificación de los nanomotores, se estudió su biodistribución *in vivo* después de una administración intravenosa e intravesical en ratones sanos.

Para la administración intravenosa se estudiaron los nanomotores de ureasa marcados tanto para el ^{18}F como para ^{124}I en ratones sanos. La biodistribución obtenida fue diferente para los dos radioisótopos, con una acumulación mayoritaria en pulmones e hígado para los nanomotores marcados con ^{18}F, y una acumulación en tiroides, estómago y orina para los nanomotores marcados con ^{124}I. Los sitios metabólicos del yodo libre son la tiroides, el estómago y la orina, lo que sugiere una rápida deyodación de los nanomotores. Por lo tanto, el estudio de biodistribución tras administración intravenosa evidenció que los nanomotores marcados con un emisor de positrón pueden ser monitorizados *in vivo* por PET en combinación con la Tomografía Computarizada (CT, de sus siglas en inglés), y que además el marcaje de los nanomotores de ureasa con ^{18}F, es mucho más estable que el de ^{124}I.

Como los tratamientos para el cáncer de vejiga se administran por vía intravesical, se decidió estudiar el comportamiento de los nanomotores de ureasa marcados con ^{18}F en una vejiga sana de ratón hembra mediante PET. Las imágenes resultantes, junto a las curvas de actividad-tiempo obtenidas de su cuantificación, mostraron la formación de dos fases debido a la entrada de orina fresca durante el estudio de imagen (Figura 3). Esta nueva orina, que no es radioactiva, desplaza la solución que contiene los nanomotores de ureasa marcados con ^{18}F, creando las dos fases. Cuando los nanomotores de ureasa son administrados en urea, sus propiedades móviles están activas, de manera que mejoran el efecto de mezclado, obteniéndose al final del estudio de imagen una distribución homogénea dentro de la vejiga (Figura 3 (1)). En cambio, cuando los nanomotores de ureasa marcados con ^{18}F son administrados en agua, la separación entre las dos fases se mantiene durante todo el estudio debido a que los nanomotores no están en contacto con la urea (presente únicamente en la orina) y por lo tanto sus propiedades móviles no están activas (Figura 3 (2)). Esta hipótesis se confirmó, utilizando nanomotores funcionalizados con albúmina de suero bovino (BSA, de sus siglas en inglés) marcados con ^{18}F, los cuales no presentan ninguna propiedad motora ni en agua ni en urea (Figura 3 (3 y 4)).

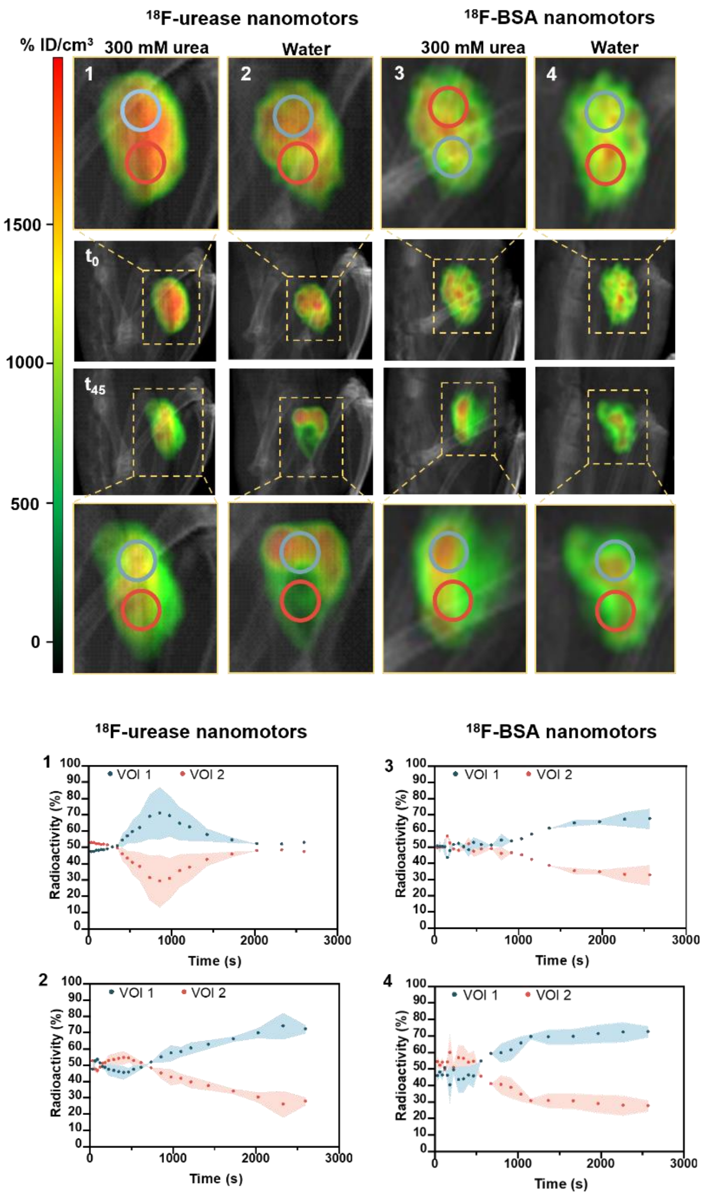

Figura 3. Imágenes PET (proyecciones de máxima intensidad), corregistradas con sus imágenes obtenidas mediante CT, y sus correspondientes cuantificaciones obtenidas a diferentes tiempos tras la administración intravesical de nanomotores de ureasa marcados con ^{18}F en urea (1) y agua (2), y de nanomotores de BSA marcados con ^{18}F en urea (3) y agua (4).

En vista de los resultados obtenidos en el Capítulo 3, en la segunda parte del trabajo (incluida en el Capítulo 4), se describe la evaluación de la capacidad de los nanomotores de ureasa de acumularse en el tejido tumoral utilizando un modelo de ratón de cáncer de vejiga.

Para ello, se inocularon ratones hembra con una línea celular de carcinoma de células de vejiga murino (MB49, de sus siglas en inglés) para desarrollar el tumor en la propia vejiga. Se utilizó la imagen por Resonancia Magnética (MRI, de sus siglas en inglés) para monitorizar el crecimiento tumoral en la vejiga a día 7 y 14 tras la implantación de las células tumorales. Las imágenes de

MRI obtenidas mostraron la presencia de tumor, una masa gris en la parte superior de la vejiga, en la mayoría de los animales. El análisis de las imágenes mediante el programa Image J, permitió obtener valores de volumen tumoral y, por lo tanto, cuantificar las diferencias de tamaño entre las dos sesiones de MRI. A partir de esos valores tumorales, se clasificaron los animales en diferentes grupos para llevar a cabo el estudio de imagen mediante PET.

El estudio de acumulación tumoral se realizó mediante PET, tras la administración intravesical de los nanomotores de ureasa y BSA marcados con ^{18}F utilizando urea y agua como vehículo. Además, se administraron nanomotores de ureasa marcados con ^{18}F en vejigas sanas, como control adicional, para evaluar la adhesión de los nanomotores al tejido sano. El procedimiento de marcaje fue el mismo que se utilizó en el Capítulo 3.

Como se puede ver en la Figura 4, las imágenes PET correspondientes a la administración de nanomotores de ureasa utilizando urea como vehículo en vejiga sana (control), mostraron ausencia de señal radioactiva, confirmando la baja adherencia y/o penetración de los nanomotores de ureasa en tejido sano. En cambio, para los animales con tumor, las imágenes PET correspondientes a los grupos 1-4, mostraron presencia de señal radioactiva en la parte superior de la vejiga, cuya posición coincide con la del tumor según las imágenes de MRI (Figura 4a, grupos 1-4). En las propias imágenes PET se puede observar que la señal radioactiva más intensa corresponde al grupo 4, los nanomotores de ureasa administrados en urea. Esto se confirmó con la cuantificación de las imágenes, dibujando volúmenes de interés (VOIs) en la región superior de la vejiga y normalizando los valores de actividad al volumen tumoral determinado por MRI (Figura 4b). La cuantificación confirmó el aumento significativo de captación tumoral para el grupo 4 (*ca*. 150 % ID/cm^3) en comparación para los grupos 1-3 (*ca*. < 20 % ID/cm^3), confirmando de esta forma el efecto positivo de la auto-propulsión en la acumulación tumoral. Estos resultados se confirmaron mediante; (i) Espectrometría de Masas con Plasma Acoplado Inductivamente (ICP-MS), detectando la presencia de oro proveniente de los nanomotores en los tumores; (ii) inmunofluorescencia, confirmando la acumulación tumoral y penetración de los nanomotores; y (iii) histología, corroborando el correcto desarrollo del tumor en todos los grupos.

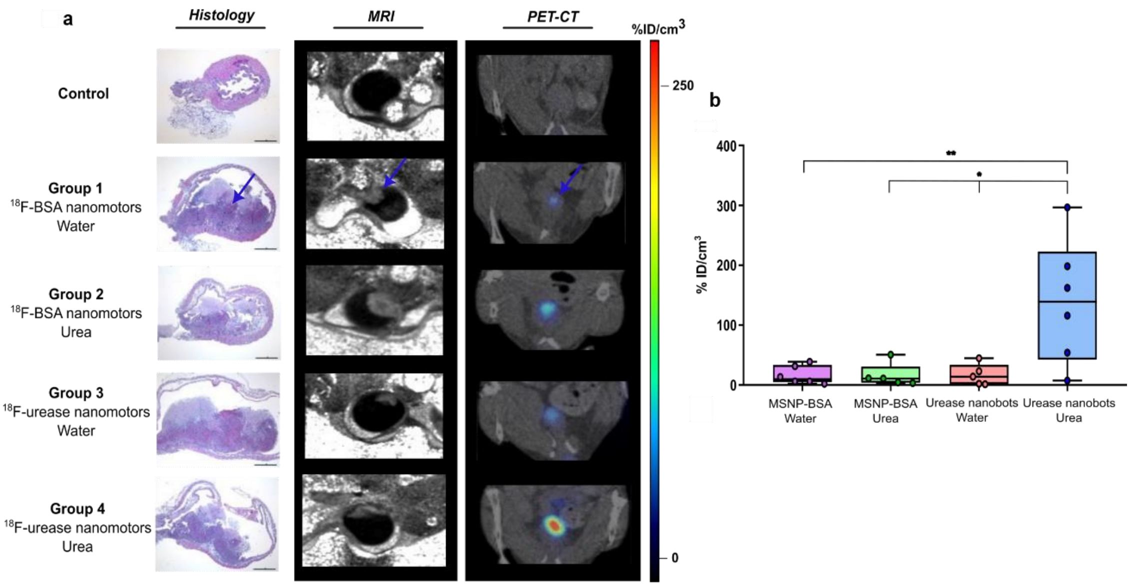

Figura 4. a) Imágenes representativas de histología, MRI y PET-CT de los animales correspondientes a los animales control y los animales de los grupos 1-4. Para las imágenes histológicas, la escala corresponde a 1 mm; las imágenes PET han sido corregistradas con el correspondiente CT para la localización anatómica de la señal radioactiva. b) Acumulación de la radioactividad en el tumor para los animales de los grupos 1-4, normalizado por volumen tumoral obtenido por MRI y expresado como porcentaje de dosis en el volumen tumoral (% ID/cm^3). Control: nanomotores de ureasa marcados con ^{18}F administrados en urea en ratón sano; grupo 1: nanomotores de BSA marcados con ^{18}F administrados en agua; grupo 2: nanomotores de BSA marcados con ^{18}F administrados en urea; grupo 3: nanomotores de ureasa marcados con ^{18}F administrados en urea; grupo 4: nanomotores de ureasa marcados con ^{18}F administrados en urea. $^{**}p < 0.01$; $^{*}p < 0.05$.

En vista de los resultados prometedores obtenidos en el Capítulo 4, la tercera y última parte del presente trabajo (Capítulo 5) ha consistido en la aplicación de la terapia con radionucleidos en cáncer de vejiga utilizando los nanomotores de ureasa como vehículos. Para ello, se diseñó una estrategia de marcaje que incorporara el yodo-131 (^{131}I) a la estructura de los nanomotores de ureasa. El radiomarcaje se produjo vía absorción directa del ^{131}I con las nanopartículas de oro presentes en la superficie de los nanomotores, obteniendo un rendimiento radioquímico del 73 ± 10%, y una pureza radioquímica superior al 99%.

Como en el Capítulo 4, se inocularon ratones hembra con la línea celular MB49 para desarrollar el tumor en la vejiga. Para el estudio de terapia, los animales se clasificaron aleatoriamente en diferentes grupos, según su tamaño tumoral determinado por MRI. Cada ratón, recibió una única inyección intravesical del correspondiente compuesto (según el grupo). Se realizaron estudios de Tomografía Computarizada por Emisión de Fotón Único (SPECT, de sus siglas en inglés) para confirmar la presencia de señal radioactiva en el tumor 3 horas después de la administración del tratamiento. Finalmente, el efecto terapéutico se determinó mediante una única sesión de MRI.

El trabajo presentado en este último capítulo es un estudio preliminar del potencial de estos nanomotores para la terapia con radionucleidos. Los resultados obtenidos sugieren que cuando los nanomotores de ureasa marcados con ^{131}I son administrados en urea, hay un efecto positivo de la capacidad de auto-propulsión en el efecto terapéutico. Este efecto es evidente cuando se trabaja en bajas dosis de ^{131}I, donde los nanomotores de ureasa administrados en urea evitan el crecimiento tumoral. Sin embargo, cuando se administran altas dosis de ^{131}I, las propiedades móviles de los nanomotores parece que no contribuyen tanto a tener un mayor efecto terapéutico. Se requieren más estudios en el futuro para confirmar los resultados obtenidos en esta última parte del trabajo.

CHAPTER 1

GENERAL INTRODUCTION

Chapter 1: General Introduction

1.1 Nanoparticles and nanomedicine

1.1.1 Nanoparticles: definition and applications

Nanoparticles (NPs) are a wide class of materials which have one dimension less than 100 nanometres [1, 2]. NPs can be made of many different materials, such as proteins, peptides, lipids, polymers, metals, and carbon atoms, in different shapes and sizes[3]. Depending on their size and composition, NPs have different physicochemical properties and therefore, can be used in a huge range of applications such as catalysis[4], chemical or biological sensing[5], and medicine[6], among others. In recent years, there has been a growing interest in using NPs in biomedical applications due to their versatile modification possibilities. In fact, an appropriate modification of their surface could enhance their solubility and stability in complex environments such as blood or tissue. Additionally, NPs can be functionalized with different moieties (fluorescent dyes, drugs, targeting ligands, etc.) to provide multi-modal treatments[7]. For that reason, NPs have emerged as potential candidates both for diagnosis and therapy.

1.1.2 NPs in nanomedicine: Oncology

Nanomedicine is a new research field based on the use of nanoscale materials and devices in health and medicine, as defined by the European Commission[8]. In fact, NPs are being deeply investigated in the field of biomedicine, with special emphasis on imaging and drug delivery[7]. The unique properties of NP-based systems, together with the possibility to load a high amount of cargo, provide some advantages over traditional drugs. Specifically, NPs have been considered as promising therapeutic agents in oncology due to their capacity to passively accumulate in tumour tissue via enhanced permeability and retention (EPR) effect after intravenous (i.v.) administration[9]. This effect is based on the fact that pathological vasculature is leaky, and therefore, penetrable for large molecules. This phenomenon, together with a compromised lymphatic drainage, is responsible of tumour accumulation of nanomaterials (Figure 1.1).

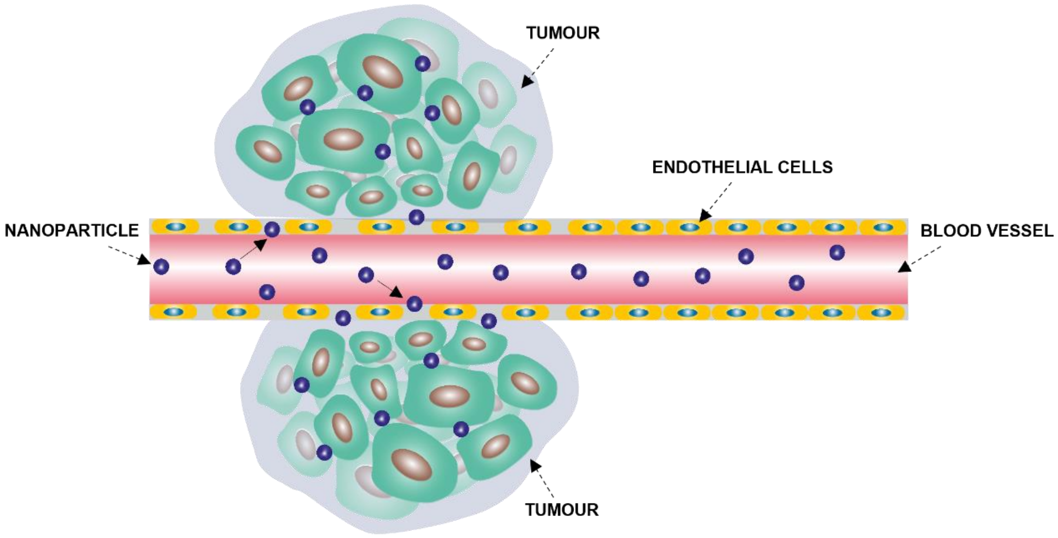

Figure 1.1. Schematic representation of passive accumulation of NPs in tumours by enhanced permeability and retention (EPR) effect.

Many different NPs have been proposed as nanocarriers for cancer therapy. The ideal candidate has to meet some criteria: (I) biocompatibility; (II) prolonged circulation in blood; and (III) stability and ability to accumulate in the target tissue via EPR effect[10]. There are different possibilities to classify NPs, depending on their properties, structure, size, and final application. NP-based drug delivery systems are commonly classified into three groups: polymeric NPs, inorganic NPs, and lipid-based NPs (Figure 1.2). Among all, liposomes, micelles, and polymeric NPs are the most extensively used[11, 12]. In fact, liposomes and polymer-conjugated drugs using polyethyleneglycol (PEG) or *N*-(2-hydroxypropyl)methacrylamine (HPMA), are predominant in clinical trials[13].

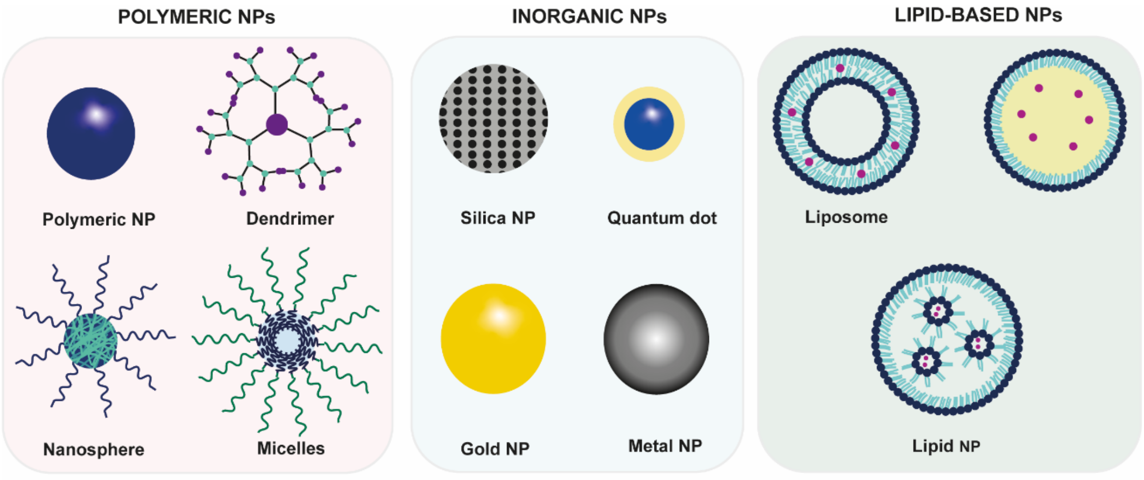

Figure 1.2. Schematic illustration of different types of NPs used as drug delivery systems. Adapted from Mitchell, M. J.[11]. General classification as polymeric NPs, Inorganic NPs, and Lipid-based NPs.

Nevertheless, some challenges still need to be overcome in order to see more nanoformulations in clinical phases. Nanocarriers need to improve their targeting capacity since a recent study suggests that, in average, only about 0.7% of parenterally administrated NPs are found to be delivered to solid tumours[14]. The main reason is the high accumulation of NPs in organs of the mononuclear phagocytic system (MPS; formerly known as the reticuloendothelial system or RES), particularly in the liver and spleen. Furthermore, they need to improve their penetration ability, delivery on the subcellular level, and motion controllability. For that reason, in the last years a new generation of drug-delivery systems have been developed: the so-called micro- and nanomotors (MNMs).

1.1.3 Micro- and nanomotors

Micro- and nanomotors (MNMs) have emerged as a new generation of NP-based drug delivery system, as they combine the advantages of non-motile nanocarriers (i.e. selectivity, biocompatibility, stability) with the capacity to swim in specific media. MNMs are micro- or nano-devices capable of generating autonomous motion in fluidic environments by different types of energy source (catalytic, electro/magnetic, or acoustic) at small scale. These self-propelled machines hold huge promise in a diversity of fields, such as drug delivery, diagnostics, chemical/biological sensing, cell and tissue penetration, cell transport, and environmental remediation, among others[15-18]. The inspiration to obtain these synthetic MNMs comes from nature, since there is a large collection of examples of motion performed in living organisms, extending from enzymatic assemblies to bacteria and cells. The MNMs can be classified into chemical, physical or biological systems, depending on their propulsion movement (Figure 1.3). Chemical MNMs are those that transform chemical energy into kinetic motion through a catalyst (Figure 1.3a). The movement of these motors is hard to control, nonetheless they can be guided by chemical gradients in their surroundings. Physical MNMs are propelled by an external stimulus, such as magnetic fields, ultrasound, or light field (Figure 1.3b). Unlike chemical MNMs, these swimmers are easier to control since changing the field's orientation or frequency alters the direction and velocity of the motor. Finally, biological or biohybrid motors are propelled by natural microswimmers, such as sperm or bacteria (Figure 1.3c). Their movement can be controlled by external fields or by the cells and microorganisms. In this thesis only catalytic MNMs, specifically enzyme-driven nanomotors, will be described to some extent, as these are the MNMs used in the experimental part. Excellent reviews can be found in the literature about the other types of MNMs[19].

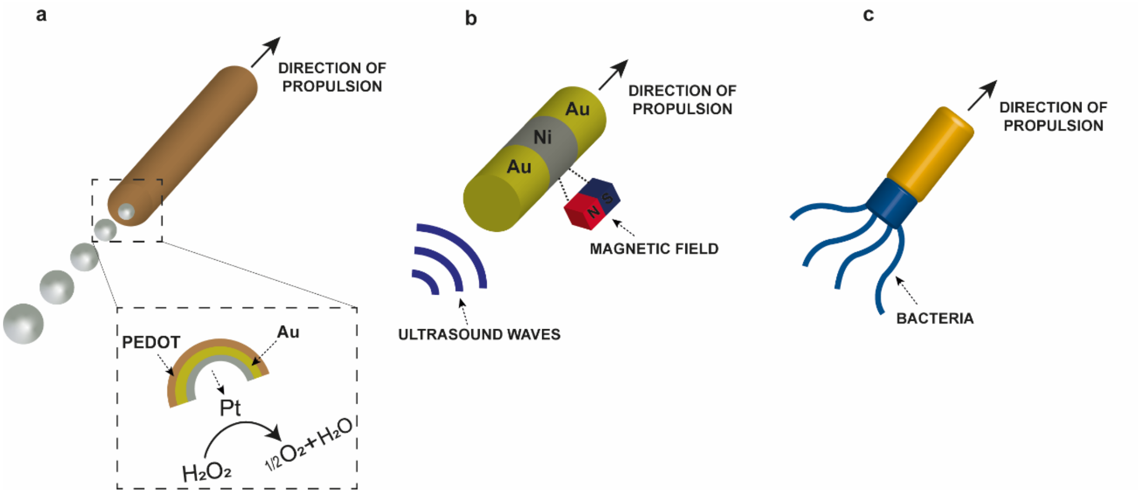

Figure 1.3. Representative examples of the different types of MNMs. a) Schematic illustration of a chemical MNM using the catalytic reaction of H_2O_2 as fuel. b) Schematic representation of physical MNM, where propulsion is promoted by ultrasound and guided by the magnetic field. c) Schematic diagram of biological MNMs, using bacteria as fuel. Au: gold; Pt: platinum; PEDOT: poly(3,4-ethylenedioxythiophene).

1.1.3.1 Enzyme-powered micro- and nanomotors

The MNMs field has been growing over time since the discovery of the first reported system based on catalytic motors of gold-platinum (Au-Pt), propelled by gas bubbles generated from the oxidation of hydrogen peroxide (H_2O_2) on the platinum (Pt) side and the reduction of water on the gold side[20, 21] (Figure 1.3a) . Since then, many strategies have been employed to develop new MNMs with various sizes, geometries, and propulsion mechanisms. Despite the significant advances in the area, the major drawback for medical application has been the toxicity of the fuel used for their motion, making difficult the use of these MNMs in biological systems. In the recent years, efforts have been focused on developing enzymatic motors that can self-propel using biocompatible fuels, such as glucose or urea.

Enzymes are proteins capable to catalyse the conversion of a substrate into its products with high specificity and efficiency at the cellular level[22]. Hence, enzymes unchain biocatalytic reactions that can convert chemical energy into kinetic motion for biological processes. For instance, deoxyribonucleic acid (DNA) synthesis by DNA polymerase, hydrolysis of proteins by endopeptidase, vesicular transport, and generation of energy to move from the hydrolysis of adenosine triphosphate (ATP). Therefore, enzymes are considered to be biological nanomotors that enhance the diffusion by its catalytic activity[23]. Based on this, different systems based on the combination of synthetic particles (i.e. polymers or inorganic particles) and enzymes have been reported, aiming at expanding application opportunities in different areas including drug delivery[24]. Particularly, the use of mesoporous silica nanoparticles (MSNPs) has been reported as a promising theranostic platform[25]. MSNP, specifically the Mobil Composition of Matter No. 41 (MCM-41) type, is a widely studied material for biomedical applications which is approved for clinical use by the Food and Drug Administration (FDA)[26]. Furthermore, MSNPs have a high drug-loading capacity and superior biocompatibility both *in vitro* and *in vivo*[27]. For these reasons, many examples can be found in the literature on the use of Janus and non-Janus MSNP-based motors with different enzymatic reactions, including catalase[28], glucose oxidase (GOx)[29] and urease[30] (Figure 1.4).

Figure 1.4. Scheme illustrating enzymatic mesoporous silica Janus nanomotors using three types of enzymes; catalase (a), glucose oxidase (GOx) (b), and urease (c). Adapted from Ma, X.[29]

The use of enzymes in the field of MNMs not only brings a new insight into the possibility of using nontoxic fuel, but also offers increased versatility for the design of swimmers based on when and where the substrate is present. In this PhD thesis, non-Janus urease-powered nanomotors were investigated, which propulsion is promoted by the conversion of urea ($CO(NH_2)_2$) into carbon dioxide (CO_2) and ammonia (NH_3).

1.1.3.2 Micro- and nanomotors in biomedical applications: Oncology

One of the most active research fields in nanomedicine is the improvement of cancer treatment and diagnosis. Conventional delivery strategies rely on the circulation of body fluids and suffer from the lack of adequate penetration and targeting, making it difficult for drugs to enter some tissues. Consequently, the clinical function of many active molecules is compromised. The design of active and smart systems has emerged as an alternative to traditional nanocarriers to overcome the long-standing challenge of drug efficacy. Compared to passive drugs, MNM's autonomous movement can significantly improve adhesion and tissue penetration, and therefore the loaded cargos can be delivered more efficiently, thus increasing therapeutic efficacy when treating cancer[31]. Furthermore, the required doses of pharmaceuticals can be reduced due to the specific targeting possibilities. In fact, there are some proof-of-concept results that demonstrate improvement in anticancer drug delivery *in vitro*[32, 33].

As already mentioned, enzymatic MNMs have several advantages respect to other catalytic MNMs due to their high diversity, bioavailability, and biocompatibility upon demand of the target application. Among all the possibilities, urease-powered nanomotors are promising drug delivery agents for bladder cancer diagnosis and/or treatment since urea is present in considerable amount in the urinary bladder (maximum concentration around 300 mM[34]). The use of urease-powered nanomotors coupled with and antibody[35], for the active targeting of bladder cancer cells in 3D cultures (bladder cancer spheroids) has been reported to enhance diffusion and internalization efficiency. Despite these encouraging results, tracking nanomotors or any nanoformulation *in vivo*, quantitatively and at the whole-body level, which is paramount for translation into clinical applications, remains a major challenge.

1.1.4 Bladder cancer: General aspects

Cancer is still one of the leading causes of death worldwide, according to the World Health Organization (WHO). Particularly, bladder cancer (BC) is the ninth most common malignancy with at least half a million new cases diagnosed globally each year[36, 37]. BC is a rather heterogenous disease whose classification is a challenging task. The depth of tumour invasion (T stage) is the deciding factor and can be categorized into non-muscle-invasive bladder cancer (NMIBC) and muscle-invasive bladder cancer (MIBC), the latter with risk of metastasis in other organs (Figure 1.5). Approximately 75% of the new cases diagnosed are classified as NMIBC (Tis, Ta and T1, Figure 1.5)[38, 39]. The standardised procedure for treating NMIBC consists of transurethral resection of the tumour followed by intravesical instillation of immunotherapeutic (Mycobacterium bovis bacillus Calmette-Guérin, BCG[40]) and/or chemotherapeutic agents (i.e. mitomycin C, MMC[41]). By contrast, MIBC needs to be treated with a surgical procedure involving either partial or complete removal of the urinary bladder.

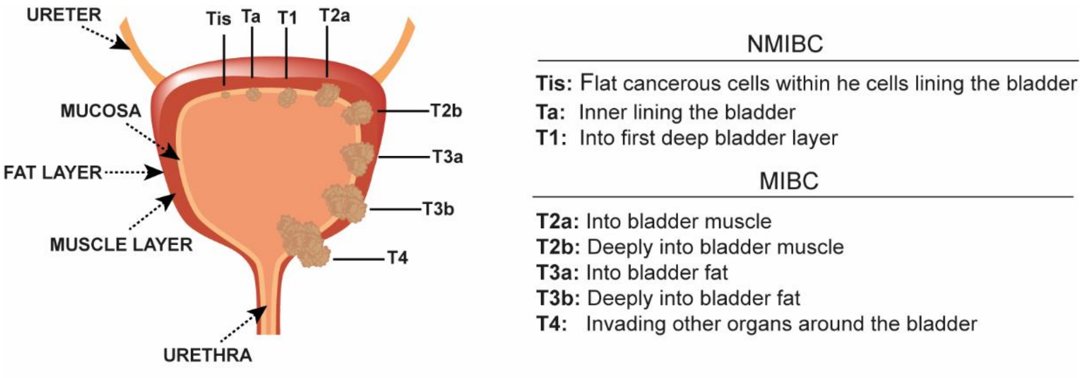

NMIBC

Tis: Flat cancerous cells within he cells lining the bladder
Ta: Inner lining the bladder
T1: Into first deep bladder layer

MIBC

T2a: Into bladder muscle
T2b: Deeply into bladder muscle
T3a: Into bladder fat
T3b: Deeply into bladder fat
T4: Invading other organs around the bladder

Figure 1.5. Schematic representation of the different stages of bladder cancer tumour. NMIBC: non-muscle-invasive bladder cancer; MIBC: muscle-invasive bladder cancer.

The physiological structure of the bladder cavity prevents the use of the systemic administration of drugs since only a small fraction of the drug reaches the target site. Local administration of the therapy has proven to be an effective method to reduce the dose required while favouring maximal drug concentration in the tumour vicinity and minimize systemic side effects.

Nevertheless, actual treatments can still cause severe side effects and are not completely effective as recurrence appears in 30% to 70% of the patients within 5 years, thus raising treatment costs[42]. The efficacy of the intravesical treatment has some limitations related to the insufficient penetration of drugs into urinary bladder wall and weak adhesion to the target site[43]. Moreover, the residence time of drugs inside the bladder is quite short due to the entrance of fresh urine, and therefore continuous administrations are required to maintain high drug concentration[39]. New therapeutic strategies are needed to improve patient outcomes and minimize recurrence and progression rates.

In recent years, different nanocomposites have been evaluated as drug delivery agents for intravesical administration, including polymeric NPs[43-45], multiwalled carbon nanotubes[46], liposomes[47], and mesoporous silica NPs[48], among others. Some of these nanoformulations contribute to enhance adherence to the tumour. However, major limitations still need to be addressed. Firstly, the complexity of reaching the whole bladder due to sedimentation of the nanocomposites over time or entrance of fresh urine. Secondly, penetration into the tumour tissue can be hampered by the limited diffusion rate leaving untreated regions. Enzyme-powered nanomotors could potentially aid overcoming such limitations thanks to their continuous momentum and ability to explore wider areas than traditional passive particles. In the context of this PhD thesis, urease-powered nanomotors have been evaluated in an orthotopic model of bladder cancer, as described in Chapters 4 and 5.

1.2 Tracking NPs *in vivo*: Nuclear imaging techniques

1.2.1 Why is it important to track NPs?

Despite the advantages listed above, NPs for *in vivo* applications must fulfil certain requirements prior to entering the clinical area. Nanoformulations should be biocompatible, have sufficient blood residence time to reach the target organ or tissue (if they are to be injected intravenously), be easily cleared from the body, and show low accumulation in off-target sites to minimize side effects. For that reason, the pharmacokinetics and biological fate of NPs need to be known to accurately establish the therapeutic dose and predict off-target side effects. Nevertheless, NPs are extremely difficult to detect and quantify once distributed in a biological system. For instance, in some preclinical studies, organs are often harvested at pre-determined time points after administration of the NPs and then, directly visualised by imaging techniques such as transmission electron microscopy (TEM)[49] and confocal Raman microscopy[50], or indirectly quantified by inductively coupled plasma mass spectrometry (ICP-MS)[51]. However, these techniques require sacrifice of large numbers of experimental animals to ensure statistical power and can only be applied to certain NP types. Furthermore, not all these techniques are quantitative. Hence, new *in situ* methodologies are required for pharmacokinetics and fate studies *in vivo*.

A first approach to overcome these limitations consists of labelling NPs with radionuclides (i.e. positron or gamma emitters) to detect and quantify the different components using ultra-sensitive imaging modalities such as positron emission tomography (PET) and single-photon emission computerised tomography (SPECT). These non-invasive molecular imaging techniques are excellent tools to evaluate pharmacokinetic profiles of novel nanosystems both in preclinical and clinical stages[52-54].

1.2.2 Nuclear Imaging

Nuclear imaging techniques rely on the administration of a trace amount of a radioactive compound, labelled with a positron or gamma emitter, to study physiological and molecular processes within the body. These techniques are based on the detection of gamma rays produced by the spontaneous disintegration of a radionuclide. Using specific equipment (e.g. PET or SPECT cameras), these gamma rays can be detected in such a way that the concentration of radioactive compound can be precisely quantified, provided the radioisotope remains bound to the compound. Therefore, absolute quantification of the concentration of a radionuclide or a compound labelled with a radionuclide can be obtained *in vivo* and over time using nuclear imaging techniques.

1.2.2.1 Positron Emission Tomography

Positron emission tomography (PET) is the most sensitive technique used in nuclear imaging. As mentioned before, it is based on the administration of positron emitter radionuclides to finally obtain three-dimensional images of biochemical processes in experimental animals or humans. When a positron emitter disintegrates by spontaneous decay, a positron is emitted (Figure 1.6a). The positron is the antiparticle of an electron, with equivalent mass but positive charge. Once emitted, the positron interacts with surrounding particles following a random pathway, while losing progressively its kinetic energy. When it is almost at rest, the positron annihilates with an electron, resulting in the emission of two gamma rays travelling in opposite directions (180°) with an energy of 511 keV each. The linear distance between the locations where disintegration and annihilation occur is called positron range and is typically of a few millimetres in water. The detection of these gamma rays is the basis of PET imaging. When a positron emitter labelled compound is administered to a living organism, millions of gamma ray pairs (which have a high penetration power) are generated, escape from the body, and are detected by an external ring of detectors of the PET cameras (Figure 1.6b). The simultaneous detection of two gamma rays by two detectors defines the line of response (LOR). LOR is the straight line between the two detectors where the annihilation occurred, although the precise position is not known. The detection of millions of pairs of gamma rays enables the reconstruction of three-dimensional and time-resolved images containing quantitative information of the concentration of the radionuclide.

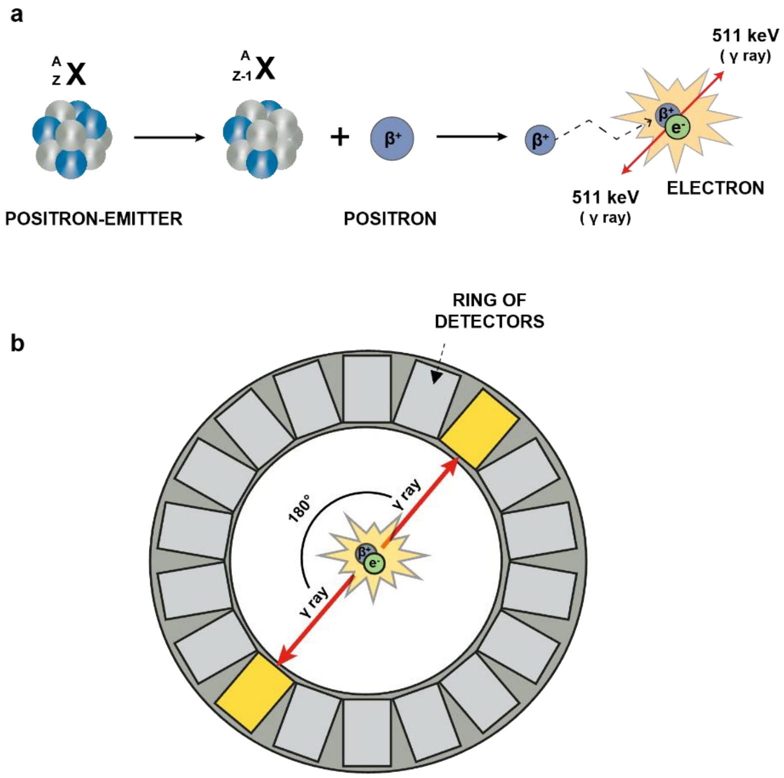

Figure 1.6. a) Schematic representation of spontaneous radioactive decay of a positron-emitter, resulting in the emission of a positron. After travelling a certain distance, two gamma (γ) rays are generated (511 keV each) after annihilation process between an electron and a positron. b) Schematic representation of parallel gamma ray's detection using a PET scanner.

Normally, PET is used in combination with computerized tomography since anatomical information is required to unambiguously localise the radioactive signal. In preclinical and clinical fields, the typical practice consists of performing consecutive PET and CT scans to finally analyse both images together. Anatomical images are used to define volumes of interest (VOIs) in different regions of the body. These VOIs are then translated into the PET images to obtain the concentration of radioactivity as a function of time.

One key aspect in PET imaging is the selection of the radionuclide which is necessary to ensure successful *in vivo* studies. This selection depends on the physical properties of the positron emitter, the most notable being half-life ($T_{1/2}$). The $T_{1/2}$ is defined as the length of time to decrease the amount of radioactivity to one half of the starting value. Ideally, the radioisotope should have a physical half-life similar to the biological half-life of the molecule or nanoformulation under investigation. If the physical half-life is too short, the radionuclide will decay before elimination from the organism, and part of the pharmacokinetic information will be lost. On the contrary, a long physical half-life will result in a high and unnecessary radiation dose for the subject. The latter is especially relevant in clinical studies, and when repeated administration is required. Another aspect to take into consideration is the positron range. A longer positron range will result in lower resolution images.

The most commonly used positron emitters in biomedical applications are fluorine-18 (^{18}F), carbon-11 (^{11}C), nitrogen-13 (^{13}N), oxygen-15 (^{15}O), zirconium-89 (^{89}Zr), gallium-68 (^{68}Ga), copper-64 (^{64}Cu) and iodine-124 (^{124}I) (see table 1.1 for physical half-lives and positron energies).

Table 1.1. Physical characteristics of the most commonly used positron emitters in biomedicine.

Isotope	$T_{1/2}$	Decay Mode ($^{+}\beta$ Fraction)	β^{+} Energy$_{max}$
^{18}F	109.8 min	97%	630 KeV
^{11}C	20.4 min	100%	960 KeV
^{13}N	9.98 min	100%	1190 KeV
^{15}O	2.05 min	100%	1730 KeV
^{89}Zr	78.4 h	22.3%	900 KeV
^{68}Ga	67.6 min	89.1%	1900 KeV
^{64}Cu	12.7 h	18%	660 KeV
^{124}I	4.18 days	23%	2140 KeV

1.2.2.2 Single Photon Emission Computerised Tomography

Single photon emission computerised tomography (SPECT) is another ultra-sensitive nuclear imaging technique used both in preclinical and clinical studies. In contrast to PET, SPECT is based on the use of gamma emitters. The spontaneous disintegration of these radionuclides directly generates gamma rays which have a range of energies between 100-300 keV (Figure 1.7a). The resulting photons emitted penetrate through the living organism and are detected by a ring of detectors placed around the living organism. Because the photons are detected individually and not in pairs (contrary to PET), physical collimators are required in SPECT cameras in order to know the position of the disintegration (Figure 1.7b). In fact, these collimators hamper the detection of a large fraction of gamma rays emitted, and consequently, the absolute sensitivity is much lower than in PET.

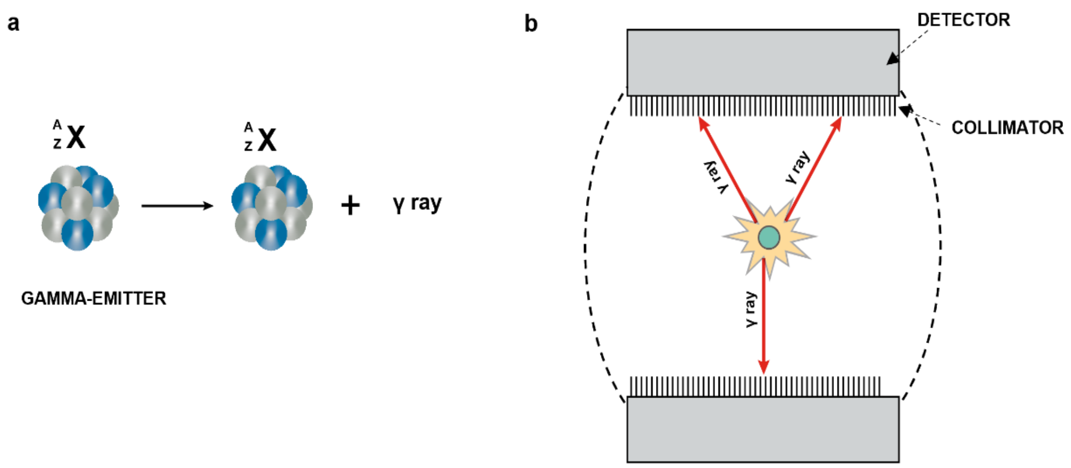

Figure 1.7. a) Schematic representation of spontaneous radioactive decay of a gamma (γ) emitter, resulting in the emission of a gamma ray. b) Schematic representation of the detection of photons using a SPECT scanner. Those photons not reaching the detector perpendicularly are absorbed by the collimator.

Most commonly used SPECT radionuclides in biomedicine and their main characteristics are summarised in table 1.2.

Table 1.2. *Physical properties of the most commonly used single-photon emitters.*

Isotope	$T_{1/2}$	Decay Mode (γ Fraction)	γ Energy_{max}
^{99m}Tc	6.02 h	89%	142 KeV
^{131}I	8.03 days	82%	364 KeV
^{123}I	13.22 h	83%	159 KeV
^{111}In	2.08 days	91,94%	171,245 KeV
^{177}Lu	6.65 days	6,10%	113,208 KeV

1.2.3 Radiolabelling of NPs

The successful application of nuclear imaging techniques to the *in vivo* development of new nanomedicines or drugs depends on the radiolabelling step. Radiolabelling is a chemical reaction in which a radionuclide is incorporated into a desired molecule to produce what is called a radiotracer. A wide variety of strategies have been developed for the incorporation of positron and gamma emitters into different NPs. Nevertheless, there are three main categories: (I) *In situ* generation of the radioisotope by direct ion[55] or neutron activation[56] of NPs; (II) attachment of the radionuclide once the NP has been synthetized by bifunctional chelators (BFCs) followed by complexation with a radiometal[57] ,or incorporation of a pre-labelled tag[58]; and (III) incorporation of the radioisotope during the NP synthesis using labelled precursors[59] or metal ions[60]. In this PhD thesis, the labelling of nanomotors has been achieved following the second strategy, and using fluorine-18 (^{18}F), iodine-124 (^{124}I) and iodine-131 (^{131}I) as radioisotopes. Therefore, the production, main characteristics and radiolabelling strategies of these radionuclides are briefly described below.

Fluorine-18

Fluorine-18 (^{18}F) is the most widely used positron emitter in research and diagnosis due to its chemical and nuclear properties (see table 1.1). The major advantage of ^{18}F is that it decays almost quantitatively by positron emission (97%), with a low positron energy (635 keV), and low linear range (< 0.3 mm), which are essential parameters to obtain high-resolution PET images. Moreover, ^{18}F has a similar atomic radius to the hydrogen atom, hence it can replace hydrogen in a variety of active molecules without causing steric alterations. ^{18}F-fluorodeoxyglucose (^{18}F-FDG) is the most commonly used radiotracer in clinics for the detection of various neurological disorders or certain types of cancer[61, 62].

In biomedical cyclotrons, ^{18}F can be produced in two different chemical forms: $[^{18}F]F^-$ or $[^{18}F]F_2$, but the first method is the most common. Nucleophilic $[^{18}F]F^-$ is generated by proton irradiation of ^{18}O-enriched water target via the $^{18}O(p,n)^{18}F$ nuclear reaction, while electrophilic $[^{18}F]F_2$ is produced following a 2-step irradiation procedure[63]. Firstly, ^{18}F ions are produced by $^{18}O(p,n)^{18}F$ nuclear reaction on enriched $[^{18}O]O_2$ gas target, and then they are absorbed into the target wall. The $[^{18}O]O_2$ gas is cryogenically recovered, and the target is filled with a mixture of Ne/F_2. A second proton irradiation is produced to induce ^{19}F-^{18}F isotopic exchange reaction with the resulting formation of $[^{18}F]F_2$ gas. Once ^{18}F is produced, it is transferred to the hot cell and used for radiolabelling (Figure 1.8).

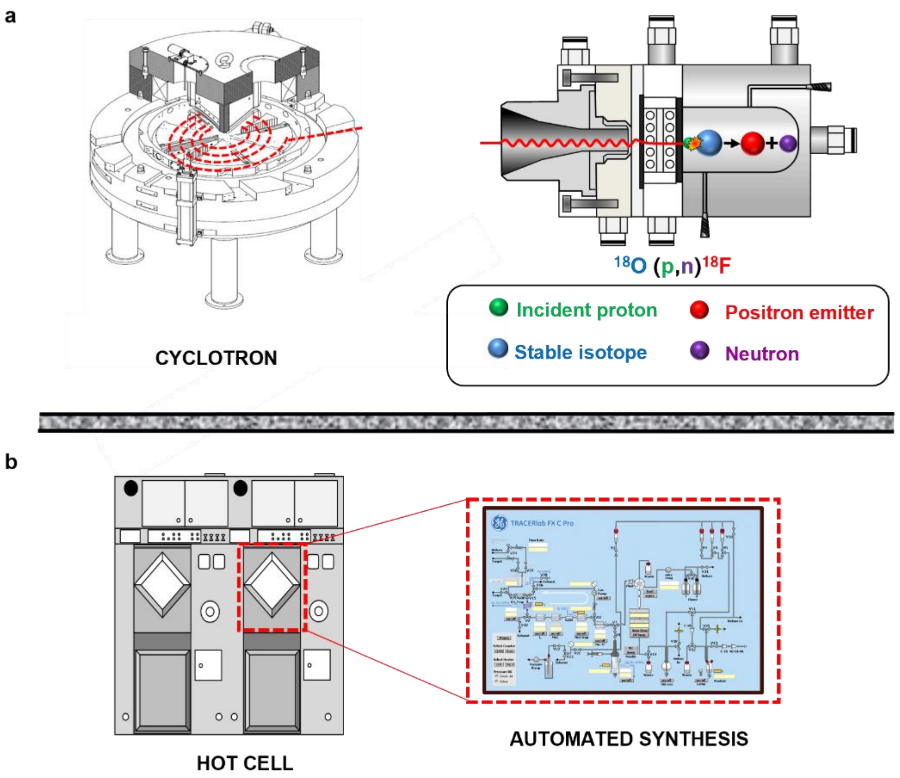

Figure 1.8. Schematic representation of ^{18}F production and radiolabelling process. a) The positron emitter ^{18}F is produced in the cyclotron by proton irradiation of the corresponding target. b) The desired form of ^{18}F is transferred from the cyclotron to the hot cell in the radiochemistry laboratory, where it is transformed in the desired chemical specie by automated synthesis.

^{18}F-labelled radiotracers are commonly prepared from $[^{18}F]F^-$ as labelling agent, and using two possible strategies: direct or indirect fluorination. Direct fluorination consists in the nucleophilic substitution of $[^{18}F]F^-$ on a precursor bearing a good leaving group[64, 65]. Indirect fluorination is normally used for biomolecules or NPs that can be unstable under the harsh condition used for direct fluorination. The latter is based on the radiolabelling of a reactive prosthetic group, which is subsequently attached to the corresponding molecule[66, 67].

In this PhD thesis, indirect fluorination has been selected to radiolabel the urease-powered nanomotors by using a pre-labelled prosthetic group which can react with amino groups present on the enzyme (see Chapter 3).

Iodine (^{124}I and ^{131}I)

Radionuclides of iodine are widely used in nuclear imaging for the labelling of several biomolecules (i.e. antibodies and proteins) when multi-day monitoring is required. Moreover, the labelling chemistry of radioiodine is well stablished. There are mainly four radioisotopes which find application in imaging: ^{123}I, ^{124}I, ^{125}I, and ^{131}I. In this PhD thesis we have focused only in ^{124}I and ^{131}I isotopes.

The ^{124}I radioisotope, as a positron emitter, has a huge potential for use in PET imaging due to its long half-life (4.18 days). Its application range goes from simple imaging of the thyroid gland using Na[^{124}I]I to longitudinal studies of radiolabelled biomolecules such as monoclonal antibodies. However, some of its characteristics can be considered as disadvantages since ^{124}I has a low positron branch and emits high-energy gamma rays (23% and 2140 keV, respectively). As ^{124}I has a long half-life, it can be produced by commercial suppliers and distributed to end users. The main routes for the production of ^{124}I consist of irradiating enriched tellurium-124 targets via $^{124}Te(d,2n)^{124}I$ or $^{124}Te(p,n)^{124}I$ reactions[68]. For the case of ^{131}I, the production is performed in nuclear reactors by neutron irradiation of tellurium dioxide ($^{130}Te\ (n,\gamma)^{131}Te \rightarrow ^{131}I$) or during the fission of uranium ($^{235}U(n,f)^{131}I$)[69]. ^{131}I is a gamma emitter which has a half-life of 8.03 days and decays with 100% beta (606 KeV) and 82% gamma (364 KeV) emissions. Normally, ^{131}I is used as therapeutic agent and not for SPECT imaging because of its high gamma energy and beta particle emission. For diagnosis purposes, ^{131}I can be replaced by ^{123}I, which has shorter half-life (13.2 h) but a lower photon energy (159 KeV), more appropriate for SPECT cameras.

As mentioned, labelling strategies using radioiodine have been widely described. The main labelling strategies comprise: (I) *in situ* oxidation of the anionic species (I^-) using oxidating agents[70, 71], such as Chloramine T or 1,3,4,6-tetrachloro-3α,6α-diphenyl glycoluril (Iodogen). Subsequently, electrophilic aromatic substitution is carried out on aromatic rings activated by the presence of electron-donating groups, *e.g.* tyrosine residues in proteins; (II) indirect method by covalent attachment of a pre-labelled prosthetic group, such as N-succinimidyl 3-(4-hydroxyphenyl) propionate (Bolton-Hunter reagent) which can react with primary amines[72]; and (III) nucleophilic substitution reaction to replace iodine in the target molecule via isotopic exchange[73].

The three methodologies described above have been extensively used in different types of molecules, from small chemical entities to large proteins and antibodies. In the context of this PhD thesis, we have used a different approach based on a previously reported method[74]. This methodology is based on the well-known affinity of iodine towards gold. Thanks to this high affinity, gold nanoparticles (AuNPs) can be labelled with iodine via chemisorption in a fast and efficient way by simple incubation of AuNPs with the radioisotope. This approach has been used to label the AuNPs on the urease-powered nanomotors surface using both ^{124}I and ^{131}I isotopes (see Chapters 3 and 5, respectively).

1.3 Theranostic NPs: Diagnosis and Therapy

As previously stated, the use of medicinal nanotechnology has been explored for decades, and several nanostructures have been developed for a variety of diseases and organs. The possibility of combining NPs for both diagnostic and therapeutic purposes give rise to the term theranostic. The most basic definition of theranostic is the combination of therapeutic and diagnostic agents on a single platform. Another meaning includes the use of theranostic platforms for an appropriate diagnostic methodology to obtain a personalized therapy[75]. This can be done in two forms: (I) therapy followed by diagnostics to corroborate the functionality of the therapy and possible side effects; or (II) diagnostics followed by therapy to identify the type of diseases and provide individualised therapy. Normally, therapeutics and diagnostics agents are two very different entities[75]. Diagnostic platforms are ideally designed to enhance visibility of a specific tissue, and to have a rapid clearance from the living organism. While therapeutic nanoformulations that have been used in clinical trials have a long circulation. Therefore, a common ground needs to be found to develop useful theranostic NPs.

Theranostic NPs have been developed for diverse imaging modalities[76], including optical imaging, magnetic resonance imaging (MRI), ultrasound, and nuclear imaging including both SPECT and PET. Furthermore, different therapeutic strategies can be followed; combining NP with light-sensitive compounds (i.e. phosensitizers), using NPs to induce photothermal effects (i.e. gold NPs), or incorporating active drugs into the NP. In this PhD thesis, we focused on the use of theranostic urease-powered nanomotors combined with nuclear imaging techniques, particularly in the context of radionuclide therapy (RNT).

1.3.1 Radionuclide therapy

Radionuclide therapy (RNT) is based on the delivery of radionuclides, mainly beta (β) or alpha (α) emitters, in tumour cells to cause double-strand breaks in DNA molecules[77] (Figure 1.9). It differs from traditional radiotherapy in the fact that the radiation is not administered from outside the body, but instead is delivered systematically or locally similar to chemotherapy or targeted therapy. The ideal modes of decay for RNT are α o β decay. α-Particles are helium particles which travel 0.05 to 0.1 mm in tissue and deposit energy at a very high density. While β-particles travel 0.8 to 5 mm in tissue and deposit energy at lower density but over a longer range[78]. Both emissions are valid for localised administration of the dose while avoiding putting other organs at risk. A successful treatment is based on the total dose and dose rate delivered to tumour tissue respect to normal tissue. For that reason, prior to therapy, imaging studies are performed using positron or gamma emitters. Thus, information about dose required and potential therapeutic effect can be obtained without exposing the patient to harmful radioactive atoms. For RNT, the ideal situation would be to have high concentration dose and long residence time into the tumours, together with low accumulation and rapid clearance from healthy tissues.

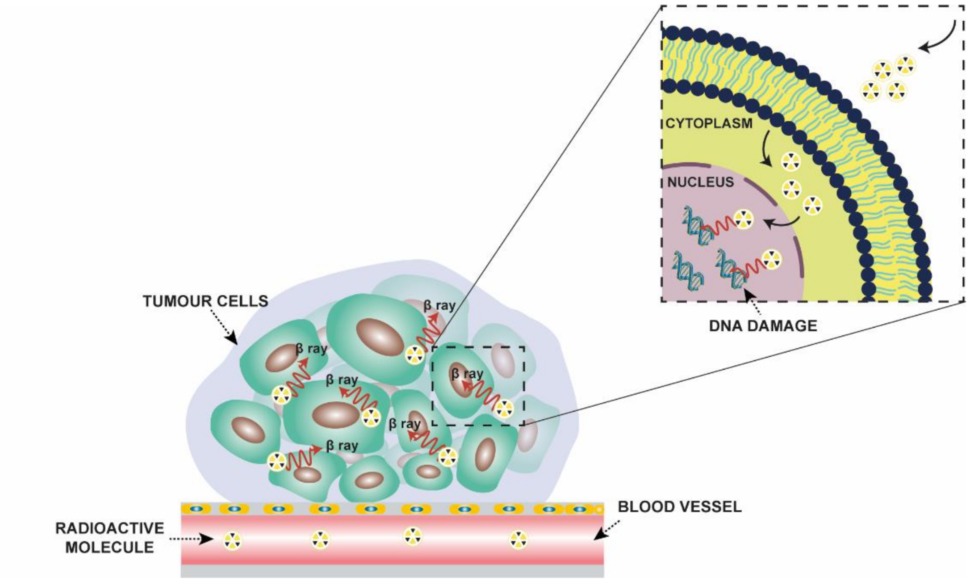

Figure 1.9. Schematic illustration of the mechanism of radionuclide therapy (RNT) using a beta (β) emitter to cause DNA damage.

The typical example of RNT, and which is indeed used clinically, is the use of radioiodine to treat hyperthyroidism and thyroid carcinoma[79]. Thyroid follicular cells and differentiated follicular thyroid cells concentrate iodine via sodium-iodine symporter. The treatment is based on the intravenous administration of ^{131}I (β emitter) for ionizing the corresponding cancer cells. Pre- and post-treatment studies are conducted with ^{123}I (gamma emitter) using a SPECT scanner in combination with CT. The success rate is around 90% but the main drawback of this radiotherapy is that it only works in thyroid cancer[80].

To apply RNT in other types of cancer, more complex structures need to be developed. One option is the combination of radionuclides with vehicles that can target specific sites. Small molecules could be a possibility as the radioisotope can be incorporated into their structure. In fact, the radioiodinated meta-iodobenzylguanidine (^{131}I-mIBG), anologue of the adrenergic neutrotransmitter noradrenaline, is used to treat neuroblastomas[81]. Moreover, peptide-based systems are already used in practice. DOTATOC and DOTATATE are used to treat somatostatin receptor (SSTR)-positive lesions, combining ^{177}Lu or ^{90}Y (β emitters) for radiotherapy and ^{68}Ga (positron emitter) for pre-and post-treatment evaluation[82]. However, these peptide-based systems have a significant accumulation in kidneys, indicating a potential loss of renal function. Other examples are prostate-specific membrane antigen (PSMA) and fibroblast activation protein (FAP) which have demonstrated a potential use for RPT in clinical trials[76, 77].

Nevertheless, both compounds showed high uptake in the kidney, resulting in potential toxicity in that organ.

The ideal radiopharmaceutical should be stable after administration to avoid side effects. NPs could be a potential alternative to the above-mentioned molecular modalities. Indeed, a promising liposomal system able to overcome the main limitations of currently RNT agents, including fast tumour washout, high kidney retention or high accumulation in MPS organs, has been reported in the literature[83]. These results may open new avenues for the use of NPs in RNT.

In this PhD thesis, we have decided to explore the use of urease-powered nanomotors as theranostic agents in bladder cancer (Chapter 5). As far as we know, RNT has not been applied in this field.

1.4 References

(1) Sgouros, G.; Roeske, J. C.; McDevitt, M. R.; Palm, S.; Allen, B. J.; Fisher, D. R.; Brill, A. B.; Song, H.; Howell, R. W.; Akabani, G.; Committee, S. M.; Bolch, W. E.; Brill, A. B.; Fisher, D. R.; Howell, R. W.; Meredith, R. F.; Sgouros, G.; Wessels, B. W.; Zanzonico, P. B., Radiobiology and dosimetry of alpha-particle emitters for targeted radionuclide therapy. *J Nucl Med* **2010,** *51* (2), 311-28.

(2) Khan, I.; Saeed, K.; Khan, I., Nanoparticles: Properties, applications and toxicities. *Arabian Journal of Chemistry* **2019,** *12* (7), 908-931.

(3) Bhatia, S., Nanoparticles Types, Classification, Characterization, Fabrication Methods and Drug Delivery Applications. In *Natural Polymer Drug Delivery Systems: Nanoparticles, Plants, and Algae*, Bhatia, S., Ed. Springer International Publishing: Cham, 2016; pp 33-93.

(4) Gao, C.; Lyu, F.; Yin, Y., Encapsulated Metal Nanoparticles for Catalysis. *Chem Rev* **2021,** *121* (2), 834-881.

(5) Liu, S.; Tang, Z., Nanoparticleassemblies for biological and chemical sensing. *J. Mater. Chem.* **2010,** *20* (1), 24-35.

(6) McNamara, K.; Tofail, S. A. M., Nanoparticles in biomedical applications. *Advances in Physics: X* **2017,** *2* (1), 54-88.

(7) Doane, T. L.; Burda, C., The unique role of nanoparticles in nanomedicine: imaging, drug delivery and therapy. *Chem Soc Rev* **2012,** *41* (7), 2885-911.

(8) Wagner V, H. B., Gaisser S, authors Bock A, editor *Nanomedicine- Drivers for Development and Possible Impacts*; 1018-5593; Luxembourg (Luxembourg): OPOCE, 2008.

(9) Greish, K., Enhanced permeability and retention (EPR) effect for anticancer nanomedicine drug targeting. *Methods Mol Biol* **2010,** *624*, 25-37.

(10) Yang, J.; Jia, C.; Yang, J., Designing Nanoparticle-based Drug Delivery Systems for Precision Medicine. *Int J Med Sci.* **2021,** *18* (13), 2943-2949.

(11) Mitchell, M. J.; Billingsley, M. M.; Haley, R. M.; Wechsler, M. E.; Peppas, N. A.; Langer, R., Engineering precision nanoparticles for drug delivery. *Nat Rev Drug Discov* **2021,** *20* (2), 101-124.

(12) Torchilin, V. P., Targeted pharmaceutical nanocarriers for cancer therapy and imaging. *The AAPS Journal* **2007,** *9* (2), 128-147.

(13) Zhang, L.; Gu Fx Fau - Chan, J. M.; Chan Jm Fau - Wang, A. Z.; Wang Az Fau - Langer, R. S.; Langer Rs Fau - Farokhzad, O. C.; Farokhzad, O. C., Nanoparticles in medicine: therapeutic applications and developments. *Nature* **2008,** *83* (5).

(14) Wilhelm, S.; Tavares, A. J.; Dai, Q.; Ohta, S.; Audet, J.; Dvorak, H. F.; Chan, W. C. W., Analysis of nanoparticle delivery to tumours. *Nature Reviews Materials* **2016,** *1* (5), 16014.

(15) Chalupniak, A.; Morales-Narvaez, E.; Merkoci, A., Micro and nanomotors in diagnostics. *Adv Drug Deliv Rev* **2015,** *95*, 104-16.

(16) Gao, W.; Wang, J., Synthetic micro/nanomotors in drug delivery. *Nanoscale* **2014,** *6* (18), 10486-94.

(17) Sanchez, S.; Soler, L.; Katuri, J., Chemically powered micro- and nanomotors. *Angew Chem Int Ed Engl* **2015,** *54* (5), 1414-44.

(18) Soler, L.; Sánchez, S., Catalytic nanomotors for environmental monitoring and water remediation. *Nanoscale* **2014,** *6* (13), 7175-7182.

(19) Medina-Sánchez, M.; Xu, H.; Schmidt, O. G., Micro- and nano-motors: the new generation of drug carriers. *Therapeutic Delivery* **2018,** *9* (4), 303-316.

(20) Paxton, W. F.; Kistler, K. C.; Olmeda, C. C.; Sen, A.; St Angelo, S. K.; Cao, Y.; Mallouk, T. E.; Lammert, P. E.; Crespi, V. H., Catalytic nanomotors: autonomous movement of striped nanorods. *J Am Chem Soc* **2004,** *126* (41), 13424-31.

(21) Sundararajan, S.; Lammert, P. E.; Zudans, A. W.; Crespi, V. H.; Sen, A., Catalytic Motors for Transport of Colloidal Cargo. *Nano Letters* **2008,** *8* (5), 1271-1276.

(22) Knowles, J. R., Enzyme catalysis: not different, just better. *Nature* **1991,** *350* (6314), 121-124.

(23) Ma, X.; Hortelao, A. C.; Patino, T.; Sanchez, S., Enzyme Catalysis To Power Micro/Nanomachines. *ACS Nano* **2016,** *10* (10), 9111-9122.

(24) Hortelão, A. C.; Patiño, T.; Perez-Jiménez, A.; Blanco, À.; Sánchez, S., Enzyme-Powered Nanobots Enhance Anticancer Drug Delivery. *Advanced Functional Materials* **2018,** *28* (25).

(25) Ma, X.; Zhao, Y.; Ng, K. W.; Zhao, Y., Integrated hollow mesoporous silica nanoparticles for target drug/siRNA co-delivery. *Chemistry* **2013,** *19* (46), 15593-603.

(26) Tang, F.; Li, L.; Chen, D., Mesoporous silica nanoparticles: synthesis, biocompatibility and drug delivery. *Adv Mater* **2012,** *24* (12), 1504-34.

(27) Manzano, M.; Vallet-Regí, M., Mesoporous Silica Nanoparticles for Drug Delivery. *Advanced Functional Materials* **2019,** *30* (2).

(28) Ma, X.; Sánchez, S., Bio-catalytic mesoporous Janus nano-motors powered by catalase enzyme. *Tetrahedron* **2017,** *73* (33), 4883-4886.

(29) Ma, X.; Jannasch, A.; Albrecht, U.-R.; Hahn, K.; Miguel-López, A.; Schäffer, E.; Sánchez, S., Enzyme-Powered Hollow Mesoporous Janus Nanomotors. *Nano Letters* **2015,** *15* (10), 7043-7050.

(30) Ma, X.; Wang, X.; Hahn, K.; Sánchez, S., Motion Control of Urea-Powered Biocompatible Hollow Microcapsules. *ACS Nano* **2016,** *10* (3), 3597-3605.

(31) Sonntag, L.; Simmchen, J. A.-O.; Magdanz, V. A.-O. X., Nano-and Micromotors Designed for Cancer Therapy. *Molecules* **2019,** *24* (18), 3410.

(32) Tu, Y.; Peng, F.; André, A. A.; Men, Y.; Srinivas, M.; Wilson, D. A.-O., Biodegradable Hybrid Stomatocyte Nanomotors for Drug Delivery. *ACS Nano* **2017,** *11* (2), 1957-1963.

(33) Wu, Y.; Lin, X.; Wu, Z.; Möhwald, H.; He, Q., Self-Propelled Polymer Multilayer Janus Capsules for Effective Drug Delivery and Light-Triggered Release. *ACS Applied Materials & Interfaces* **2014,** *6* (13), 10476-10481.

(34) Liu, L.; Mo, H.; Wei, S.; Raftery, D., Quantitative analysis of urea in human urine and s erum by 1H nuclear magnetic resonance. *Analyst* **2012,** *137* (3), 595-600.

(35) Hortelao, A. C.; Carrascosa, R.; Murillo-Cremaes, N.; Patino, T.; Sanchez, S., Targeting 3D Bladder Cancer Spheroids with Urease-Powered Nanomotors. *ACS Nano* **2019,** *13* (1), 429-439.

(36) Bray, F.; Ferlay, J.; Soerjomataram, I.; Siegel, R. L.; Torre, L. A.; Jemal, A., Global cancer statistics 2018: GLOBOCAN estimates of incidence and mortality worldwide for 36 cancers in 185 countries. *CA Cancer J Clin* **2018,** *68* (6), 394-424.

(37) Richters, A.; Aben, K. K. H.; Kiemeney, L., The global burden of urinary bladder cancer: an update. *World J Urol* **2020,** *38* (8), 1895-1904.

(38) Matulewicz, R. S.; Steinberg, G. D., Non-muscle-invasive Bladder Cancer: Overview and Contemporary Treatment Landscape of Neoadjuvant Chemoablative Therapies. *Rev Urol* **2020,** *22* (2).

(39) Wirth, M.; Plattner, V. E.; Gabor, F., Strategies to improve drug delivery in bladder cancer therapy. *Expert Opin Drug Deliv* **2009,** *6* (7), 727-44.

(40) Meyer, R. K.; Williams, S. J.; Lee, T. Y., Mycobacterium bovis infection of a femorofemoral bypass graft following intravesical Bacillus Calmette-Guerin (BCG) immunotherapy. *J Clin Tuberc Other Mycobact Dis* **2020,** *19*, 100152.

(41) Volpe, A.; Racioppi M Fau - D'Agostino, D.; D'Agostino D Fau - Cappa, E.; Cappa E Fau - Filianoti, A.; Filianoti A Fau - Bassi, P. F.; Bassi, P. F., Mitomycin C for the treatment of bladder cancer. *Minerva Urol Nefrol* **2010,** *62* (2), 133-44.

(42) Svatek, R. S.; Hollenbeck, B. K.; Holmang, S.; Lee, R.; Kim, S. P.; Stenzl, A.; Lotan, Y., The economics of bladder cancer: costs and considerations of caring for this disease. *Eur Urol* **2014,** *66* (2), 253-62.

(43) Xu, X.; Liu, K.; Jiao, B.; Luo, K.; Ren, J.; Zhang, G.; Yu, Q.; Gan, Z., Mucoadhesive nanoparticles based on ROS activated gambogic acid prodrug for safe and efficient intravesical instillation chemotherapy of bladder cancer. *J Control Release* **2020,** *324*, 493-504.

(44) Bilensoy, E.; Sarisozen, C.; Esendagli, G.; Dogan, A. L.; Aktas, Y.; Sen, M.; Mungan, N. A., Intravesical cationic nanoparticles of chitosan and polycaprolactone for the delivery of Mitomycin C to bladder tumors. *Int J Pharm* **2009,** *371* (1-2), 170-6.

(45) Mugabe, C.; Matsui, Y.; So, A. I.; Gleave, M. E.; Baker, J. H.; Minchinton, A. I.; Manisali, I.; Liggins, R.; Brooks, D. E.; Burt, H. M., In vivo evaluation of mucoadhesive nanoparticulate docetaxel for intravesical treatment of non-muscle-invasive bladder cancer. *Clin Cancer Res* **2011,** *17* (9), 2788-98.

(46) Rieger, C.; Kunhardt, D.; Kaufmann, A.; Schendel, D.; Huebner, D.; Erdmann, K.; Propping, S.; Wirth, M. P.; Schwenzer, B.; Fuessel, S.; Hampel, S., Characterization of different carbon nanotubes for the development of a mucoadhesive drug delivery system for intravesical treatment of bladder cancer. *Int J Pharm* **2015,** *479* (2), 357-63.

(47) Kaldybekov, D. B.; Tonglairoum, P.; Opanasopit, P.; Khutoryanskiy, V. V., Mucoadhesive maleimide-functionalised liposomes for drug delivery to urinary bladder. *Eur J Pharm Sci* **2018,** *111*, 83-90.

(48) Wang, B.; Zhang, K.; Wang, J.; Zhao, R.; Zhang, Q.; Kong, X., Poly(amidoamine)-modified mesoporous silica nanoparticles as a mucoadhesive drug delivery system for potential bladder cancer therapy. *Colloids Surf B Biointerfaces* **2020,** *189*, 110832.

(49) Levy, M.; Luciani, N.; Alloyeau, D.; Elgrabli, D.; Deveaux, V.; Pechoux, C.; Chat, S.; Wang, G.; Vats, N.; Gendron, F.; Factor, C.; Lotersztajn, S.; Luciani, A.; Wilhelm, C.; Gazeau, F., Long term in vivo biotransformation of iron oxide nanoparticles. *Biomaterials* **2011,** *32* (16), 3988-3999.

(50) Girish, C. M.; Sasidharan, A.; Gowd, G. S.; Nair, S.; Koyakutty, M., Confocal Raman imaging study showing macrophage mediated biodegradation of graphene in vivo. *Adv Healthc Mater* **2013,** *2* (11), 1489-500.

(51) Simpson, C. A.; Salleng, K. J.; Cliffel, D. E.; Feldheim, D. L., In vivo toxicity, biodistribution, and clearance of glutathione-coated gold nanoparticles. *Nanomedicine* **2013,** *9* (2), 257-63.

(52) Lamb, J.; Holland, J. P., Advanced Methods for Radiolabeling Multimodality Nanomedicines for SPECT/MRI and PET/MRI. *J Nucl Med* **2018,** *59* (3), 382-389.

(53) Pratt, E. C.; Shaffer, T. M.; Grimm, J., Nanoparticles and radiotracers: advances toward radionanomedicine. *Wiley Interdiscip Rev Nanomed Nanobiotechnol* **2016,** *8* (6), 872-890.

(54) Stockhofe, K.; Postema, J. M.; Schieferstein, H.; Ross, T. L., Radiolabeling of Nanoparticles and Polymers for PET Imaging. *Pharmaceuticals (Basel)* **2014,** *7* (4), 392-418.

(55) Pérez-Campaña, C.; Gómez-Vallejo, V.; Puigivila, M.; Martín, A.; Calvo-Fernández, T.; Moya, S. E.; Ziolo, R. F.; Reese, T.; Llop, J., Biodistribution of Different Sized Nanoparticles Assessed by Positron Emission Tomography: A General Strategy for Direct Activation of Metal Oxide Particles. *ACS Nano* **2013,** *7* (4), 3498-3505.

(56) Hirn, S.; Semmler-Behnke, M.; Schleh, C.; Wenk, A.; Lipka, J.; Schäffler, M.; Takenaka, S.; Möller, W.; Schmid, G.; Simon, U.; Kreyling, W. G., Particle size-dependent and surface charge-dependent biodistribution of gold nanoparticles after intravenous administration. *European Journal of Pharmaceutics and Biopharmaceutics* **2011,** *77* (3), 407-416.

(57) Smiley, S. A.-O.; Yun, Y.; Ayyagari, P.; Shannon, H. E.; Pollok, K. E.; Vannier, M. A.-O. X.; Das, S. A.-O. X.; Veronesi, M. A.-O. X., Development of CD133 Targeting Multi-Drug Polymer Micellar Nanoparticles for Glioblastoma - In Vitro Evaluation in Glioblastoma Stem Cells. *Pharm Res* **2021,** *38* (6), 1067-1079.

(58) Feiner, I. V. J.; Pulagam, K. R.; Uribe, K. B.; Passannante, R.; Simo, C.; Zamacola, K.; Gomez-Vallejo, V.; Herrero-Alvarez, N.; Cossio, U.; Baz, Z.; Caffarel, M. M.; Lawrie, C. H.; Vugts, D. J.; Rejc, L.; Llop, J., Pre-targeting with ultra-small nanoparticles: boron carbon dots as drug candidates for boron neutron capture therapy. *J Mater Chem B* **2021,** *9* (2), 410-420.

(59) Andreozzi, P.; Simo, C.; Moretti, P.; Porcel, J. M.; Ludtke, T. U.; Ramirez, M. L. A.; Tamberi, L.; Marradi, M.; Amenitsch, H.; Llop, J.; Ortore, M. G.; Moya, S. E., Novel Core-Shell Polyamine Phosphate Nanoparticles Self-Assembled from PEGylated Poly(allylamine hydrochloride) with Low Toxicity and Increased In Vivo Circulation Time. *Small* **2021,** *17* (35), e2102211.

(60) Suárez-García, S.; Esposito, T. V. F.; Neufeld-Peters, J.; Bergamo, M.; Yang, H.; Saatchi, K.; Schaffer, P.; Häfeli, U. O.; Ruiz-Molina, D.; Rodríguez-Rodríguez, C.; Novio, F., Hybrid Metal–Phenol Nanoparticles with Polydopamine-like Coating for PET/SPECT/CT Imaging. *ACS Applied Materials & Interfaces* **2021,** *13* (9), 10705-10718.

(61) Shooli, H.; Assadi, M.; Aboian, M., [18F]-FDG PET/MR Neuroimaging: Focus on Neuro-Oncology Applications. In *Hybrid PET/MR Neuroimaging: A Comprehensive Approach*, Franceschi, A. M.; Franceschi, D., Eds. Springer International Publishing: Cham, 2022; pp 89-98.

(62) Vallabhajosula, S., (18)F-labeled positron emission tomographic radiopharmaceuticals in oncology: an overview of radiochemistry and mechanisms of tumor localization. *Semin Nucl Med* **2007,** *37* (6), 400-19.

(63) Roberts, A. D.; Oakes Tr Fau - Nickles, R. J.; Nickles, R. J., Development of an improved target for [18F]F2 production. *Applied Radiation and Isotopes* **1995,** *46* (2), 87-91.

(64) Iwata, R.; Terasaki, K.; Ishikawa, Y.; Harada, R.; Furumoto, S.; Yanai, K.; Pascali, C., A concentration-based microscale method for 18F-nucleophilic substitutions and its testing on the one-pot radiosynthesis of [18F]FET and [18F]fallypride. *Applied Radiation and Isotopes* **2020,** *166*, 109361.

(65) Wang, C.; Zhang, L.; Mou, Z.; Feng, W.; Li, Z.; Yang, H.; Chen, X.; Lv, S.; Li, Z., Direct 18F-Labeling of Biomolecules via Spontaneous Site-Specific Nucleophilic Substitution by F– on Phosphonate Prostheses. *Organic Letters* **2021,** *23* (11), 4261-4266.

(66) Jacobson, O.; Wang, Z.; Yu, G.; Ma, Y.; Chen, X.; Kiesewetter, D. O., 3-18F-fluoropropane-1-thiol and 18F-PEG4-1-thiol: Versatile prosthetic groups for radiolabeling maleimide functionalized peptides. *Bioorganic & Medicinal Chemistry* **2019,** *27* (19), 115041.

(67) Olberg, D. E.; Arukwe, J. M.; Grace, D.; Hjelstuen, O. K.; Solbakken, M.; Kindberg, G. M.; Cuthbertson, A., One Step Radiosynthesis of 6-[18F]Fluoronicotinic Acid 2,3,5,6-

Tetrafluorophenyl Ester ([18F]F-Py-TFP): A New Prosthetic Group for Efficient Labeling of Biomolecules with Fluorine-18. *Journal of Medicinal Chemistry* **2010,** *53* (4), 1732-1740.

(68) Braghirolli, A. M.; Waissmann, W.; da Silva, J. B.; dos Santos, G. R., Production of iodine-124 and its applications in nuclear medicine. *Applied Radiation and Isotopes* **2014,** *90*, 138-48.

(69) Elom Achoribo, A. S.; Akaho Eh Fau - Nyarko, B. J. B.; Nyarko Bj Fau - Osae Shiloh, K. D.; Osae Shiloh Kd Fau - Odame Duodu, G.; Odame Duodu G Fau - Gibrilla, A.; Gibrilla, A., Feasibility study for production of I-131 radioisotope using MNSR research reactor. *Applied Radiation and Isotopes* **2012,** *70* (1), 76-80.

(70) Guo, J.; Feng, K.; Wu, W.; Ruan, Y.; Liu, H.; Han, X.; Shao, G.; Sun, X. A.-O., Smart (131) I-Labeled Self-Illuminating Photosensitizers for Deep Tumor Therapy. *Angew Chem Int Ed Engl* **2021,** *60* (40), 21884-21889.

(71) Sanad, M. H.; Rizvi, S. F. A.; Farag, A. B., Radiosynthesis and in silico bioevaluation of (131) I-Sulfasalazine as a highly selective radiotracer for imaging of ulcerative colitis. *Chem Biol Drug Des* **2021,** *98* (5), 751-761.

(72) Bolton Ae Fau - Hunter, W. M.; Hunter, W. M., The labelling of proteins to high specific radioactivities by conjugation to a 125I-containing acylating agent. *Biochemical Journal* **1973,** *133* (3), 529-538.

(73) Weichert, J. P.; Van Dort, M. E.; Groziak, M. P.; Counsell, R. E., Radioiodination via isotope exchange in pivalic acid. *International Journal of Radiation Applications and Instrumentation. Part A. Applied Radiation and Isotopes* **1986,** *37* (8), 907-913.

(74) Zhang, Y. A.-O.; Zhang, Y. A.-O.; Yin, L. A.-O.; Xia, X.; Hu, F. A.-O. X.; Liu, Q. A.-O.; Qin, C. A.-O.; Lan, X. A.-O., Synthesis and Bioevaluation of Iodine-131 Directly Labeled Cyclic RGD-PEGylated Gold Nanorods for Tumor-Targeted Imaging. *Contrast Media Mol Imaging* **2017,** *6081724*.

(75) Janib, S. M.; Moses, A. S.; MacKay, J. A., Imaging and drug delivery using theranostic nanoparticles. *Adv Drug Deliv Rev* **2010,** *62* (11), 1052-1063.

(76) Zavaleta, C.; Ho, D.; Chung, E. J., Theranostic Nanoparticles for Tracking and Monitoring Disease State. *SLAS Technol* **2018,** *23* (3), 281-293.

(77) Sgouros, G.; Bodei, L.; McDevitt, M. R.; Nedrow, J. R., Radiopharmaceutical therapy in cancer: clinical advances and challenges. *Nature Reviews Drug Discovery* **2020,** *19* (9), 589-608.

(78) St James, S.; Bednarz, B.; Benedict, S.; Buchsbaum, J. C.; Dewaraja, Y.; Frey, E.; Hobbs, R.; Grudzinski, J.; Roncali, E.; Sgouros, G.; Capala, J.; Xiao, Y., Current Status of Radiopharmaceutical Therapy. *Int J Radiat Oncol Biol Phys* **2021,** *109* (4), 891-901.

(79) Griggs, W. S.; Divgi, C., Radioiodine imaging and treatment in thyroid disorders. *Neuroimaging Clin N Am* **2021,** *31* (3), 337-344.

(80) Llop, J.; Lammers, T., Nanoparticles for Cancer Diagnosis, Radionuclide Therapy and Theranostics. *ACS Nano* **2021,** *15* (11), 16974-16981.

(81) Kayano, D.; Kinuya, S. A.-O., Iodine-131 metaiodobenzylguanidine therapy for neuroblastoma: reports so far and future perspective. *ScientificWorldJournal* **2015,** *189135*.

(82) Fani, M.; Nicolas, G. P.; Wild, D., Somatostatin Receptor Antagonists for Imaging and Therapy. *J Nucl Med* **2017,** *58* (2), 61-66.

(83) Lee, W.; Il An, G.; Park, H.; Sarkar, S.; Ha, Y. S.; Huynh, P. T.; Bhise, A.; Bhatt, N.; Ahn, H.; Pandya, D. N.; Kim, J. Y.; Kim, S.; Jun, E.; Kim, S. C.; Lee, K. C.; Yoo, J., Imaging Strategy that Achieves Ultrahigh Contrast by Utilizing Differential Esterase Activity in Organs: Application in Early Detection of Pancreatic Cancer. *ACS Nano* **2021,** *15*, 17348-17360.

CHAPTER 2

MOTIVATION AND OBJECTIVES OF THE THESIS

Chapter 2: Motivation and objectives of the thesis

2.1 Justification of the study and hypothesis

As mentioned in Chapter 1, micro- and nanomotors (MNMs) have emerged as new generation of nanoparticles (NPs) capable of generating autonomous motion in fluidic environments. Few examples have been reported on the tracking and quantification of MNMs *in vivo*, which is an important parameter for their possible translation in biomedical applications. In 2018, the Smart nano-bio-devices group led by Prof. Samuel Sánchez at Institute for Bioengineering of Catalonia (IBEC), in collaboration with our group, the Radiochemistry and Nuclear Imaging Group at CIC biomaGUNE led by Dr. Jordi Llop, reported for the first time the use of positron emission tomography (PET) in combination with computerized tomography (CT) to monitor the movement of tubular gold/poly(3,4-ethylenedioxythiophene)/platinum (Au/PEDOT/Pt) micromotors in cylindrical phantoms. This work published in *ACS nano*[1] showed the suitability of using nuclear imaging techniques to detect and quantify MNMs *in vitro*, becoming a good approach for their tracking *in vivo*. However, the movement of these micromotors is promoted by the catalytic oxidation of H_2O_2, which is a toxic fuel for biological systems, making difficult their use in biomedical applications.

Recently, and with the objective to use MNMs in biomedicine, new efforts have been directed towards developing MNMs whose self-propulsion is generated from endogenous fuels. In this context, enzyme-powered nanomotors have gained much attention due to their biocompatibility and possibility of designing enzymatic nanomotors upon demand. In fact, our collaborator (Prof. Samuel Sánchez) has demonstrated the potential of using urease-powered nanomotors, whose movement is promoted by the hydrolysis of urea, to target bladder cancer cells spheroids[2].

Because urea is present in urine, the consideration of using urease-powered nanomotors as diagnostic, therapeutic or even theranostic tools with application in bladder cancer, is a natural evolution of the results achieved before the start of this PhD thesis. In this context, the following hypotheses were established:

1- Positron emission tomography (PET) is a suitable tool for the *in vivo* and non-invasive monitoring of the collective motion of urease-powered nanomotors after intravesical administration.
2- Self-propelling capacity enhances tumour uptake of nanomotors, and such enhanced uptake can be quantified using PET imaging.

3- Increased tumour uptake capacity results in higher therapeutic efficacy when a beta emitter is incorporated into the nanomotors.

2.2 Objectives

To prove our hypotheses, we established the following specific objectives:

1. To develop radiolabelling strategies for the incorporation of fluorine-18 and iodine-124 to urease and BSA nanomotors to enable their tracking by using PET imaging.
2. To study the collective behaviour of urease and BSA nanomotors both *in vitro* and i*n vivo* by using PET imaging.
3. To evaluate the *in vivo* tumour acumulation of urease and BSA nanomotors, after intravesical administration, in an orthotopic mouse model of bladder cancer by using PET imaging and *ex vivo* complementary techniques.
4. To develop a radiolabelling strategy for the incorporation of iodine-131 to urease nanomotors, and evaluate their therapeutic capacity in an orthotopic mouse model of bladder cancer by using MRI.

2.3 References

(1) Vilela, D.; Cossio, U.; Parmar, J.; Martinez-Villacorta, A. M.; Gomez-Vallejo, V.; Llop, J.; Sanchez, S., Medical Imaging for the Tracking of Micromotors. *ACS Nano* **2018,** *12* (2), 1220-1227.

(2) Hortelao, A. C.; Carrascosa, R.; Murillo-Cremaes, N.; Patino, T.; Sanchez, S., Targeting 3D Bladder Cancer Spheroids with Urease-Powered Nanomotors. *ACS Nano* **2019,** *13* (1), 429-439.

CHAPTER 3

RADIOLABELLING AND *IN VITRO* AND *IN VIVO* MONITORING OF UREASE-POWERED NANOMOTORS

Chapter 3: Radiolabelling and *In vitro* and *in vivo* monitoring of urease-powered nanomotors

3.1 Introduction

In the last years, the emergence of nanotechnology has received a considerable interest due to its impact on the treatment of various diseases[1]. One of the most studied applications is the use of nano-sized systems as tools to increase efficacy and minimize side effects in cancer treatment. A wide range of examples of nanomaterials applied to drug delivery, including liposomes, polymeric nanoparticles, dendrimers, and nanoemulsions, among others, have been reported in the literature[2]. Nanoparticles (NPs) can indeed be loaded with drugs and surface-decorated with a large variety of functionalities, thus acting as targeted drug delivery agents capable to improve stability, solubility of encapsulated drugs, extend circulation lifetime, and transport across membranes and accumulate to the target site[3, 4]. Nevertheless, the major challenge of common drug delivery systems is the penetration on tissues and cellular barriers. Indeed, a recent study determined that, when considering nanomaterials as drug delivery agents, only 0.7% of the injected doses reach their target *in vivo* after parenteral administration[5]. In this context, self-propelled materials have emerged to overcome these limitations and increase drug efficiency.

As mentioned in the introduction of this PhD thesis, Micro- and nanomotors (MNMs) are micro- and nano-devices capable to self-propel in fluidic environments. The field has evolved over time since the first reported MNMs based on the catalytic oxidation of H_2O_2[6]. In nanomedicine, MNMs have demonstrated enhanced targeting properties[7, 8] and superior drug delivery efficiency compared to traditional particles[9, 10], showing the potential of these swimmers for biomedical applications. Recently, efforts have been focused on designing biocompatible MNMs using enzymes as biocatalysts. The use of enzymes to design self-propelled particles has several advantages respect to other catalytic motors due to the use of biocompatible fuels. Moreover, the extended library of enzyme/substrate combinations allows the design of enzymatic motors upon demand. For instance, MNMs based on mesoporous silica, which is an optimal material for biomedical applications, coupled with enzymes to produce the self-propulsion by the biocatalytic conversion of urea and glucose, which are substrates available in the body[11, 12], show promise as biocompatible self-propelled systems. Particularly, urease-powered nanomotors, which can move in the presence of urea, have demonstrated promising results for the active targeting of bladder cancer cells[8], thus becoming promising candidates for the diagnosis and treatment of bladder cancer.

One critical point when developing new therapeutic agents is the assessment of the amount of drug that reaches the tumour before they can be safely applied on real clinical settings. A possible strategy to quantify the time-resolved concentration of active agent after administration consist of determining the concentration in the resected tumour at different time points after drug administration. Nevertheless, longitudinal evaluation is not feasible, and a significant number of animals is required. To overcome this problem, a good option can be the use of *in vivo* imaging modalities, which are non-invasive techniques capable of tracking NPs after administration. In the context of MNMs, magnetic resonance imaging (MRI)[13, 14], fluorescence (FL) imaging [15, 16], photoacoustic computed tomography (PACT)[17], and ultrasound (US) imaging[18] have been used to track MNMs *in vivo*. However, these imaging techniques have insufficient sensitivity, and they fail to provide quantitative information. A promising alternative is the incorporation of a positron or gamma emitter into MNMs to be tracked using nuclear imaging techniques: positron emission tomography (PET) or single photon emission computerized tomography (SPECT). These non-invasive nuclear imaging techniques are fully translational and enable absolute quantification of the radiolabelled specie at the whole-body level both in preclinical and clinical stages. Moreover, they are extremely sensitive, thus providing high-quality images by administering subpharmacological doses of the radiolabelled entity. Both PET and SPECT in combination with computed tomography (CT) to provide anatomical information, are widely used in clinical settings and can be a good approach for tracking MNMs *in vivo*. However, the application of nuclear imaging techniques to the *in vivo* tracking of self-propelled particles has barely been explored. In a previous study carried out in our research group, the suitability of PET-CT to track the movement of tubular gold/poly(3,4-ethylenedioxythiophene)/platinum (Au/PEDOT/Pt) micromotors in cylindrical phantoms has been demonstrated[20]. In this work, radiolabelling was achieved by chemisorption of ^{124}I into micromotor's gold surface.

In this chapter, we go one step further to overcome the problems associated to the track of motors, not only *in vitro* but also *in vivo*. We describe the application of radiolabelling and PET imaging to achieve the time-resolved tracking of mesoporous silica nanoparticles (MSNP) containing urease enzymes and gold nanoparticles (AuNPs) as nanomotors. Our approach consists of the radiolabelling of nanomotors using two radionuclides, fluorine-18 (^{18}F; half-life = 119.7 min) and iodine-124 (^{124}I; half-life = 4.2 days) (Figure 3.1, left).

After radiolabelling, four different PET-CT studies were performed, both *in vitro* and *in vivo* (Figure 3.1, right). *In vitro* imaging studies were carried out using Petri dish- and 3D printed phantoms to investigate the self-propelling capacity of labelled nanomotors in the presence and absence of the fuel (urea). Then, *in vivo* experiments in healthy mice were performed using two administration routes: intravenous and intravesical. Firstly, stability of the radiolabel and whole-body distribution were investigated after intravenous administration. Then, envisioning the use of this urease-powered nanomotors for bladder cancer, their motile properties were studied after intravesical instillation. Additional control experiments were performed using bovine serum albumin (BSA)-modified particles (BSA nanomotors), which do not have motile properties, to corroborate our hypothesis. The resulting PET-CT results demonstrated the capability of these urease-powered nanomotors to self-propel in the presence of urea, both *in vitro* and *in vivo*, and their potential to be used in clinical settings.

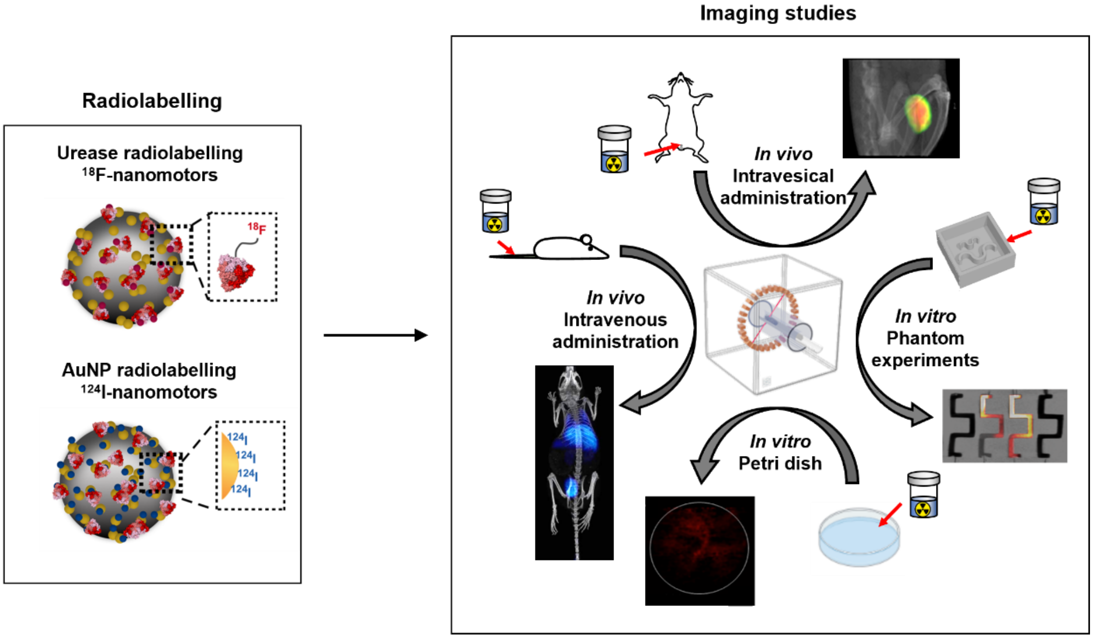

Figure 3.1. Summary of the radiolabelling strategies to yield ^{18}F-urease nanomotors and urease ^{124}I-nanomotors (left) and the imaging studies performed *in vitro* and *in vivo* (right).

3.2 Objectives

The specific objectives of this chapter are:

1. To radiolabel urease-powered nanomotors using two positron emitters: ^{124}I and ^{18}F.
2. To investigate the collective movement of urease ^{124}I-nanomotors and ^{18}F-urease nanomotors in a urea-rich environment using *in vitro* PET imaging.
3. To demonstrate the suitability of *in vivo* PET imaging to track nanomotors and evaluate their *in vivo* stability after intravenous and intravesical administration.

3.3 Materials and methods

3.3.1 General Remarks

The nanomotors used in the *in vitro* and *in vivo* studies were synthetized by the Smart Nano-Bio-Devices group led by Prof. Samuel Sánchez from Institute for Bioengineering of Catalonia, IBEC (Barcelona, Spain). A brief description of their preparation and characterization is provided in this PhD thesis. Phantom fabrication was also carried out at IBEC.

3.3.2 Synthesis of nanomotors

3.3.2.1 Synthesis of MSNPs

MSNPs that serve as chassis for the fabrication of the nanomotors were synthesized by sol-gel chemistry using a modification of the Stöber method[21]. In brief, a mixture of triethanolamine (TEOA; 35 g), ultrapure water (20 mL), and hexadecyltrimethylammonium bromide (CTAB; 570 mg) was placed in a three-mouthed round-bottom flask and heated up to 95°C in a silicon oil bath, under reflux and stirring, for 30 minutes. After this, Tetraethyl orthosilicate (TEOS; 1.5 mL) was added dropwise. The reaction took place for 2 hours, and then the resulting MSNPs were collected by centrifugation and washed in ethanol (three times, 1350g, 5 min). The CTAB was then removed by reflux in acidic methanol. For this, the MSNPs were suspended in methanol (30 mL) and hydrochloric acid (1.8 mL) mixture, placed in one-mouthed round-bottom flask in silicon oil bath at 80°C, and refluxed for 24 hours. Last, the MSNPs were collected by centrifugation and washed thrice in ethanol and thrice in ultrapure water (1350g, 5 min). The concentration of the final dispersion was evaluated by dry weighting.

3.3.2.2 Amine modifications of MSNPs

The surface of the MSNPs was then modified to carry free amino groups, using a modification of a reported method[22]. In brief, a suspension of MSNPs (2 mg/ml) in water was placed in a round-bottom flask and heated up to 50°C under vigorous stirring. Then, (3-aminopropyl)triethoxysilane (APTES) was added to the dispersion to a final concentration of 5 mM. The reaction took place under reflux, at 50°C, for 24 hours, after which point the MSNP-NH_2 were collected and washed thrice in water by centrifugation (1350g, 5 min). The concentration of the final dispersion was evaluated by dry weighing.

3.3.2.3 Synthesis of AuNPs

The AuNPs were synthesized according to a previously reported method[23, 24]. In brief, all necessary materials were cleaned using freshly prepared aqua regia and then rinsed extensively with water and dried in air. Then, a solution of 1 mM gold (III) chloride trihydrate ($HAuCl_4$) was heated up to a boil under stirring, in a round-bottom flask integrated in a reflux system. After this, 10 ml of a sodium citrate solution (NaCit; 38.8 mM) were added, and the solution was boiled for 20 min, turning red in colour. The solution was stirred without heating for 1 hour, reaching room temperature. The resulting AuNP dispersion was stored at room temperature in the dark. The Z-potential of the synthesized AuNPs in water was −40.26 ± 2.23 mV, and their hydrodynamic radii were 10.4 ± 0.1 nm (n = 10).

3.3.2.4 Fabrication of urease nanomotors

The MSNP-NH_2 were resuspended in PBS (10 mM, pH 7.4) at a concentration of 1 mg/ml and a total volume of 900 μl and activated with glutaraldehyde (GA; 100 μl). The reaction took place for 2.5 hours, at room temperature, under mixing in an end-to-end shaker. After this, the activated MSNP-NH_2 were collected and washed in phosphate buffered saline (PBS; 10 mM, pH 7.4) thrice by centrifugation (1350g, 5 min), lastly being resuspended in a solution of urease (3 mg/ml) and heterobifunctional PEG (1 μg PEG/mg of MSNP-NH_2) in PBS (10 mM, pH 7.4). This mixture was left reacting in an end-to-end shaker for 24 hours at room temperature. The resulting nanomotors were then collected and washed three times in PBS (10 mM, pH 7.4) by centrifugation (1350g, 5 min). Then, these nanomotors were resuspended in a dispersion of AuNPs and left rotating in an end-to-end shaker for 10 min, followed by thorough washing by centrifugation (five times, 1350g, 5 min). Hydrodynamic size distribution and surface charge of the MSNPs, MSNP-NH_2, GA-activated MSNP-NH_2, nanomotors, and AuNPs-decorated nanomotors were determined using a Wyatt Möbius DLS system and a Malvern Zetasizer, respectively. AuNPs were also characterized by transmission electron microscopy (TEM).

3.3.2.5 Fabrication of BSA nanomotors

The fabrication of BSA nanomotors was prepared following the same procedure described above for the urease-powered nanomotors, but BSA was used instead of urease.

3.3.3 Radiolabelling of urease nanomotors

3.3.3.1 Radiolabelling of urease nanomotors with [^{18}F]F-PyTFP (^{18}F-urease nanomotors)

Synthesis of [^{18}F]F-PyTFP

[^{18}F]F-PyTFP was synthesized using a TRACERlab FX-FN synthesis module (GE Healthcare, Waukesha, WI, USA), following a previously described procedure with modifications[25] (Scheme 3.1). In brief, aqueous [^{18}F]fluoride was first trapped in an ion-exchange resin (Sep-Pak® Accell Plus QMA Light, Milford, MA, USA) and subsequently eluted to the reactor vessel with a solution of Kryptofix $K_{2.2.2}$/K_2CO_3 in a mixture of water and acetonitrile. After azeotropic drying of the solvent, a solution of F-PyTFP (10 mg) in a mixture of *tert*-butanol and acetonitrile (4/1) was added and heated at 40°C for 15 min. The reaction mixture was then diluted with 1 mL of acetonitrile and 1 mL of water, and purified by high performance liquid chromatography (HPLC) using a Nucleosil 100-7 C18 column (Machery-Nagel, Düren, Germany) as stationary phase and 0.1% trifluoroacetic acid (TFA)/acetonitrile (25/75) as the mobile phase at a flow rate of 3 mL/min. The desired fraction (retention time = 22-23 minutes; [^{18}F]F-PyTFP) was collected, diluted with ultrapure water (25 mL), and flushed through a C18 cartridge (Sep-Pak® Light, Waters, Milford, MA, USA) to selectively retain [^{18}F]F-PyTFP. The desired labelled specie was finally eluted with acetonitrile (1 mL). Radiochemical purity was determined by radio-HPLC, using an Agilent 1200 Series chromatograph equipped with a multiple wavelength UV detector (λ = 254 nm) and a Gabi radiometric detector (Raytest Gmbh, Radeberg, Germany) connected in series. A Mediterranean C18 column (4.6 x 150 mm, 5 µm) was used as stationary phase and 0.1% TFA/acetonitrile (0-1 min 25% acetonitrile; 1-9 min 25-90% acetonitrile; 9-12 min 90% acetonitrile; 12-13 min 90-25% acetonitrile; 13-15 min 25% acetonitrile) as the mobile phase at a flow rate of 1.5 mL/min (retention time = 7.5 minutes).

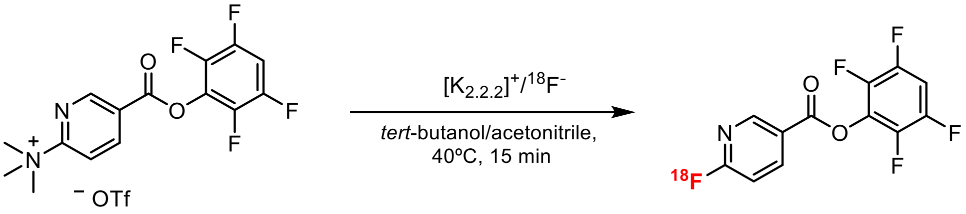

Scheme 3.1. Synthesis of the prosthetic group [^{18}F]F-PyTFP.

Radiolabelling of urease nanomotors with ^{18}F

The radiofluorination of urease nanomotors with ^{18}F was carried out by the reaction between the free amine groups of urease (*i.e.* present in lysine residues) present at the surface of the nanomotors and [^{18}F]F-PyTFP. In brief, 200 µL of urease nanomotors solution (1 mg/mL) were centrifuged (16162g, 10 min), re-suspended in PBS (10 µL, 10 mM pH 8) and mixed with 4 µL of [^{18}F]F-PyTFP in acetonitrile (*ca.* 74 MBq). The reaction mixture was incubated at room temperature for 35 min. After incubation, the reaction crude was diluted with water (100 µL) and purified by centrifugation (16162g, 5 min). The resulting precipitate was washed three times with water. The amount of radioactivity in the supernatant and the precipitate were determined in a dose calibrator (CPCRC-25R, Capintec Inc., NJ, USA) and analysed with radio-thin layer chromatography (radio-TLC) using iTLC-SG chromatography paper (Agilent Technologies, CA, USA) and dichloromethane and methanol (2:1) as the stationary and mobile phases, respectively. TLC plates were analysed using a TLC-reader (MiniGITA, Raytest, Straubenhardt, Germany).

3.3.3.2 Radiolabelling of urease nanomotors with ^{124}I (^{124}I-urease nanomotors)

The radioiodination of urease nanomotors was performed by incubation with [^{124}I]NaI (solution in 0.1M NaOH), purchased from Perkin Elmer. In brief, 200 µL of urease nanomotors solution (1 mg/mL) diluted in 100 µL of water and 8 µL of [^{124}I]NaI (*ca*. 11 MBq) were incubated at room temperature for 30 min. After incubation, the reaction mixture was purified by centrifugation (5 minutes, 16162g). The resulting precipitate was washed three times with water (100 µL). The amount of radioactivity in the supernatant and the precipitate were determined in a dose calibrator (CPCRC-25R, Capintec Inc., NJ, USA) and analysed with radio-TLC, using iTLC-SG chromatography paper (Agilent Technologies, CA, USA) and dichloromethane and methanol (2:1) as the stationary and mobile phases, respectively. TLC plates were analysed using TLC-reader (MiniGITA, Raytest).

3.3.4 Radiolabelling of BSA nanomotors with [^{18}F]F-PyTFP (^{18}F-BSA nanomotors)

The radiofluorination of BSA nanomotors with ^{18}F was carried out following the same procedure for urease nanomotors described above.

3.3.5 *In vitro* PET-CT studies

In vitro imaging studies were conducted using MOLECUBES β-CUBE (PET) and MOLECUBES X-CUBE (CT) scanner (MOLECUBES, Gent, Belgium).

Petri dish

Preliminary studies of the swarming behaviour of nanomotors were obtained using a Petri dish. For this, ^{18}F-urease nanomotors were resuspended in 200 µL of either pure water or a 300 mM solution of urea in water. Then, a Petri dish was filled with water or 300 mM urea solution in water and positioned in the centre of the field of view of the PET scanner. A 10 µL drop of ^{18}F-urease nanomotors was added to the liquid-filled Petri dish, and dynamic PET images were acquired over 6 minutes (Figure 3.2).

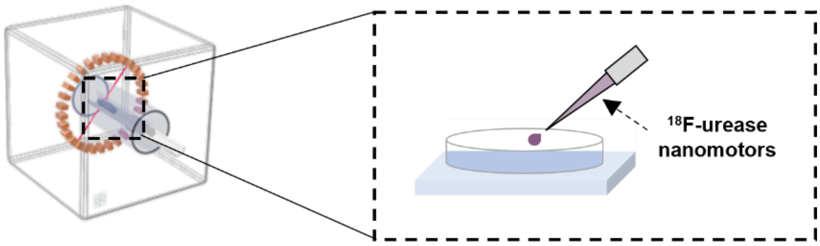

Figure 3.2. Schematic representation of the design performed during the *in vitro* PET study using a Petri dish.

PET images were reconstructed using 3D OSEM reconstruction algorithm and applying random, scatter and attenuation corrections, and analysed for pixel intensity distribution using PMOD image processing tool.

Phantoms

To analyse the effect of complex paths on the motility of passive nanoparticles and active nanomotor swarms, polydimethylsiloxane phantoms with different shapes were prepared (Figure 3.3a). To obtain the desired channels' geometry, a 3D design was prepared by using autoCAD software and posttreated with PreForm Software to be later 3D printed by stereolithography.

The central channels of all phantoms were filled either with 300 mM urea solution in water or ultrapure water (one channel with each medium) and positioned in the centre of the field of view of the PET scanner (Figure 3.3b). The field of view was selected to cover the whole length of the phantom. For each media, two samples of labelled urease nanomotors (10 µL, *ca*. 1 MBq each) were seeded simultaneously in one of the edges of the phantom, one in the channel filled with urea solution and the other one in the channel filled with ultrapure water. Immediately after, a dynamic PET scan was acquired for 25 minutes, followed by a CT acquisition.

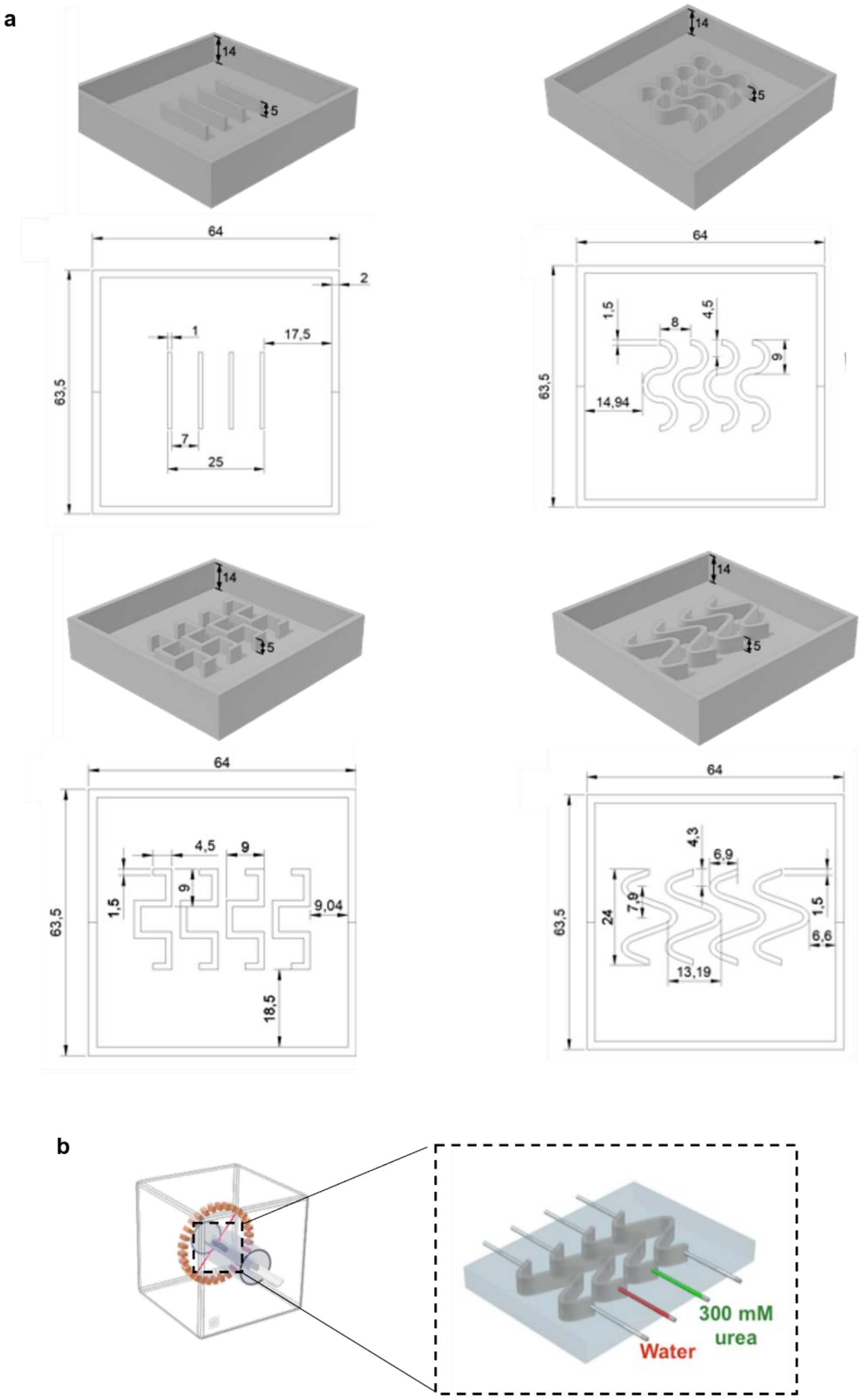

Figure 3.3. a) Design and dimensions of the molds for the different phantoms. b) schematic representation of the design performed during the in vitro PET study using the complex phantoms.

PET images were reconstructed using 3D OSEM reconstruction algorithm and applying random, scatter and attenuation corrections, and analysed using PMOD image processing tool. With that aim, the whole channel was divided in sectors with the same length over the coronal view, and the concentration of activity in each section was determined as a function of time. The values of activity concentration were finally normalized to the whole amount of radioactivity in the channel.

3.3.6 *In vivo* imaging studies

3.3.6.1 General considerations

Female mice (C57BL/6JRj, 8 week-old, Janvier lab; 12 animals, see below for number of animals under different experimental scenarios) weighing 20 ± 3 g were used to conduct the biodistribution studies. The animals were maintained and handled in accordance with the Guidelines for Accommodation and Care of Animals (European Convention for the Protection of Vertebrate Animals Used for Experimental and Other Scientific Purposes) and internal guidelines. All experimental procedures were approved by the ethical committee and the local authorities before conducting experimental work (Code: PRO-AE-SS-059).

3.3.6.2 Intravenous administration

Anaesthesia was induced by inhalation of 3% isoflurane in pure O_2 and maintained by 1.5-2% isoflurane in 100% O_2. With the animal under anaesthesia, the ^{18}F-urease nanomotors or ^{124}I-urease nanomotors were injected via one of the lateral tail veins using PBS (10 mM, pH 7.4) as the vehicle (*N* = 2 for each type of radiolabelling; see Table 3.1 for details). Dynamic, whole body 60-min PET imaging sessions were immediately started after administration of the labelled compounds using a MOLECUBES β-CUBE scanner. After the PET scan, whole-body high resolution CT acquisitions were performed on the MOLECUBES X-CUBE scanner to provide anatomical information of each animal as well as the attenuation map for the later reconstruction of the PET images.

PET images were reconstructed using 3D OSEM reconstruction algorithm and applying random, scatter and attenuation corrections. PET-CT images of the same mouse were co-registered and analysed using PMOD image processing tool. Volumes of interest (VOIs) were placed on selected organs (namely: brain, thyroid, lungs, liver, stomach, kidneys, spleen, and bladder), as well as the heart in order to get an estimation of the concentration of radioactivity in blood. Time–activity curves (decay corrected) were obtained as cps/cm^3 in each organ. Curves were transformed into real activity (Bq/cm^3) curves by using a calibration factor, obtained from previous scans performed on a phantom (micro-deluxe, Data spectrum Corp.) under the same experimental conditions (isotope, reconstruction algorithm and energetic window).

3.3.6.3 Intravesical administration

Anaesthesia was induced by inhalation of 3% isoflurane in pure O_2 and maintained by 1.5-2% isoflurane in 100% O_2. With the animal under anaesthesia, the animals were positioned in supine position and the bladder was emptied by massaging the abdominal region. Immediately after, the ^{18}F-urease and ^{18}F-BSA nanomotors were introduced in the bladder (through a catheter) by intravesical administration using 300 mM of urea solution in water or ultrapure water as the vehicle (*N* = 2 for each type of radiolabelling and vehicle; see Table 3.1 for details). Administration was followed by 45-minutes PET imaging sessions and whole-body high resolution CT acquisitions as above.

PET images were reconstructed using 3D OSEM reconstruction algorithm and applying random, scatter and attenuation corrections. PET-CT images of the same mouse were co-registered and analysed using PMOD image processing tool. Two VOIs were placed on the upper and lower regions of the bladder (namely: VOI 1 and VOI 2) to obtain the concentration of radioactivity in both VOIs over time. The values were normalized to the maximum values for each frame.

Table 3.1. Summary of the *in vivo* studies performed with the different types of nanomotors and administration routes.

Group	**Number of animals**	**Particle**	**Administration route**	**Vehicle**	**Activity (MBq)**	**Mass of Particles (µg)**
1	2	^{18}F-urease nanomotors	i.v.*	PBS	2.2 ± 0.10	73
2	2	^{124}I-urease nanomotors	i.v.*	PBS	1.6 ± 0.10	73
3	2	^{18}F-urease nanomotors	i.v.*	water	1.6 ± 0.10	33
4	2	^{18}F-urease nanomotors	i.vesic.*	urea	1.9 ± 0.15	33
5	2	^{18}F-BSA nanomotors	i.vesic.*	water	0.5 ± 0.06	33
6	2	^{18}F-BSA nanomotors	i.v.*	urea	0.4 ± 0.05	33

i.v.: intravenous; i.vesic.*: intravesical*

3.4 Results and discussion

3.4.1 Radiolabelling of nanomotors

This PhD thesis has been carried out in the Radiochemistry and Nuclear Imaging group at CIC biomaGUNE. For this reason, all the information stated below will be focused on the results obtained with the radiolabelling of nanomotors and *in vitro* and *in vivo* studies using PET-CT. The nanomotors preparation and characterization, together with the swarming behaviour of urease-powered nanomotors at microscopic level were conducted by the Smart nano-bio-devices group led by Prof. Samuel Sánchez at IBEC institute (Barcelona, Spain) and transferred to CIC biomaGUNE. As these studies were not performed by our group, the results will not be discussed here. The composition of the nanomotors will only be briefly discussed. For further details, the reader is referred to Hortelao, A.C, et al.[26]

The composition of these nanomotors is based on MSNPs, modified with amine groups by attaching APTES. The amino groups were activated with GA to enable the covalent binding of the enzyme (urease or BSA) and the heterobifunctional polyethylene glycol (NH_2-PEG-SH). The available thiol groups were used to anchor gold nanoparticles (AuNPs) to the surface of the nanomotors (Figure 3.4a). Dynamic light scattering (DLS) and electrophoretic mobility analysis were performed to assess the hydrodynamic radii and stability, and surface properties, respectively. The resulting particles had an average diameter of 507.8 ± 3.4 nm with a homogenous distribution of AuNPs on the surface (as determined by TEM), and a Z-potential of −32.0 ± 0.6 mV (Figure 3.4b).

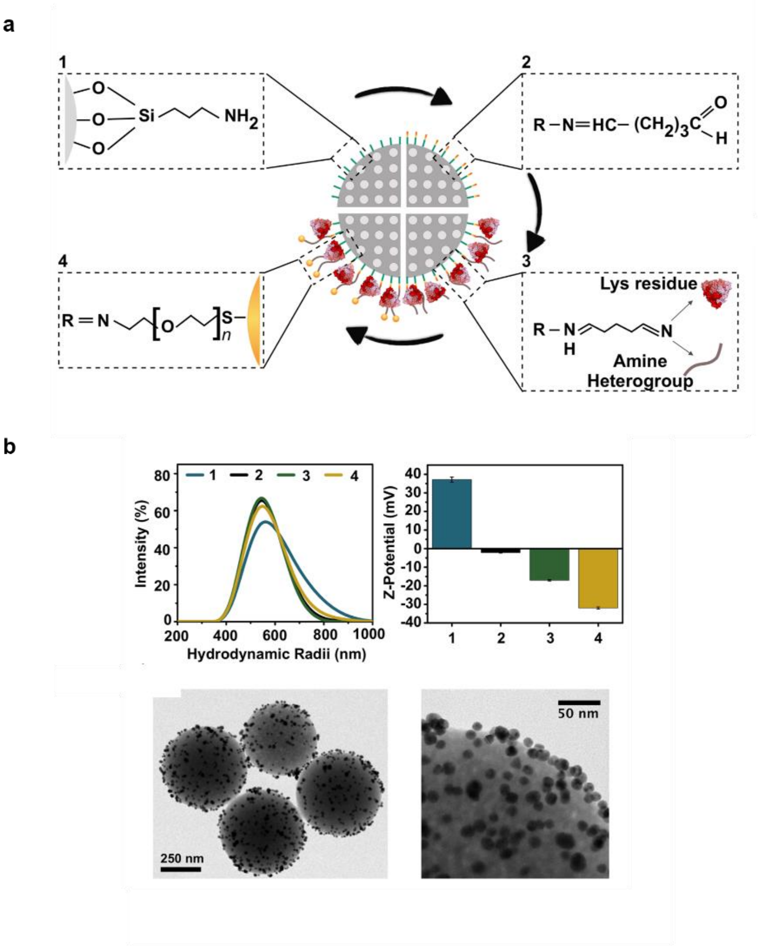

Figure 3.4. Fabrication steps (a) and characterization by DLS, Z-potential, and TEM (b) of urease-powered nanomotors.

For enabling the visualization of the nanomotors by PET, our approach was the use of two positron emitters, namely ^{18}F and ^{124}I. The decision of using these radioisotopes was based on the previous experience of our group. Prior studies were performed using a prosthetic group pre-labelled with ^{18}F for enabling the radiolabelling of macromolecules or NPs, containing amino groups[27]. Furthermore, ^{124}I has been used to radiolabel AuNPs via chemisorption[20, 28]. Therefore, these two well-stablished methodologies were adequate to be applied in our nanomotors due to the presence of enzymes (containing lysine groups) and AuNPs on their surface.

The radioiodination was performed *via* direct absorption of ^{124}I on AuNPs present at the surface of the nanomotors (Figure 3.5a). This methodology has been previously described in the literature and applied to the radiolabelling of Au/PEDOT/Pt micromotors[20]. In our case, urease ^{124}I-nanomotors were prepared following the same procedure with minor modifications. [^{124}I]NaI was incubated with the nanomotors at room temperature during 30 min, followed by a purification step by centrifugation. Radiochemical purity of urease ^{124}I-nanomotors after purification was ≥99%, as determined by radio-TLC (Figure 3.5b). The radiochemical yield obtained was 71 ± 2%, due to the high-affinity binding between gold and iodine.

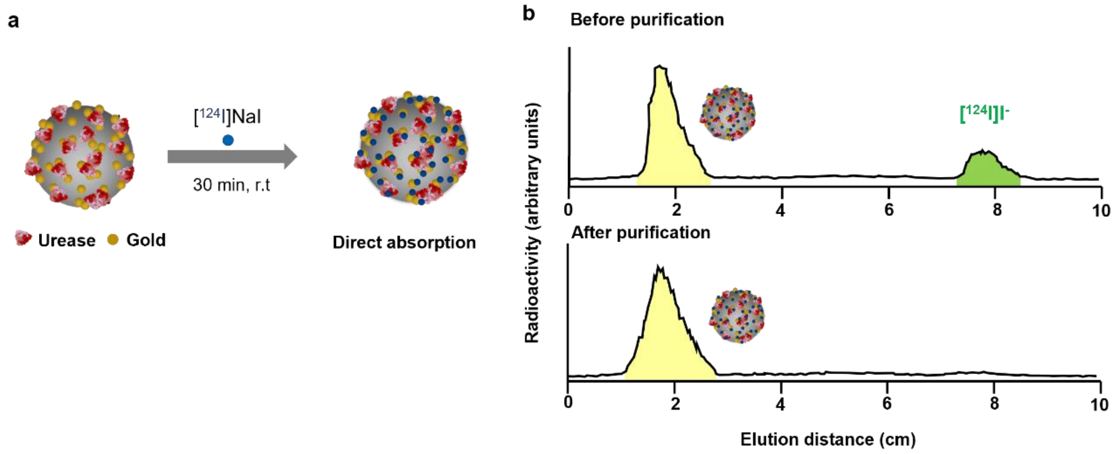

Figure 3.5. a) Radiolabelling of nanomotors by direct absorption on the AuNP of ^{124}I to yield urease ^{124}I-nanomotors. b) Labelling efficiency and radiochemical purity monitored by radio-TLC.

Working with ^{124}I has some drawbacks despite its radiolabelling efficiency: (I) our cyclotron cannot produce ^{124}I, consequently the organization of the studies is challenging. ^{124}I can be provided from commercial supplies, but it is expensive and also requires synchronization between experiments in animals and the delivery schedules of the provider. (II) The emission spectrum of ^{124}I is considered not optimal for PET imaging[29] (Figure 3.6). The decay mode of ^{124}I is mainly by electron capture, where only 23% of disintegrations lead to positrons (β^+), resulting in the emission of high-energy gamma (γ) rays. Furthermore, the resulting β^+ have a high energy (2140 KeV), which is translated in images with lower resolution compared to those obtained with other positron emitters.

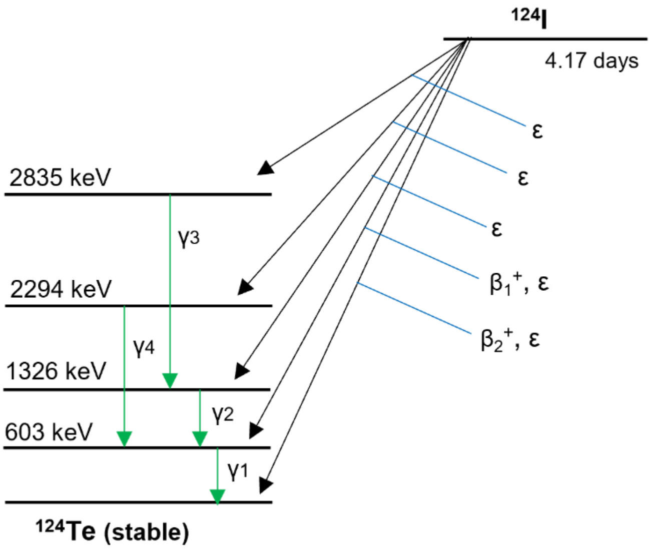

Figure 3.6. Simplified decay scheme of ^{124}I radionuclide. Adapted from Kuker, R.[29]

To overcome the problems associated to ^{124}I, we developed an unprecedented methodology to label nanomotors using the positron emitter ^{18}F. Our strategy consisted on the radiolabelling of the urease attached to the nanomotor's surface with a pre-labelled prosthetic group [^{18}F]F-PyTFP, taking advantage of the available amino groups on the enzyme (Figure 3.7a). [^{18}F]F-PyTFP is based on an active ester of nicotinic acid which can react efficiently with amino groups[25]. A single radiosynthesis step was required to achieve [^{18}F]F-PyTFP in good yields from its trimethylammonium precursor. The radiochemical synthesis consisted in the aromatic substitution of the trimethylammonium precursor with [^{18}F]F$^-$ at 40°C for 15 min to afford [^{18}F]F-PyTFP (Scheme 3.1). Then, the prosthetic group was purified by solid phase extraction prior to be incubated with the nanomotors.

The ^{18}F-urease nanomotors were produced by incubation of [^{18}F]F-PyTFP with nanomotors and the reaction mixture was monitored at different times (5, 25 and 35 min) using radio-TLC (Figure 3.7b). After diverse tests, the ideal time to get ^{18}F-urease nanomotors was set at 35 min, followed by a purification step by centrifugation. Radiochemical purity of ^{18}F-urease nanomotors after purification via centrifugation was ≥99% as determined by radio-TLC. Radiochemical yield obtained was 30% related to [^{18}F]F-PyTFP (decay-corrected).

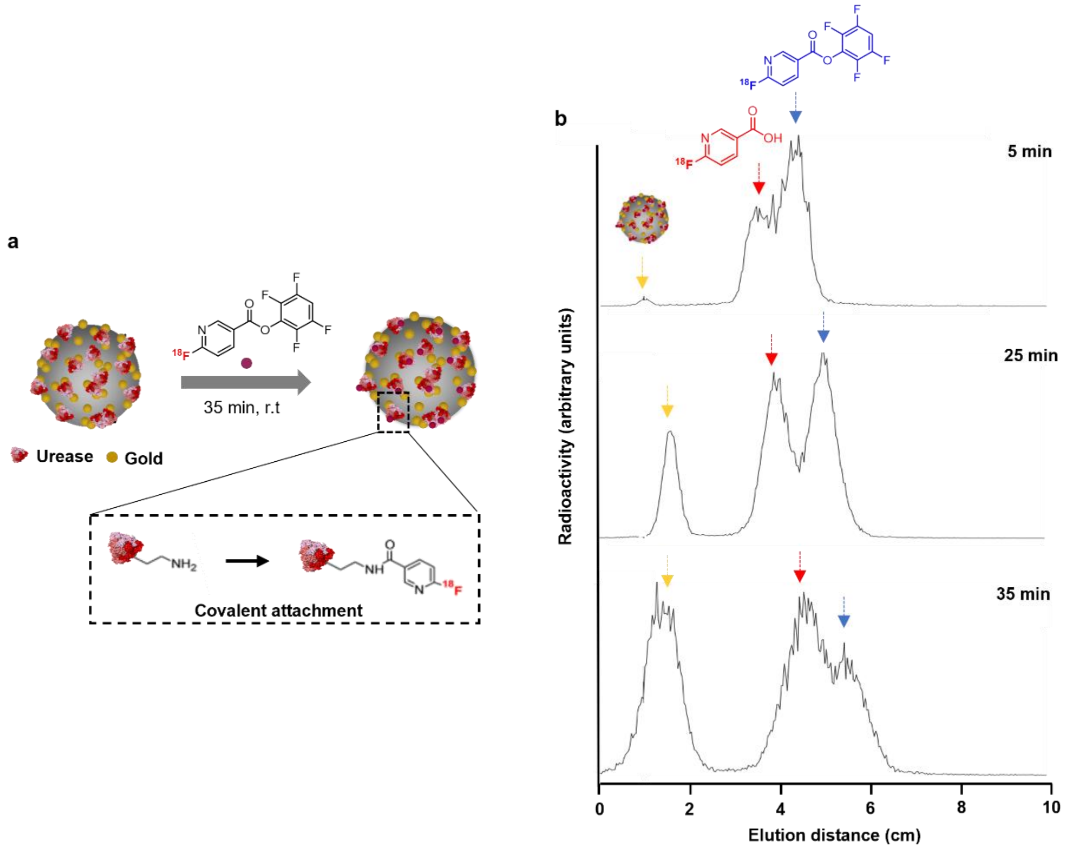

Figure 3.7. a) Radiolabelling of urease nanomotors by covalent attachment of [^{18}F]F-PyTFP to yield ^{18}F-urease nanomotors. b) Radiolabelling efficiency of ^{18}F-urease nanomotors at different times (5, 25 and 35 min) monitored by radio-TLC.

As control, ^{18}F-BSA nanomotors were prepared and labelled with ^{18}F following the same methodology. Briefly, BSA nanomotors were incubated with [^{18}F]F-PyTFP at room temperature for 35 min, followed by a purification step by centrifugation (Figure 3.8). Radiochemical yields and purity were similar to those obtained for ^{18}F-urease nanomotors.

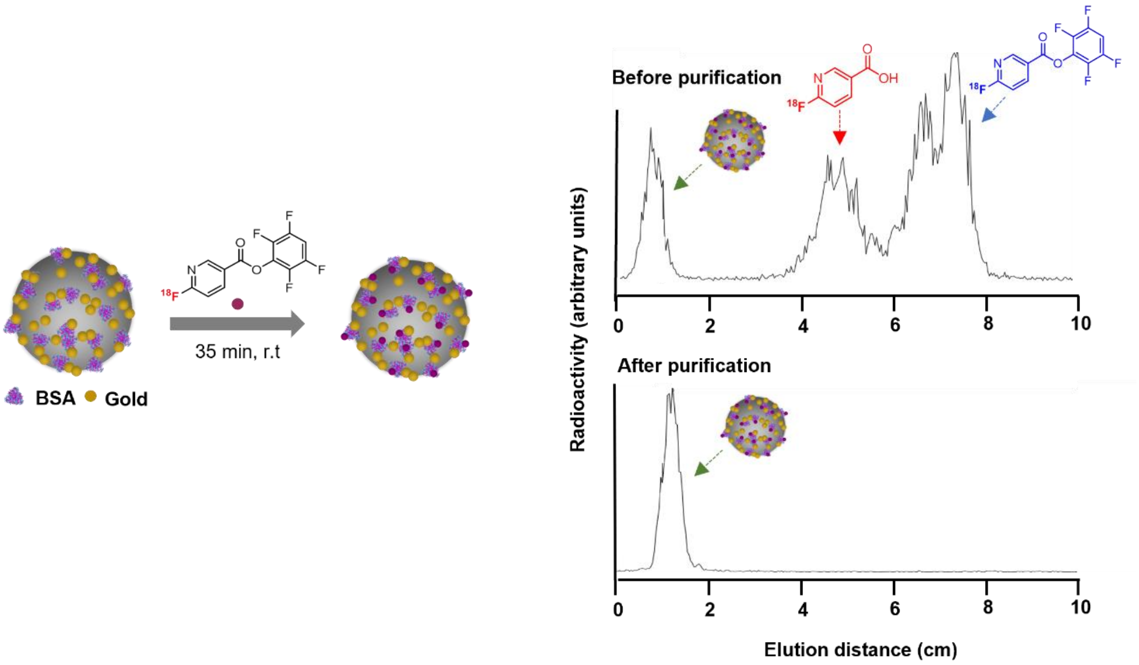

Figure 3.8. Radiolabelling of BSA nanomotors by covalent attachment of $[^{18}\text{F}]$F-PyTFP to yield ^{18}F-BSA nanomotors (right), and labelling efficiency and radiochemical purity monitored by radio-TLC (left).

3.4.2 *In vitro* imaging of nanomotors

As previously stated, the self-propulsion of urease-powered nanomotors is promoted by the generation of ionic species in the solution due to the catalytic decomposition of urea into carbon dioxide and ammonia[30, 31]. Nevertheless, most of the published studies are based on the study of a single-particle or a few particles by optical microscopy, and not about the collective swarming behaviour. Recently, it has been demonstrated that PET could be a useful technique to track nanomotors[20], and therefore a good tool for studying their collective movement.

Our first preliminary study was performed using only ^{18}F-urease nanomotors in a petri dish. For that, a 10-µL droplet of ^{18}F-urease nanomotors was placed onto a petri dish containing either pure water or 300 mM urea solution in water (maximum concentration found it in the bladder[32]), and PET scans were immediately started. The resulting PET images suggested that the ^{18}F-urease nanomotors remained close to the seeding point in water (Figure 3.9a), while in the presence of urea they distributed across the entire plate's length and width (Figure 3.9b). This behaviour was confirmed with three-dimensional (3D) histograms, which represents the pixel intensity distribution of the population of ^{18}F-urease nanomotors throughout the petri dish (Figure 3.9 c-d). Overall, this experiment demonstrated the suitability of PET imaging to obtain quantitative information about the nanomotors distribution *in vitro*.

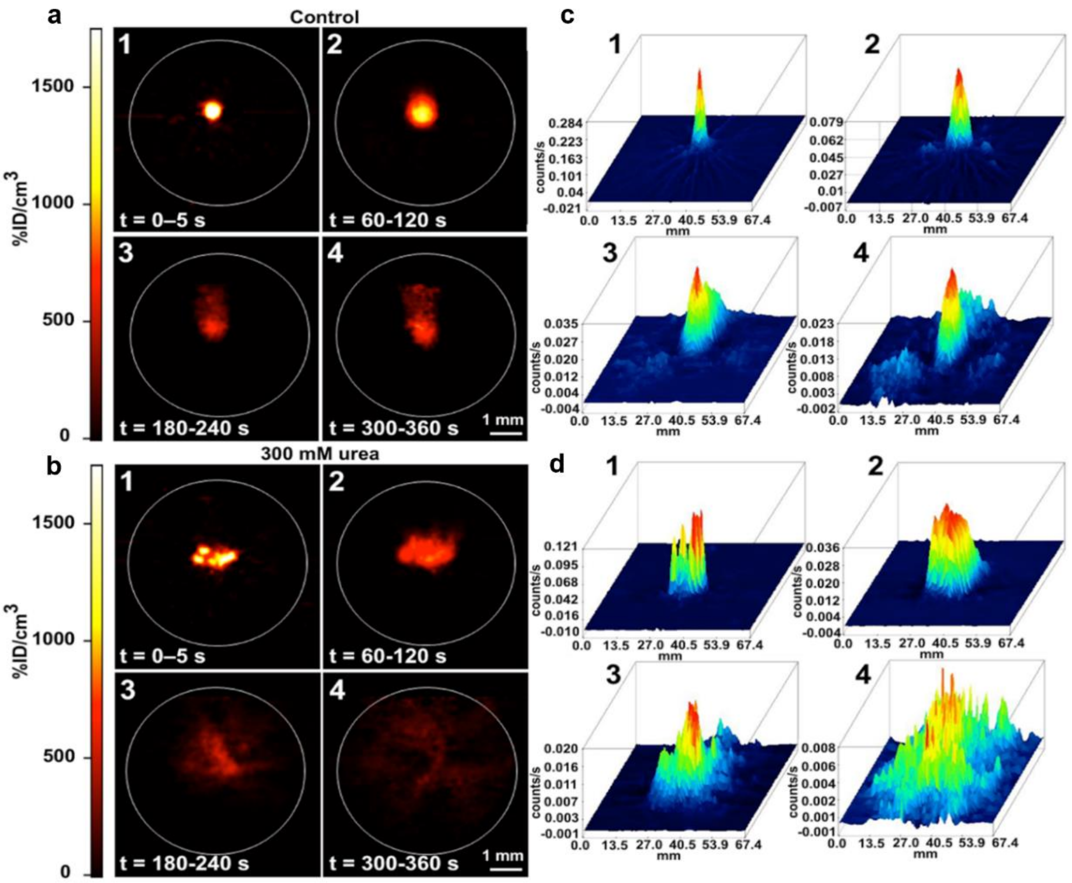

Figure 3.9. *In vitro* imaging of ^{18}F-urease nanomotor swarms in a Petri dish by PET imaging. Snapshots of a population of ^{18}F-urease nanomotors in a) water and b) 300 mM urea solution in water imaged by PET at 0-5 s (1), 60-120 s (2), 180-240 s (3), and 300-360 s (4). Pixel intensity distribution histograms of the population of ^{18}F-urease nanomotors in the field of view in c) water and d) 300 mM urea solution.

Subsequently, the *in vitro* swarming behaviour of the nanomotors was investigated in four different phantoms with increasing degrees of complexity; (i) straight, (ii) rectangular, (iii) curved, and (iv) curved path with longer straight channel. With that aim, phantoms were filled with water and 300 mM urea solution in water (one channel with each medium) and positioned in the middle of the field of view of PET camera (Figure 3.10, left). Two samples of ^{18}F-urease nanomotors (one in urea solution and the other with water) were seeded simultaneously at the edge of each channel, and dynamic PET images were immediately acquired over 25 min.

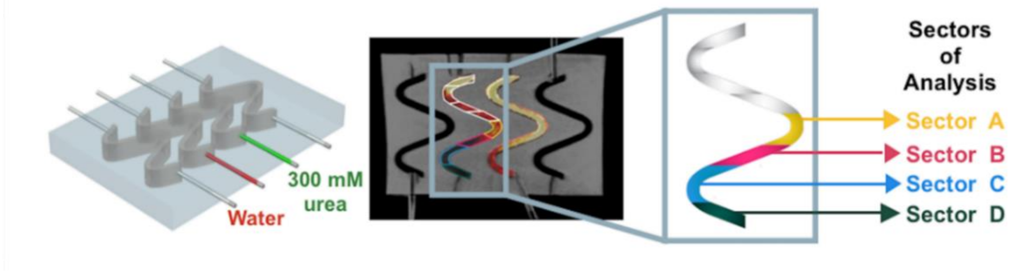

Figure 3.10. Scheme depicting the experimental set up (left) and the corresponding sectors of analysis of 3D phantoms performed on PET studies (right).

Visual inspection of the images obtained after seeding the ^{18}F-urease nanomotors clearly suggests a prominent effect on the motion of the nanomotors in the presence of urea solution (Figure 3.11 a-d for representative images). Irrespective of the shape of the phantom, nanomotors reached the end of the channel at the later time point (25 min) in the presence of urea solution, while most of nanomotors remained close to the seeding point in water, and only minimal movement could be observed. To get quantitative data, four sectors with the same length were defined in each phantom (marked in yellow, pink, blue, green in Figure 3.10, right), and the concentration of radioactivity was determined in each sector as a function of time. Values were normalised to the total amount of radioactivity in the channel.

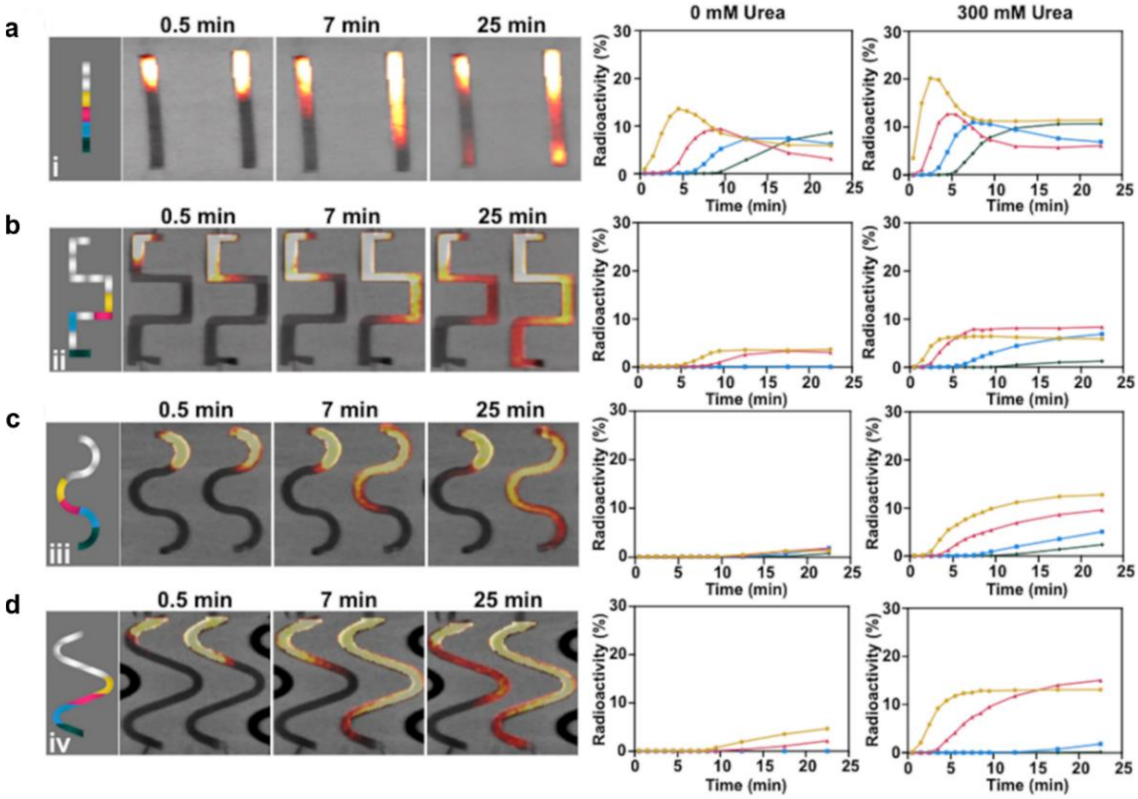

Figure 3.11. Left part of the figure: PET images (coronal projections) obtained at 0.5, 7 and 25 minutes after seeding of the ^{18}F-urease nanomotors in different-shaped phantoms a) straight (i), b) rectangular (ii), c) curved (iii), and d) a curved path with longer straight trenches (iv). For each phantom, one of the channels was filled with water (left) and another channel was filled with 300 mM urea solution in water (right). The channels were then divided in four sectors with the same length over the coronal view and the concentration of activity in each channel was measured as a function on time. The values were normalized to the total amount of radioactivity in each channel. Values of concentration of radioactivity as a function of time in each sector and for each channel and phantom are shown on the right part of the figure.

Focusing on the less restrictive phantom (straight shape, Figure 3.11a), nanomotors could be detected for both media in the sectors under consideration, although the movement is slower for non-activated nanomotors, as clearly visible in the dynamic curves of sectors A to D. These differences increased when the mobility is limited by introducing more complex phantoms (ii to iv). Figure 3.11 (b-d) shows that nanomotors can reach sectors B to D much faster in urea than in water, which was confirmed by the higher concentration of radioactivity in those sectors farther from the seeding point. Indeed, nanomotors in water stay close to the seeding point and slowly move along the channel, probably due to passive diffusion.

Equivalent results were obtained when the experiments were repeated with urease ^{124}I-nanomotors (Figure 3.12), confirming the robustness of our approach and the stability of the radiolabel under investigated conditions. Small differences could be observed using the two radionuclides; these might be due to inherent limitations of PET imaging. The diameter of the channel (*ca*. 1.5 mm) is very close to the spatial resolution of our PET system, which is around 1.0 mm full-width half maximum for ^{18}F, and notably lower for ^{124}I with less favourable emission properties[33]. Moreover, some error in the absolute quantification values could be promoted by the partial volume effect due to the presence of a high concentration of radioactivity in a small volume.

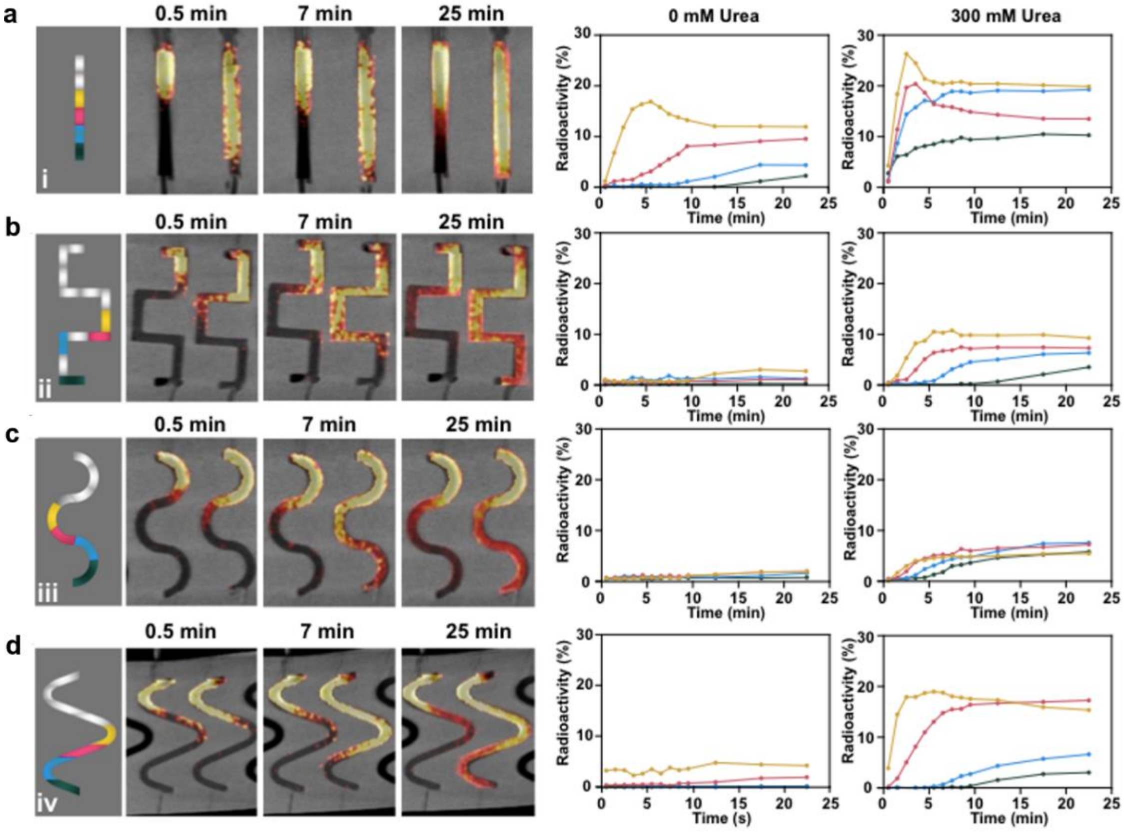

Figure 3.12. PET images (coronal projections) obtained at 0.5, 7 and 25 minutes after seeding of the urease ^{124}I-nanomotors in different-shaped phantoms a) straight (i), b) rectangular (ii), c) curved (iii), and d) a curved path with longer straight trenches (iv) on the left. For each phantom, one of the channels was filled with water (left) and another channel was filled with 300 mM urea solution in water (right). For image quantification, the channels were divided in four sectors with the same length over the coronal view and the concentration of activity in each channel was measured as a function on time. The values were normalized to the total amount of radioactivity in each channel. Values of concentration of radioactivity as a function of time in each sector and for each channel and phantom are shown on the right part of the figure.

The results obtained by PET imaging confirmed the enhanced mobility of urease-powered nanomotors in the presence of urea, effect that becomes more notable when the complexity of the path increase. Furthermore, the results highlight the usefulness of PET technique for absolute quantification and tracking of nanomotors.

3.4.3 *In vivo* imaging of nanomotors

3.4.3.1 Biodistribution of intravenously administered nanomotors

Moving towards biomedical applications, we next explored the biodistribution of ^{18}F-urease nanomotors and ^{124}I-urease-nanomotors in female mice after intravenous administration. This study was carried out to (I) demonstrate the suitability of *in vivo* PET imaging to quantitatively track nanomotors at the whole-body level, and (II) evaluate the *in vivo* stability of the radiolabel.

PET images obtained after intravenous administration of ^{18}F-urease nanomotors (Figure 3.13a) show an initial accumulation of radioactivity in the lungs and the liver, and a progressive accumulation of the radioactivity in the bladder suggesting slow elimination via urine, as confirmed by image quantification (Figure 3.13 b-c). Higher accumulation in the liver was observed at short times after administration, until stable uptake values (*ca*. 25% injected dose per organ; %ID/organ) were reached and maintained over the whole duration of the study. These results, together with accumulation in the lungs, correspond to a typical biodistribution profile observed for nanoparticles with similar size after intravenous administration, suggesting a rapid uptake by the mononuclear phagocyte system (MPS). At long times after administration ($t > 15$ min), the amount of radioactivity progressively increased in the bladder. Because the nanomotors are above the estimated size threshold for glomerular filtration (*ca*. 8 nm)[34], the presence of radioactivity in urine is an indicator of slow detachment of the radiolabel from the nanomotors.

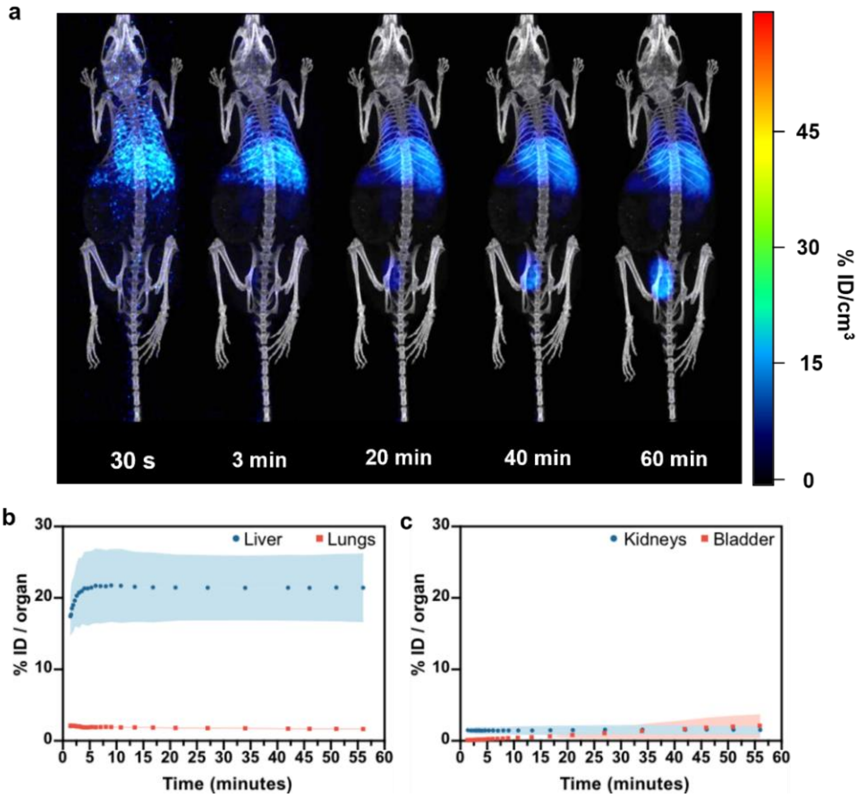

Figure 3.13. Biodistribution of ^{18}F-urease nanomotors after intravenous administration. a) PET-CT coronal images (maximum intensity projections) obtained at different time points. Time-activity curves of ^{18}F-urease nanomotors in the liver and lungs (b) and kidneys and bladder (c), as determined by PET imaging. Results are expressed as percentage of injected dose per organ (mean ± SD, *N* = 2).

Interestingly, ^{124}I-urease-nanomotors show a completely different biodistribution profile (Figure 3.14). Initial accumulation is observed at short times in the liver and the lungs, similarly to ^{18}F-urease nanomotors (Figure 3.14b). Nevertheless, the concentration of radioactivity in both organs progressively decreases afterwards, paralleled by an increase in the thyroid gland, stomach, and urine (Figure 3.14 c-d). The thyroid gland, the stomach and the bladder are the metabolic sites of free iodine[35], and hence, our results suggest a fast nanomotor deiodination, probably by desorption of ^{124}I from the gold surface.

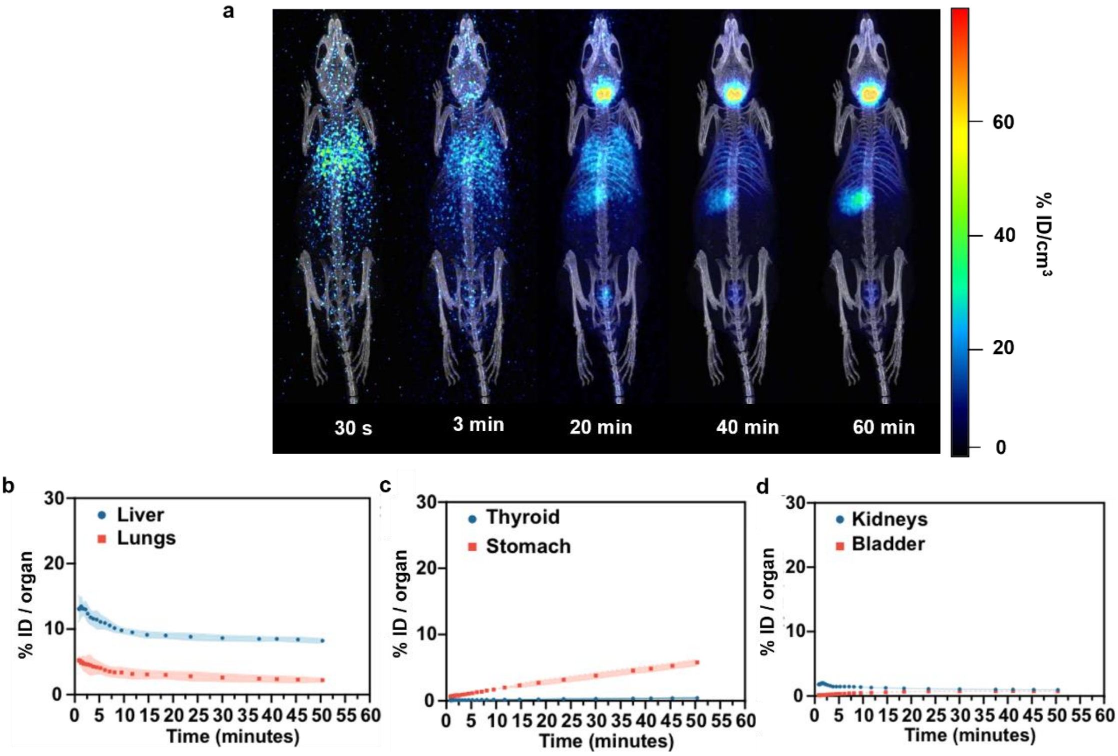

Figure 3.14. Biodistribution of urease ^{124}I-nanomotors injected intravenously. a) PET-CT coronal images (maximum intensity projections) obtained at different time points. Time-activity curves of urease ^{124}I-nanomotors in b) liver and lungs and c) thyroid and stomach, and d) kidneys and bladder, as determined by PET imaging. Results are expressed as percentage of injected dose per organ (mean ± SD, *N* = 2).

Together, these results demonstrate that positron emitter-labelled nanomotors can be tracked *in vivo* after administration into living organisms using PET imaging, and that radiolabelling with ^{18}F is a more convenient strategy since higher radiochemical stability was observed compared to ^{124}I-radiolabelling.

3.4.3.2 Biodistribution of intravesically administered nanomotors

As our nanomotors have the capacity to self-propel in the presence of urea, applications in bladder cancer imaging and therapy could be foreseen. As nanomotors' size prevents accumulation in the bladder after intravenous injection, and conventional treatments in bladder cancer are applied by intravesical instillation[36], we decided to study the motile properties of urease-powered nanomotors after intravesical administration using PET imaging. Considering the previous results obtained, only ^{18}F-urease nanomotors were used due to several reasons: (I) the radionuclide ^{18}F has better physical properties, with a 100% positron decay mode and lower energy of the emitted positrons, resulting in higher resolution images; (II) the production of ^{18}F is much easier and less costly than the production of ^{124}I, facilitating clinical translation; and (III) *in vivo* studies after intravenous administration confirmed higher stability of ^{18}F-urease nanomotors.

For this study, female mice with an empty bladder (emptied immediately before starting the experiments by promoting urination via abdominal massage) were positioned within the PET camera (supine position), and acquisitions were started immediately after intravesical instillation of ^{18}F-urease nanomotors either in water or 300 mM of urea solution in water. Visual inspection of the images obtained at different times after administration showed unprecedented results. When ^{18}F-urease nanomotors were injected using 300 mM urea solution in water as the vehicle, uniform distribution of the radioactivity was observed immediately after instillation, followed by a progressive radioactivity displacement resulting in two-phase formation. At longer times, a progressive cancelation between the two phases was observed, leading to a uniform distribution of radioactivity within the bladder at t = 45 min (Figure 3.15 (1)). Contrarily, the distribution after instillation of ^{18}F-urease nanomotors in water as vehicle followed a different trend. The two-phase formation was maintained during the whole imaging study (Figure 3.15 (2)). These qualitative results were confirmed by analysis of the concentration of radioactivity in two volumes of interest (VOIs) drawn within the two phases observed (VOI 1: blue, and VOI 2: red) to obtain time-activity curves normalised to total amount of radioactivity.

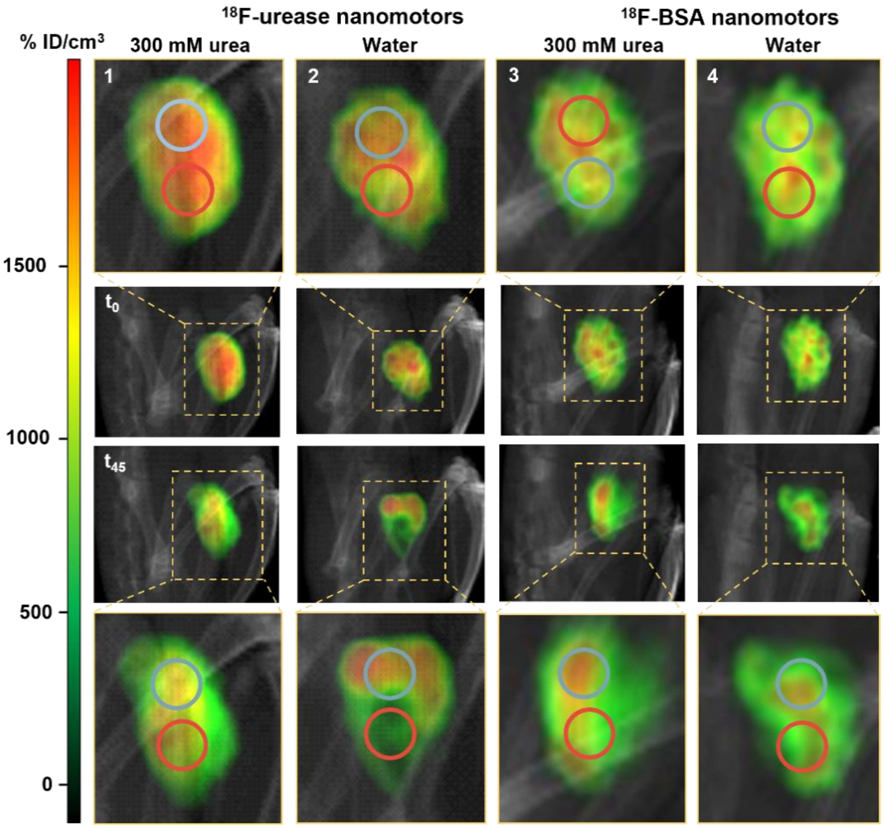

Figure 3.15. PET-CT images (maximum intensity projections) obtained at different time points after the intravesical instillation of ^{18}F-urease nanomotors in urea (1) and water (2), and control ^{18}F-BSA nanomotors in urea (3) and water (4).

For ^{18}F-urease nanomotors injected in urea, the initial time-activity profile shows that the amount of radioactivity in both regions was close to 50% (homogenous distribution). After some minutes, the value of VOI 1 progressively increases to reach a maximum of *ca.* 70% (two-phase formation), and then decreases to recover starting values until the end of the study (homogenous distribution, Figure 3.16 (1)). The concentration of radioactivity in VOI 2 follows an opposite trend, with an initial decrease and progressive increase afterwards. In contrast, time activity-curves obtained for ^{18}F-urease nanomotors instilled in water (control conditions) show a divergent trend (Figure 3.16 (2)). Initial uniform distribution of the radioactivity at short times after administration in both VOIs (*ca.* 50%), corresponding to homogenous distribution within the bladder. Nevertheless, the amount of radioactivity in VOI 1 tends to increase with time, while the concentration of radioactivity in VOI 2 has an opposite trend, until the end of the study (non -homogenous distribution).

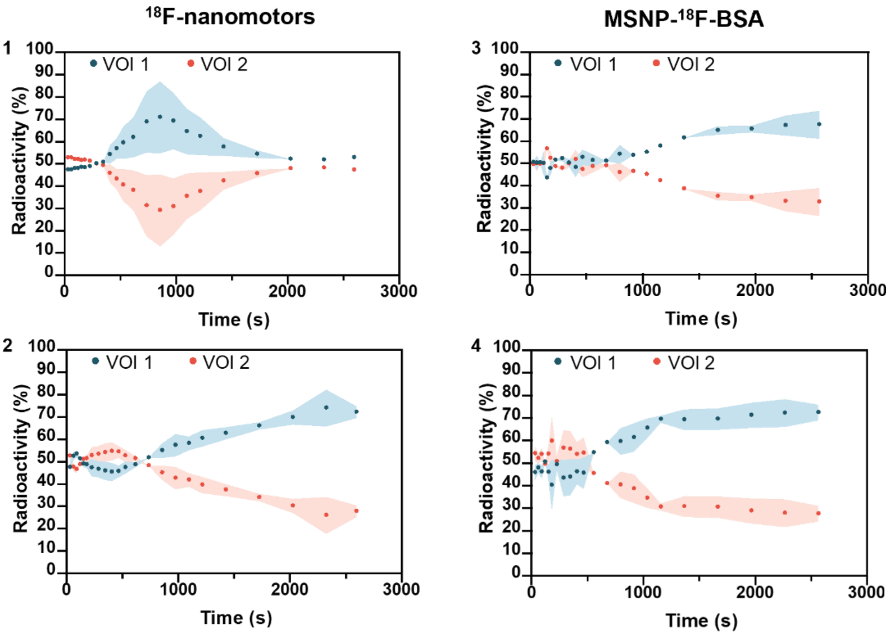

Figure 3.16. Quantification analysis of the PET-CT images obtained after intravesical instillation of ^{18}F-urease nanomotors in urea (1) and water (2), and control ^{18}F-BSA nanomotors in urea (3) and water (4).

These results suggests that immediately after ^{18}F-urease nanomotors instillation into the empty bladder, fresh urine starts entering. This new urine (non-radioactive) displaces the solution containing ^{18}F-urease nanomotors, creating two-phases (Figure 3.17). If ^{18}F-urease nanomotors are in urea, they can actively move and enhance mixing effect, reversing the phase separation. However, when ^{18}F-urease nanomotors are instilled in water, the separation of two phases remains until the end of the study because nanomotors are not in close contact with the urea (present only in the fresh urine), and consequently, they do not have motile properties.

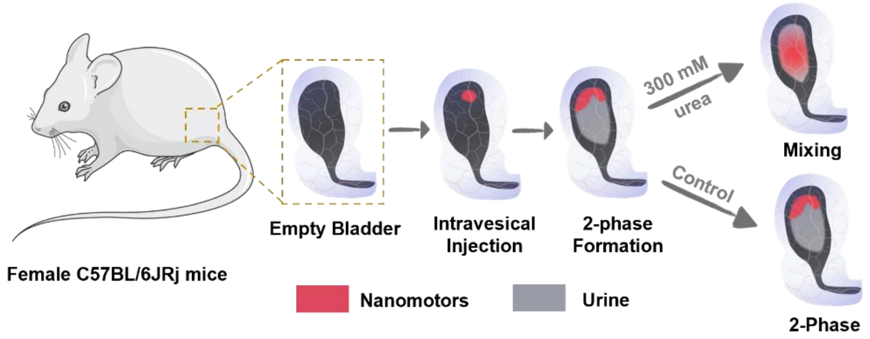

Figure 3.17. Schematic representation of the phenomena observed after intravesical instillation of ^{18}F-nanomotors.

To confirm these results, extra controls studies were performed using ^{18}F-BSA nanomotors, which do not show self-propelling capacity in urea or water. The experimental procedure was the same as for ^{18}F-urease nanomotors. The time-activity curves followed the same trend as for ^{18}F-urease nanomotors instilled in water (Figure 3.15 and 3.16 (3,4)) confirming the lack of particle mobility which results in a non-homogenous distribution of radioactivity within the bladder.

To our opinion, this is a clear proof of the capacity of the nanomotors to swim *in vivo* in the presence of the fuel. Moreover, this observed phenomenon could be a potential advantage in the design of active drug delivery systems because homogenous distribution of the drug is required to reach the target site.

3.5 Summary and conclusions

The work presented in this chapter shows two possible radiolabelling strategies for nanomotors, using ^{124}I by direct absorption on AuNPs and ^{18}F by labelling the enzyme with the pre-labelled prosthetic group [^{18}F]-FPyTFP. Then, we studied the *in vitro* collective movement of urease-labelled nanomotors in Petri dish and 3D phantoms. *In vivo* biodistribution and stability was observed after intravenous administration of both ^{18}F-urease nanomotors and urease ^{124}I-nanomotors. Finally, the *in vivo* movement of ^{18}F-urease-powered nanomotors was studied after intravesical administration.

Overall, the results obtained in this chapter demonstrate the suitability of using nuclear imaging techniques, particularly PET in combination with CT, to investigate the collective behaviour of nanomotors both *in vitro* and *in vivo*. Moreover, the mixing effect observed upon intravesical instillation of urease-powered nanomotors in urea hold great potential towards biomedical applications, particularly in bladder cancer, where a homogenous distribution is required for targeting and drug delivery purposes.

3.6 References

(1) Farokhzad, O. C.; Langer, R., Impact of Nanotechnology on Drug Delivery. *ACS Nano* **2009,** *3* (1), 16-20.

(2) Wang, A. Z.; Langer, R.; Farokhzad, O. C., Nanoparticle Delivery of Cancer Drugs. *Annual Review of Medicine* **2012,** *63* (1), 185-198.

(3) Blanco, E.; Shen, H.; Ferrari, M., Principles of nanoparticle design for overcoming biological barriers to drug delivery. *Nat Biotechnol* **2015,** *33* (9), 941-51.

(4) Kou, L.; Bhutia, Y. D.; Yao, Q.; He, Z.; Sun, J.; Ganapathy, V., Transporter-Guided Delivery of Nanoparticles to Improve Drug Permeation across Cellular Barriers and Drug Exposure to Selective Cell Types. *Frontiers in Pharmacology* **2018,** *9*, 27.

(5) Wilhelm, S.; Tavares, A. J.; Dai, Q.; Ohta, S.; Audet, J.; Dvorak, H. F.; Chan, W. C. W., Analysis of nanoparticle delivery to tumours. *Nature Reviews Materials* **2016,** *1* (5), 16014.

(6) Paxton, W. F.; Kistler, K. C.; Olmeda, C. C.; Sen, A.; St Angelo, S. K.; Cao, Y.; Mallouk, T. E.; Lammert, P. E.; Crespi, V. H., Catalytic nanomotors: autonomous movement of striped nanorods. *J Am Chem Soc* **2004,** *126* (41), 13424-31.

(7) Douglas, S. M.; Bachelet, I.; Church, G. M., A Logic-Gated Nanorobot for Targeted Transport of Molecular Payloads. **2012,** *335* (6070), 831-834.

(8) Hortelao, A. C.; Carrascosa, R.; Murillo-Cremaes, N.; Patino, T.; Sanchez, S., Targeting 3D Bladder Cancer Spheroids with Urease-Powered Nanomotors. *ACS Nano* **2019,** *13* (1), 429-439.

(9) Hortelão, A. C.; Patiño, T.; Perez-Jiménez, A.; Blanco, À.; Sánchez, S., Enzyme-Powered Nanobots Enhance Anticancer Drug Delivery. *Advanced Functional Materials* **2018,** *28* (25), 1705086.

(10) Tang, S.; Zhang, F.; Gong, H.; Wei, F.; Zhuang, J.; Karshalev, E.; Ávila, B. E.-F. d.; Huang, C.; Zhou, Z.; Li, Z.; Yin, L.; Dong, H.; Fang, R. H.; Zhang, X.; Zhang, L.; Wang, J., Enzyme-powered Janus platelet cell robots for active and targeted drug delivery. **2020,** *5* (43), eaba6137.

(11) Ma, X.; Jannasch, A.; Albrecht, U. R.; Hahn, K.; Miguel-Lopez, A.; Schaffer, E.; Sanchez, S., Enzyme-Powered Hollow Mesoporous Janus Nanomotors. *Nano Lett* **2015,** *15* (10), 7043-50.

(12) Ma, X.; Hortelao, A. C.; Patino, T.; Sanchez, S., Enzyme Catalysis To Power Micro/Nanomachines. *ACS Nano* **2016,** *10* (10), 9111-9122.

(13) Yan, X.; Zhou, Q.; Vincent, M.; Deng, Y.; Yu, J.; Xu, J.; Xu, T.; Tang, T.; Bian, L.; Wang, Y.-X. J.; Kostarelos, K.; Zhang, L., Multifunctional biohybrid magnetite microrobots for imaging-guided therapy. **2017,** *2* (12), eaaq1155.

(14) Zheng, S.; Wang, Y.; Pan, S.; Ma, E.; Jin, S.; Jiao, M.; Wang, W.; Li, J.; Xu, K.; Wang, H., Biocompatible Nanomotors as Active Diagnostic Imaging Agents for Enhanced Magnetic Resonance Imaging of Tumor Tissues In Vivo. *Advanced Functional Materials* **2021,** *31* (24), 2100936.

(15) Choi, H.; Cho, S. H.; Hahn, S. K., Urease-Powered Polydopamine Nanomotors for Intravesical Therapy of Bladder Diseases. *ACS Nano* **2020,** *14* (6), 6683-6692.

(16) Servant, A.; Qiu, F.; Mazza, M.; Kostarelos, K.; Nelson, B. J., Controlled in vivo swimming of a swarm of bacteria-like microrobotic flagella. *Adv Mater* **2015,** *27* (19), 2981-8.

(17) Wu, Z.; Li, L.; Yang, Y.; Hu, P.; Li, Y.; Yang, S.-Y.; Wang, L. V.; Gao, W., A microrobotic system guided by photoacoustic computed tomography for targeted navigation in intestines in vivo. **2019,** *4* (32), eaax0613.

(18) Olson, E. S.; Orozco, J.; Wu, Z.; Malone, C. D.; Yi, B.; Gao, W.; Eghtedari, M.; Wang, J.; Mattrey, R. F., Toward in vivo detection of hydrogen peroxide with ultrasound molecular imaging. *Biomaterials* **2013,** *34* (35), 8918-8924.

(19) St James, S.; Bednarz, B.; Benedict, S.; Buchsbaum, J. C.; Dewaraja, Y.; Frey, E.; Hobbs, R.; Grudzinski, J.; Roncali, E.; Sgouros, G.; Capala, J.; Xiao, Y., Current Status of Radiopharmaceutical Therapy. *Int J Radiat Oncol Biol Phys* **2021,** *109* (4), 891-901.

(20) Vilela, D.; Cossio, U.; Parmar, J.; Martinez-Villacorta, A. M.; Gomez-Vallejo, V.; Llop, J.; Sanchez, S., Medical Imaging for the Tracking of Micromotors. *ACS Nano* **2018,** *12* (2), 1220-1227.

(21) He, Q.; Cui, X.; Cui, F.; Guo, L.; Shi, J., Size-controlled synthesis of monodispersed mesoporous silica nano-spheres under a neutral condition. *Microporous and Mesoporous Materials* **2009,** *117* (3), 609-616.

(22) Wang, Y.; Sun, Y.; Wang, J.; Yang, Y.; Li, Y.; Yuan, Y.; Liu, C., Charge-Reversal APTES-Modified Mesoporous Silica Nanoparticles with High Drug Loading and Release Controllability. *ACS Applied Materials & Interfaces* **2016,** *8* (27), 17166-17175.

(23) Ai, K.; Liu, Y.; Lu, L., Hydrogen-Bonding Recognition-Induced Color Change of Gold Nanoparticles for Visual Detection of Melamine in Raw Milk and Infant Formula. *Journal of the American Chemical Society* **2009,** *131* (27), 9496-9497.

(24) Vilela, D.; Hortelao, A. C.; Balderas-Xicohténcatl, R.; Hirscher, M.; Hahn, K.; Ma, X.; Sánchez, S., Facile fabrication of mesoporous silica micro-jets with multi-functionalities. *Nanoscale* **2017,** *9* (37), 13990-13997.

(25) Olberg, D. E.; Arukwe, J. M.; Grace, D.; Hjelstuen, O. K.; Solbakken, M.; Kindberg, G. M.; Cuthbertson, A., One step radiosynthesis of 6-[(18)F]fluoronicotinic acid 2,3,5,6-tetrafluorophenyl ester ([(18)F]F-Py-TFP): a new prosthetic group for efficient labeling of biomolecules with fluorine-18. *J Med Chem* **2010,** *53* (4), 1732-40.

(26) Hortelao, A. C.; Simó, C.; Guix, M.; Guallar-Garrido, S.; Julián, E.; Vilela, D.; Rejc, L.; Ramos-Cabrer, P.; Cossío, U.; Gómez-Vallejo, V.; Patiño, T.; Llop, J.; Sánchez, S., Swarming behavior and in vivo monitoring of enzymatic nanomotors within the bladder. **2021,** *6* (52), eabd2823.

(27) Feiner, I. V. J.; Pulagam, K. R.; Uribe, K. B.; Passannante, R.; Simo, C.; Zamacola, K.; Gomez-Vallejo, V.; Herrero-Alvarez, N.; Cossio, U.; Baz, Z.; Caffarel, M. M.; Lawrie, C. H.; Vugts, D. J.; Rejc, L.; Llop, J., Pre-targeting with ultra-small nanoparticles: boron carbon dots as drug candidates for boron neutron capture therapy. *J Mater Chem B* **2021,** *9* (2), 410-420.

(28) Pulagam, K. R.; Gona, K. B.; Gomez-Vallejo, V.; Meijer, J.; Zilberfain, C.; Estrela-Lopis, I.; Baz, Z.; Cossio, U.; Llop, J., Gold Nanoparticles as Boron Carriers for Boron Neutron Capture Therapy: Synthesis, Radiolabelling and In vivo Evaluation. *Molecules* **2019,** *24* (19), 3609.

(29) Kuker, R.; Sztejnberg, M.; Gulec, S., I-124 Imaging and Dosimetry. *Mol Imaging Radionucl Ther* **2017,** *26* (Suppl 1), 66-73.

(30) Arque, X.; Romero-Rivera, A.; Feixas, F.; Patino, T.; Osuna, S.; Sanchez, S., Intrinsic enzymatic properties modulate the self-propulsion of micromotors. *Nat Commun* **2019,** *10* (1), 2826.

(31) Patino, T.; Feiner-Gracia, N.; Arque, X.; Miguel-Lopez, A.; Jannasch, A.; Stumpp, T.; Schaffer, E.; Albertazzi, L.; Sanchez, S., Influence of Enzyme Quantity and Distribution on the Self-Propulsion of Non-Janus Urease-Powered Micromotors. *J Am Chem Soc* **2018,** *140* (25), 7896-7903.

(32) Liu, L.; Mo, H.; Wei, S.; Raftery, D., Quantitative analysis of urea in human urine and serum by 1H nuclear magnetic resonance. *Analyst* **2012,** *137* (3), 595-600.

(33) Jong, H. W. A. M. d.; Perk, L.; Visser, G. W. M.; Boellaard, R.; Dongen, G. A. M. S. v.; Lammertsma, A. A. In *High resolution PET imaging characteristics of /sup 68/Ga, /sup 124/I and /sup 89/Zr compared to /sup 18/F*, IEEE Nuclear Science Symposium Conference Record, 2005, 23-29 Oct. 2005; 2005; pp 1624-1627.

(34) Du, B.; Jiang, X.; Das, A.; Zhou, Q.; Yu, M.; Jin, R.; Zheng, J., Glomerular barrier behaves as an atomically precise bandpass filter in a sub-nanometre regime. *Nat Nanotechnol* **2017,** *12* (11), 1096-1102.

(35) Ahad, F.; Ganie, S. A., Iodine, Iodine metabolism and Iodine deficiency disorders revisited. *Indian J Endocrinol Metab* **2010,** *14* (1), 13-17.

(36) Richters, A.; Aben, K. K. H.; Kiemeney, L., The global burden of urinary bladder cancer: an update. *World J Urol* **2020,** *38* (8), 1895-1904.

CHAPTER 4

EVALUATION OF THE CAPACITY OF TUMOUR ACCUMULATION OF UREASE-POWERED NANOMOTORS

Chapter 4: Evaluation of the capacity of tumour accumulation of urease-powered nanomotors

4.1 Introduction

Despite recent advances, cancer is still one of the major causes of death worldwide[1, 2]. In particular, bladder cancer remains a major health concern with at least half a million of cases diagnosed globally each year[3], and a 5-year relative survival rate of 77 %[4]. Close to 75% of bladder cancer cases are classified as non-muscle invasive bladder cancer (NMIBC, Figure 4.1)[5], which are treated by transurethral resection of the bladder tumour, followed by intravesical instillation of immunotherapeutic (Mycobacterium bovis bacillus Calmette–Guérin, BCG[6]) and/or chemotherapeutic (mitomycin C, MMC[7]) agents. While the cases considered as muscle invasive bladder cancer (MIBC, Figure 4.1) are treated by partial or complete removal of the urinary bladder.

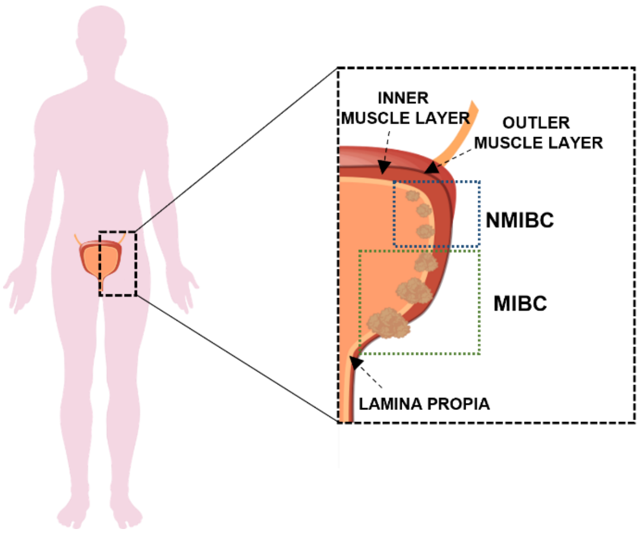

Figure 4.1. Schematic representation of bladder cancer classification. NMIBC: non-muscle-invasive bladder cancer; MIBC: muscle-invasive bladder cancer.

For NMIBC, local administration of the drug into the urinary bladder has shown an improvement in the exposure of the affected bladder to the therapeutic agent and a reduction of the dose required compared to systemic administration. However, the actual treatments can cause severe side effects and are not highly effective as recurrence appears in 30-70% of the patients within 5 years[8]. Therefore, frequent cystoscopic surveillance and re-treatment are required, turning bladder cancer in one of the most expensive malignancies to treat[9]. Limitations of the classical approach are related to the complexity of reaching the affected bladder tissue due to the lower permeability of the urothelium or the drug dilution because of the entrance of fresh urine[10]. The periodical voiding of urine washes out drug solutions instilled in the bladder; as a consequence, frequent catheterisations are required and the residence time of the drug is reduced, compromising the therapeutic efficacy[11].

The ideal drug for the treatment of bladder cancer should be able to accumulate efficiently in the tumour vicinity and penetrate the tumour mass to avoid leaving untreated subregions that may ultimately lead to recurrence. Therefore, new therapeutic strategies are needed to improve specificity, patient outcomes and minimize recurrence and progression rates.

In the last decade, the emergence of nanotechnology has led to the study of nano-sized systems as tools to increase therapeutic efficacy and minimize side effects in cancer treatment. In this sense, nanoparticles (NPs) can be loaded with drugs and surface-decorated with a large variety of functionalities to improve stability, circulation times, transport across membranes and accumulation at the target site[12, 13]. In the context of intravesical administration, different types of NPs have been reported to enhance the adhesion to the tumour, including polymeric NPs[14], liposomes[15], and carbon nanotubes[16], among others. Nevertheless, the limitations mentioned above still need to be addressed.

Enzyme-powered nanomotors have been developed as self-propelled drug carriers that could potentially overcome limitations of drugs and passive NPs due to their continuous momentum. In biomedical applications, nanomotors have been reported to enhance drug transport and delivery[17, 18], and improve penetration into bladder cancer spheroids[19] as well as other tissues[20]. In particular, urease-powered nanomotors have a huge potential for treating and diagnosing bladder cancer since their movement is promoted by the conversion of urea (present in urine) into carbon dioxide and ammonia.

In the previous chapter, we demonstrated that urease nanomotors could be efficiently radiolabelled with the positron emitter fluorine-18 (^{18}F, half-life = 109.7 min), and their motion could be tracked both *in vitro* and *in vivo* using PET imaging[21]. The collective motion observed for urease nanomotors administered in urea promoted convection and mixing inside the bladder, ensuring a homogenous distribution even after the entrance of fresh urine. These features would help to explore wider areas and avoid possible sedimentation of the drug, providing treatment to all areas of the bladder.

Taking a step forward into the application of urease-powered nanomotors as therapeutic tools, in this chapter we evaluate the capacity of urease nanomotors to reach the tumour site in an orthotopic mouse model of bladder cancer using positron emission tomography (PET) in combination with computed tomography (CT), the latter to obtain anatomical information. With this ultra-sensitive, non-invasive, and fully translational imaging tool, nanomotors can be quantified in a time-resolved fashion in bladder tumour tissue.

Experimentally, female mice were intravesically instilled with a bladder carcinoma cell line (MB49). Then, tumour size was monitored by magnetic resonance imaging (MRI) at 7 and 14 days from the cell implantation. MRI is a non-invasive and high-resolution imaging technique that generates three-dimensional anatomical images. This technique is based on the detection of the signals generated from the underlying protons (^{1}H) found in water that makes up living tissues. In fact, MRI is used for the detection of bladder cancer in clinics since its superior resolution allows to obtain information about tumour invasiveness and infiltration, especially in distinguishing between MIBC from NMIBC[22]. Finally, at 15 days from cell instillation, ^{18}F-urease or ^{18}F-BSA (bovine serum albumin) nanomotors were administered within the bladder, and PET imaging studies were conducted to evaluate their capacity to accumulate in the tumour (Figure 4.2). The resulting PET-CT images demonstrated the capacity of urease nanomotors to accumulate more in the tumour tissue compared to the control groups. *Ex vivo* complementary techniques were used to confirm the location of the nanomotors, as well as their penetration into the tumour.

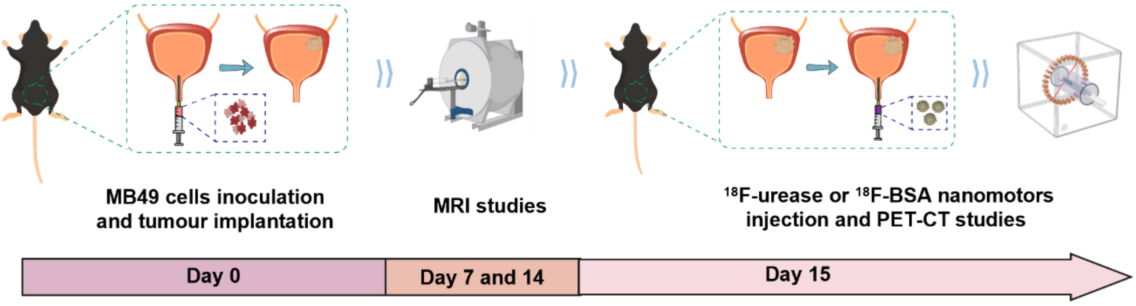

Figure 4.2. Schematic representation and timeline for the study to determine accumulation of nanomotors in bladder tumour masses *in vivo*.

4.2 Objectives

The specific objectives of this chapter are:

1. To implement a mouse model of bladder cancer.
2. To investigate the suitability of MRI technique to monitor tumour growth within the bladder in mice.
3. To evaluate the capacity of ^{18}F-urease nanomotors to accumulate in bladder tumour, when urea is used as vehicle, by using PET imaging and *ex vivo* complementary techniques. To compare accumulation capacity towards ^{18}F-BSA nanomotors.

4.3 Materials and methods

4.3.1 General remarks

As mentioned in Chapter 3, the nanomotors used for *in vivo* imaging by PET, and fluorescein isothiocyanate (FITC)-nanomotors used for immunohistochemistry were synthetized by Prof. Samuel Sánchez's group at Institute for Bioengineering of Catalonia, IBEC (Barcelona, Spain). Furthermore, the orthotopic animal model used was established with the help of Prof. Esther Julián (Autonomous University of Barcelona, UAB; Bellaterra, Spain).

4.3.2 Radiolabelling of nanomotors with [^{18}F]F-PyTFP

Synthesis of [^{18}F]F-PyTFP

[^{18}F]F-PyTFP was synthetized in a Neptis® xSeedTM module (Optimized Radiochemical Applications, ORA, Neuville, Belgium), following a previously reported method[21]. In brief, [^{18}F]Fluorine (produced by proton irradiation of an ^{18}O-enriched water target) was trapped in an ion-exchange resin (Sep-Pak Accell Plus QMA Light, Milford, MA, USA) and subsequently eluted into a reactor vessel in a solution of Kryptofix $K_{2.2.2}/K_2CO_3$ mixture of water and acetonitrile. After azeotropic drying of the solvent, the precursor F-PyTFP in a mixture of *tert*-butanol and acetonitrile (4:1) was added and heated at 40°C for 15 min. The reaction mixture was diluted with acetonitrile (1 mL) and water (1 mL), and purified by semipreparative high performance liquid chromatography (HPLC) using a Nucleosil 100-7 C18 column (Machery-Nagel, Düren, Germany) as the stationary phase and 0.1% trifluoroacetic acid (TFA)/acetonitrile (25:75) as the mobile phase at a flow rate of 3 mL/min. The desired fraction (24-25 min, [^{18}F]F-PyTFP) was collected, diluted with water (30 mL), and flushed through a C18 cartridge (Sep-Pak Light, Waters, Milford, MA, USA) to selectively retain [^{18}F]F-PyTFP. Finally, the desired labelled specie was eluted with acetonitrile (1 mL). Radiochemical purity was determined by radio-HPLC using a Mediterranean C18 column (4.6 mm by 150 mm, 5 µm) as the stationary phase and 0.1% TFA/acetonitrile as the mobile phase (0-1 min 25% acetonitrile; 1-9 min 25-90% acetonitrile; 9-12 min 90% acetonitrile; 12-13 min 90-25% acetonitrile; 13-15 min 25% acetonitrile) at a flow rate of 1.5 mL/min (retention time = 7.5 min).

Synthesis of ^{18}F-urease nanomotors

Urease nanomotors were labelled with [^{18}F]F-PyTFP, based on a previously stablished procedure[21]. In brief, 200 µL of urease nanomotors solution (1 mg/mL) was centrifugated (13853 g, 10 min), re-suspended in 10 µL of phosphate buffered solution (PBS; 10 mM, pH 8) and incubated with 4 µL of [^{18}F]F-PyTFP in acetonitrile (*ca*. 37 MBq) for 35 min at room temperature. After incubation, the reaction mixture was diluted with water (200 µL) and purified by centrifugation (13853g, 5 min). The resulting pellet was then rinsed three times with water before being measured in a dose calibrator (CPCRC-25R, Capintec Inc., NJ, USA) to determine the final amount of radioactivity. Radiochemical yield was calculated as the ratio between the amount of radioactivity present in the nanobots after washing and the initial amount of radioactivity. Radiochemical purity was determined by radio-thin layer chromatography (radio-TLC) using iTLC-SG chromatography paper (Agilent Technologies, CA, USA) and dichloromethane and methanol (2:1) as the stationary and mobile phases, respectively. TLC plates were analysed using a TLC reader (MiniGITA, Raytest, Straubenhardt, Germany).

Synthesis of ^{18}F-BSA nanomotors

The radiofluorination of BSA-nanomotors was performed following the same procedure stablished for ^{18}F-urease nanomotors.

4.3.3 Stability of ^{18}F-nanomotors

The stability of ^{18}F-urease or ^{18}F-BSA nanomotors was determined using the following media: (i) 300 mM urea solution in water; (ii) water; and (iii) urine extracted from tumour-bearing mice. With that aim, 100 µL of the corresponding nanomotor (^{18}F-urease or ^{18}F-BSA) were incubated with the corresponding solution (1 mL for water and urea, and 100 µL for urine) for 1 h at room temperature. Then, nanomotors and supernatant were separated by centrifugation, collected, and the amount of radioactivity was measured in a dose calibrator (CPCRC-25R, Capintec Inc., NJ, USA).

4.3.4 Animal model development

Mice were maintained and handled in accordance with the European Council Directive 2010/63/UE and internal guidelines. All experimental procedures were approved by the ethical committee at CIC biomaGUNE and the local authorities before conducting experimental work. The orthotopic murine model of bladder cancer was generated by intravesical administration of MB49 cells in C57BL/6JRj female mice (8 weeks old, Janvier, *N*= 45; see below for detailed groups and protocol).

For tumour establishment, mice were anesthetized by inhalation of 3% isoflurane in pure O_2 and maintained by 1.0-1.5% isoflurane in 100% O_2. Then, the bladder was emptied by abdominal massage, and chemical lesions were induced on the bladder urothelium by intravesically instilling 50 µL of poly-L-lysine (Sigma-Aldrich) through a 24-gauge catheter for 15 min. Subsequently, bladder was again emptied and 100 µL of MB49 cells (10^5 cells) in DMEM high glucose media were instilled and incubated for 1 h. After that time, the catheter was removed, and the bladder was finally emptied by abdominal massage.

4.3.5 Tumour size monitorization

MRI studies were conducted at t = 7 and 14 days after tumour inoculation, using at 7 Tesla Bruker Biospec USR 70/30 scanner (Bruker Biospin MRI GmbH, Ettlingen) equipped with a BGA-12S gradients' insert of 440 mT/m and using a 112/086 QSN resonator (T12053V3) for radiofrequency (RF) transmission and a rat brain surface coil (T11205V3) for RF reception (both operating at 300 MHz). Animals were anesthetized with isoflurane (4% for induction and 1.5% for maintenance in a mixture 50% O_2/50% N_2) and placed on a MR compatible cradle. Body temperature and respiration rate were continuously monitored using an MR compatible monitoring device (model 1030 SA, Small Animal Instruments, Stony Brook, NY, USA), interfaced to a Small Rodent Air Heater System to maintain body temperature. After acquisition of scout images for reference, a Spin-Echo based Diffusion Weighted Imaging sequence (SE-DWI) was used to image the tumours, using the following imaging parameters: SE-DWI sequence, TE = 22.3 ms, TR = 2500 ms, N = 2 averages, 1 A0 image and on DW image acquired using diffusion gradients in (1, 0, 0) direction, with δ = 4.5 ms and Δ = 10.6 ms, giving a b value of 650 mm^{-2} s, a field of view = 16 x 16 mm^2, image matrix = 160 x 160 points, 20 consecutive slices of 0.5 mm thickness (no gap, acquired in interleaved mode), and a bandwidth of 192.9 Hz/pixel.

To facilitate the visualization of the tumours, images were postprocessed with ImageJ software, dividing the set of images acquired with diffusion gradient (b=650 mm^{-2} s) by the set of images acquired without diffusion gradients (b=0 mm^{-2} s), and applying a Gaussian 3D filter (σx ,σy. σz = 0.7) to the resulting image. To determine tumour volume, VOIs were manually drawn on each slice covering the tumour area.

4.3.6 *In vivo* biodistribution of radiolabelled nanomotors

At t = 15 days from cell implantation, PET-CT imaging studies (MOLECUBES β and X-CUBE scanners, MOLECUBES, Gent, Belgium) were conducted at t = 3 hours after intravesical administration of 100 µL of ^{18}F-BSA (0.17 mg/mL; groups 1 and 2, *N* = 6 per group) or ^{18}F-urease (0.17 mg/mL; groups 3 and 4, *N* = 6 per group) nanomotors, administered using either ultrapure water (groups 1 and 3) or 300 mM urea solution in water (groups 2 and 4) as the vehicle (table 4.1 for details).

The experimental procedure for image acquisition was the following: Animals were induced with anaesthesia (5% isoflurane in pure O_2) and positioned in supine position. The bladder was emptied by massaging the abdominal region. Immediately after, the corresponding ^{18}F-labelled particle (^{18}F-BSA or ^{18}F- urease nanomotors) were instilled in the bladder through a 24-gauge catheter, using the appropriate vehicle according to the experimental group (water or 300 mM urea solution in water). The solution containing the labelled specie was allowed to stay in the bladder for 1 h. After that time, the catheter was removed, the bladder was emptied by abdominal massage, and mice were recovered from the anaesthesia in their cages. At t = 3 h after administration, animals were re-anaesthetized and 10-minutes static whole-body PET images were acquired, followed by CT acquisitions.

PET images were reconstructed using 3D OSEM reconstruction algorithm and applying random, scatter and attenuation corrections. PET-CT images of the same mouse were co-registered and analysed using PMOD image processing tool. To get the concentration of radioactivity, 3D contour tool was used to create a VOI on the upper region of the bladder. Activity values (decay corrected) were obtained as KBq/organ. Activity concentration was corrected by applying a calibration factor obtained from previous scans performed on a phantom (micro-deluxe, Data spectrum Corp.) under the same experimental conditions (isotope, reconstruction algorithm and energetic window). Resulting values were normalised to tumour volume previously obtained by MRI.

4.3.7 *Ex vivo* studies

4.3.7.1 Histopathological analysis

After the last imaging session, selected bladders (*N* = 3 per group; 4 groups), and healthy bladders were immediately fixed in formaldehyde 4% after their collection. Then, bladders were embedded in paraffin, and 2-3 µm-sections of were performed for hematoxylin-eosin staining. Representative images were obtained from all conditions for histopathologic examination.

4.3.7.2 ICP-MS analysis

Inductively coupled plasma-mass spectrometry (ICP-MS) measurements were performed on a Thermo iCAP Q ICP-MS instrument (Thermo Fisher Scientific GmbH, Bremen, Germany), coupled with ASX-560 autosampler (CETAC Tech, Omaha, NE, USA). After the last imaging session, animals were sacrificed, and selected bladders (*N* = 2 per group; 4 groups) were collected. Bladders were digested in a mixture of HNO_3/HCl (4:1) with a volume of 1 mL. The dispersion was heated to boiling until organs were completely dissolved. Then, the solution was cooled to room temperature and analysed by ICP-MS to determine the concentration of Au in each sample. Values were finally transformed into percentage of injected dose per g of tissue (%ID/g).

4.3.7.3 Immunohistochemistry

For immunohistochemistry analyses, tumour-bearing animals were administered with FITC-urease nanomotors in either water or 300 mM urea solution in water (*N* = 4 per group), following the same procedure described above for PET-CT studies. Additionally, tumour-bearing animals in absence of nanomotors were used as controls (*N* = 2). In all cases, bladders were harvested, frozen, and cut in 10 µm-sections. Sections were immediately fixed in formaldehyde 10% during 15 min, washed with PBS (10 mM, pH 7.4) and incubated in 50 Mm NH_4Cl in PBS (10 mM, pH 7.4) for 5 min, followed by another PBS rinse. Permeabilization was performed with methanol/acetone (1:1) for 5 min at room temperature, and 0.1% triton in PBS (10 mM, pH 7.4) for 5 min. After PBS washing, samples were saturated with a solution of 5% BSA/0.5% Tween in PBS for 15 min at room temperature and incubated during 1 h at room temperature with mouse anti-FITC (1:100, AbCam, Cambridge, UK) 5% BSA/0.5% Tween. Sections were washed 3 times with PBS (10 mM, pH 7.4) for 5 min and incubated for 30 min at room temperature with secondary antibody Alex Fluor 647 donkey anti-mouse IgG (Molecular Probes, Life Technologies, Madrid, Spain, 1:1000) in 5% BSA/0.5% Tween in PBS, washed again in PBS (10 mM, pH 7.4; 3 x 5 min), and mounted with a prolong antifade kit with DAPI (Molecular Probes Life Technologies, Madrid, Spain). Standardized images acquisition was performed with the Leica Stellaris 5 microscope (UPV/EHU Scientific Park, Spain). The tumour fluorescence was analysed by ImageJ software.

4.3.8 Statistical analysis

For PET imaging studies, values of percentage of injected dose (% ID) and percentage of injected dose per volume of tumour (% ID/cm^3) within each group were compared using one-way ANOVA. Differences between groups were determined using Turkey's multiple comparisons test. For immunohistochemistry analyses, values of tumoral fluorescence for each group were averaged and compared using the same statistical method. Differences were concluded significant for p values < 0.05: $p < 0.05$, *; and $p < 0.01$, **. Statistical analyses were performed with GraphPad Prism version 8.0.

4.4 Results and discussion

4.4.1 Tumour model and monitorization of tumour size

Different animal models have been developed to investigate bladder cancer[23]. These can be classified as spontaneous, which include chemically induced and genetically engineered models, and transplantable. The latter can be sub-classified as syngeneic, which corresponds to murine bladder cancer cells implanted to syngeneic, immunocompetent, or transgenic mice, and xenograft, which are generated by implantation of human bladder cancer cells to immunodeficient mice. For this study, we used an orthotopic syngeneic transplantable model, based on the intravesical implantation of bladder carcinoma cells (MB49) in 8 weeks old C57Bl/6 female mice. This model has been widely used in therapeutic experiments[24] as it allows the tumour to arise in immunocompetent mice, thus reflecting the role of the immune system. Additionally, this model was well established in the laboratory of our collaborator (Prof. Esther Julián, UAB, Bellaterra) and hence the implementation at CIC biomaGUNE was straightforward.

Tumour formation was achieved by traumatization of the urothelium by intravesical pretreatment with poly-L-lysine, followed by intravesical instillation of 1 x 10^5 MB49 tumour cells that attach to the damaged surface. Animals were weighted daily.

A critical point in preclinical evaluation of novel treatments is the assessment and control of tumour size when randomizing mice among the different groups. In this chapter, we decided to use MRI to monitor tumour size and use the obtained volume values to randomize mice for the subsequent *in vivo* PET studies.

Previous studies performed in bladder cancer models used bioluminescence[25] or ultrasound imaging[26] to evaluate tumour growth. Both techniques present some disadvantages related to lack spatial resolution or the use of cell lines which express bioluminescent genes. On the contrary, MRI offers three-dimensional information and high spatial resolution, allowing the visualization of bladder anatomy and morphology[27]. In this study, two MRI sessions were established at 7 and 14 days after cell implantation in order to monitor the tumour size over time (Figure 4.3a). MRI images obtained clearly show the presence of the tumour as a grey mass in the upper part of the bladder. Moreover, analysing MRI images by Image J software, values of tumour volume could be obtained, and difference of tumour size could be quantified between both MRI sessions.

In total 35 animals were inoculated with MB49 cell line, of which 28 developed bladder tumours bigger than 1 mm^3, with average volumes of 6.8 ± 6.4 and 17.1 ± 14.1 mm^3 at 7 and 14 days after cell instillation. This tumour growing rate was as expected since the tumour implantation ratio of MB49 cell line has been described with an efficiency between 80-100%[28, 29]. The general trend observed for most of the animals was a significant increase of the tumour size over time (Figure 4.3b). Nevertheless, some animals showed smaller tumours with invariable size or with slightly descending trend between both MRI sessions. This can be explained by the fact that MB49 cells were originally isolated from a male mouse and express the H-Y antigen. Therefore, MB49 cell line is immunogenic, and some mice can be spontaneously cured after implantation[30]. From them, only mice with tumour volume increasing over time were selected (*N* = 24) and randomized in four groups to undergo the subsequent PET studies (Figure 4.3c). Randomization was performed by distributing from the largest to the smallest values of tumour volume between the four groups, always ensuring that average values were uniform among the groups.

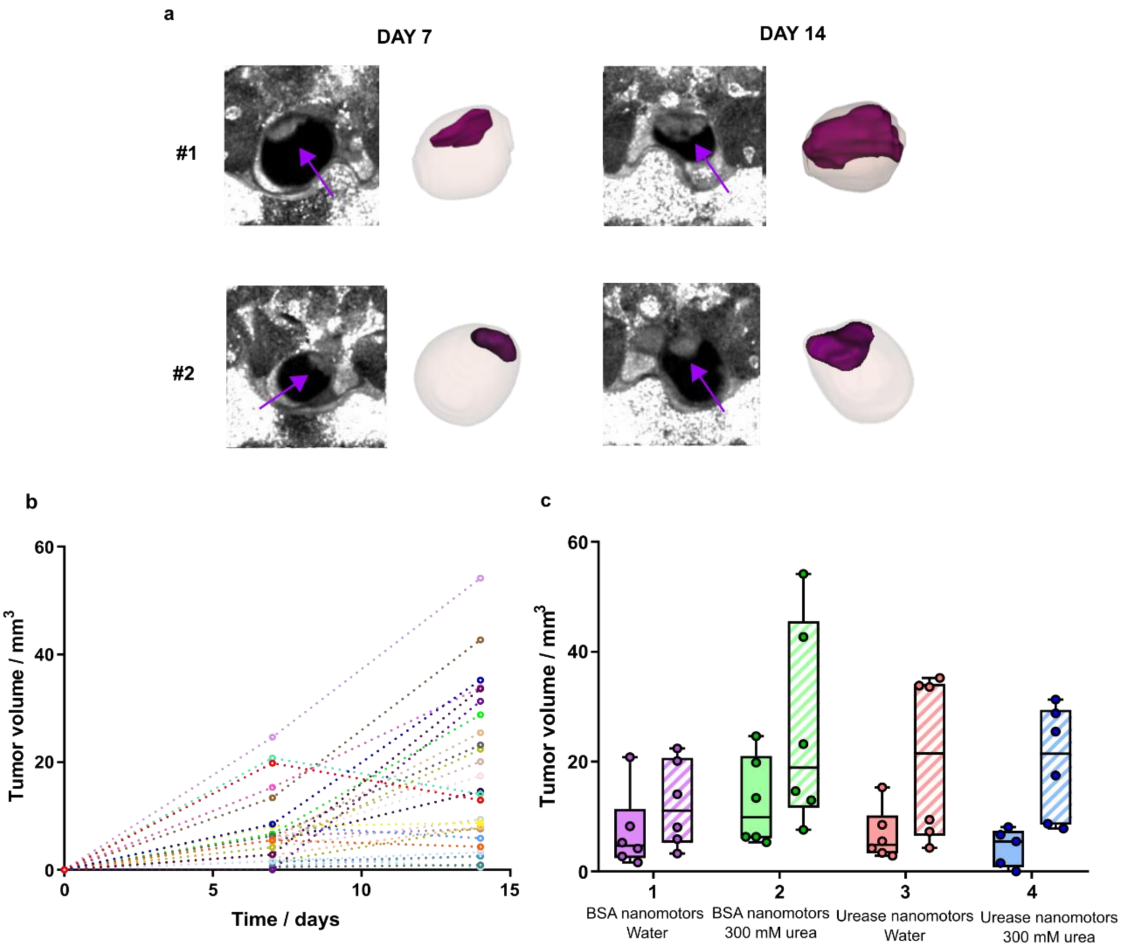

Figure 4.3. a) Representative MRI images of two animals at 7 and 14 days after MB49 cell instillation. The position of the tumour is indicated with a purple narrow. On the right of the MRI images, 3D-rendered images of the bladder (white) and tumour (purple) are shown. b) Tumour volume growth determined by MRI for all animals developing tumour (N=28) at 7 and 14 days after cell inoculation. c) Distribution of tumour volume values determined by MRI within the four experimental groups. Dots represent each individual tumour value at 7 and 14 days after cell instillation (*N* = 6 per group). 1: ^{18}F-BSA nanomotors administered in water; 2: ^{18}F-BSA nanomotors administered in 300 mM urea; 3: ^{18}F-Urease nanomotors administered in water; 4: ^{18}F-Urease nanomotors administered in 300 mM urea.

4.4.2 Determination and quantification of tumour uptake

In the previous chapter, we demonstrated that urease-powered nanomotors can swim within a healthy bladder when administered with 300 mM urea solution in water. By contrast, urease-powered nanomotors injected in water as the vehicle, did not show self-propelling capacity and generated a 2-phase system after the entrance of fresh urine into the bladder[21]. Similar results were found when BSA nanomotors were administered within the bladder either with 300 mM urea solution in water or ultrapure water. Here, we decided to explore tumour accumulation of urease-powered nanomotors in an orthotopic model of bladder cancer.

To determine tumour accumulation and subsequent quantification, we decided to conduct the study using PET imaging. PET offers certain key advantages with respect to other imaging techniques previously employed to evaluate and quantify nanomotors within the bladder, including fluorescence imaging[31] or MRI imaging[32]. As previously stated, PET is a non-invasive and fully translational technique that enables the quantification of sub-pharmacological amounts of radiolabelled entities at the whole-body level both in preclinical and clinical settings. CT was used in combination with PET to obtain anatomical information, and the attenuation map for correction during image reconstruction.

With that aim, BSA and urease nanomotors were labelled with the positron emitter ^{18}F. Radiofluorination was achieved following the same procedure described in Chapter 3 based on the condensation of a pre-labelled prosthetic group ([^{18}F]F-PyTFP) with the amino groups present on the enzyme (Figure 4.4a). Equivalent yields (30% decay-corrected) and radiochemical purity (≥ 95%) to those previously reported were obtained (Figure 4.4b).

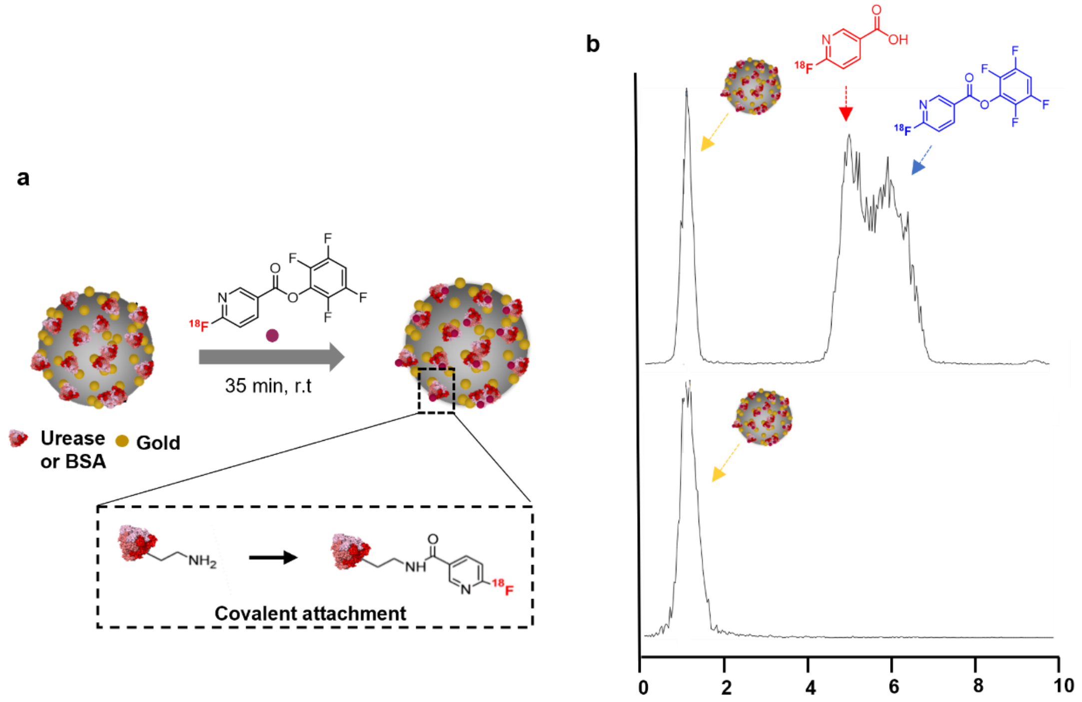

Figure 4.4. a) Schematic representation of radiolabelling of BSA or urease nanomotors by covalent attachment of [^{18}F]F-PyTFP. b) Representative radio-TLC chromatograms of ^{18}F-urease nanomotors before (top) and after (below) purification.

Stability studies were performed in water, 300 mM urea solution and urine extracted from tumour-bearing to ensure radiochemical stability during the whole *in vivo* imaging study. For this, labelled nanomotors (BSA or urease) were incubated during 1 h with all three solutions. In water and 300 mM urea solution, radiochemical purity was ≥ 95%, while only a 60% was obtained in urine, suggesting a certain label detachment. This could be a problem for the subsequent PET studies since the resulting image accounts for all radiolabelled species present in the organ. As partial label detachment may lead to misinterpretation of the obtained results, the urine present in the bladder was evacuated prior to injecting the radiolabelled nanomotors. This strategy guarantees a prolonged *in vivo* stability of the labelled nanomotors, as these proved stable both in water and in urea solution.

After the radiolabelling procedure, four different scenarios were defined to explore tumour accumulation of the nanomotors using PET imaging. Animals were administered with: (1) ^{18}F-BSA nanomotors using water as vehicle; (2) ^{18}F-BSA nanomotors using 300 mM urea solution as vehicle; (3)^{18}F-urease nanomotors using water as vehicle; and (4) ^{18}F-urease nanomotors using 300 mM urea solution as vehicle (Table 4.1). An additional control group was included, comprising non-bearing tumour animals administered with ^{18}F-urease nanomotors in 300 mM urea solution as vehicle.

Table 4.1. Summary of the different experimental scenarios performed *in vivo*.

Group	***N***	**^{18}F-Enzyme**	**Vehicle**
Control	3*	Urease	Urea
1	6	BSA	Water
2	6	BSA	Urea
3	6	Urease	Water
4	6	Urease	Urea

**non-tumour bearing animals; N: number of animals in each group*

For PET studies, independent of the study group, all animals with the empty bladder received an intravesical administration of the corresponding labelled particle and vehicle, which were left for 1 h. We decided to incubate the labelled solution for 1 h following the same procedure applied for the tumour implantation. To ensure that the radioactive signal came only from nanomotors attached to the tumour (and not residual radioactivity in the urine), PET acquisitions were performed 3 h after administration and right after bladder evacuation, followed by CT scans.

Firstly, we decided to study the nanomotors' adhesion to the healthy bladder by performing a control study in a non-tumour bearing mice. For this preliminary study, only ^{18}F-urease nanomotors administered with 300 mM urea solution in water were used as they show motile properties. The resulting PET images did not show presence of radioactivity within the bladder (Figure 4.5a; control). Quantification of the PET images only showed a negligible fraction of radioactivity retained in the bladder, *ca*. 0.02 % ID (Figure 4.5b; control), confirming the low adherence and/or penetration capacity of labelled urease-powered nanomotors in healthy bladder.

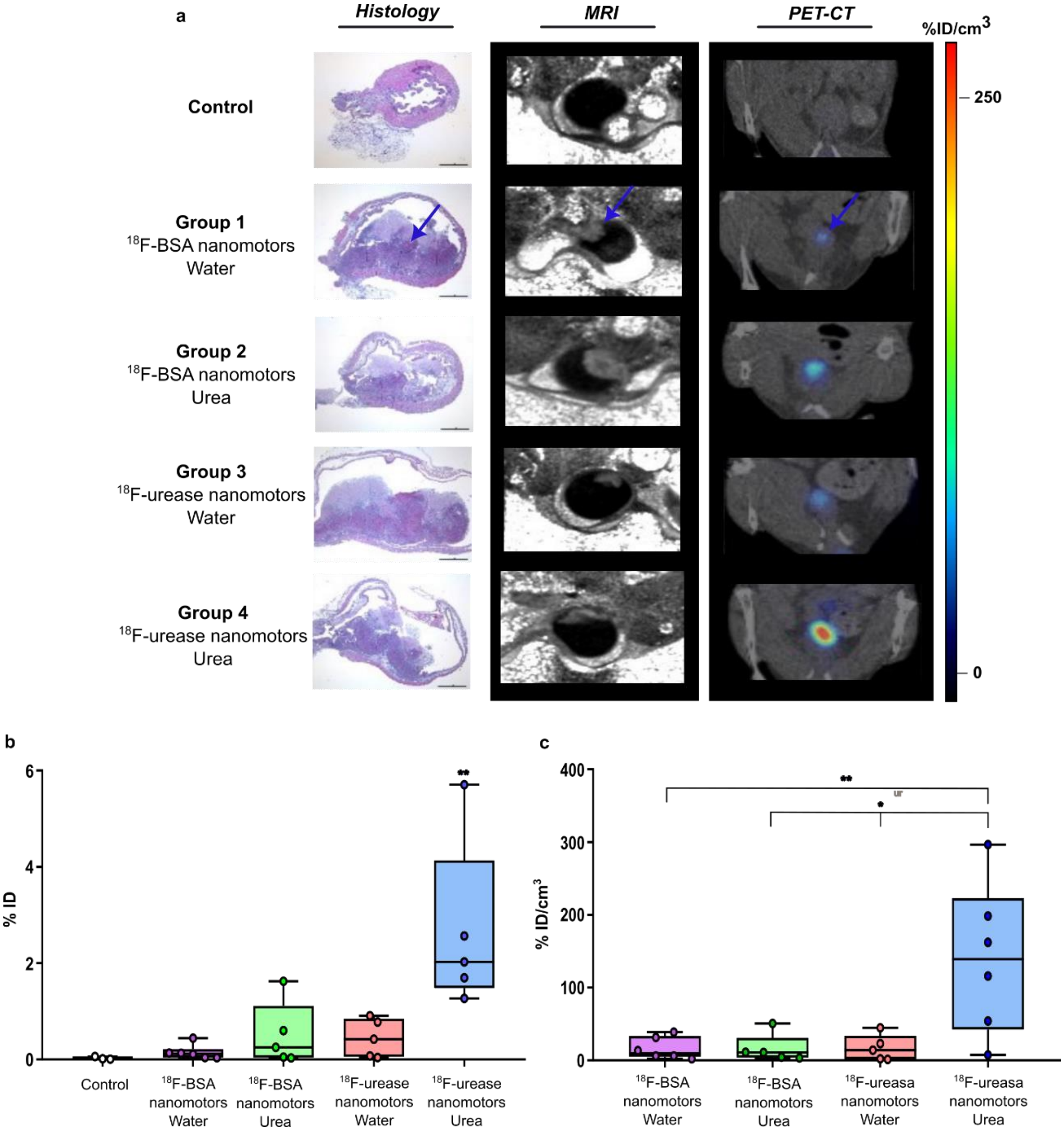

Figure 4.5. a) Representative histological images of hematoxylin-eosin staining, MRI and PET-CT images of animals corresponding to control animals and animals included in groups 1-4. For histopathological images scale bar corresponds to 1 mm; PET slices have been corregistered with the corresponding CT slice for anatomical localization of the radioactive signal. b) Accumulation of radioactivity in the tumour for control animals and animals included in groups 1-4, as determined from PET images, expressed as percentage of injected dose in the whole tumour (% ID). c) Accumulation of radioactivity in the tumour for animals included in groups 1-4, normalised to tumour volume as determined by MRI. Control: ^{18}F-urease nanomotors administered with 300 mM urea solution in water in healthy mice; group 1: ^{18}F-BSA nanomotors administered with water; group 2: ^{18}F-BSA nanomotors administered with 300 mM urea solution; group 3: ^{18}F-urease nanomotors administered with water; and group 4: ^{18}F-urease nanomotors administered with 300 mM urea solution. **$p < 0.01$; *$p < 0.05$.

After confirming the absence of ^{18}F-urease nanomotors uptake in healthy bladder, studies with tumour-bearing mice were carried out. In all cases, PET images revealed the presence of radioactive signal in the upper part of the bladder, whose position coincides with the location of the tumour according to MRI images (Figure 4.5a; groups 1-4). Visual inspection of the images already revealed a higher tumour accumulation for ^{18}F-urease nanomotors administered in urea (group 4), thus suggesting a positive effect of urease nanomotors' motion on tumour uptake in the presence of urea. From the quantification of PET images (Figure 4.5b), the highest uptake was observed for ^{18}F-urease nanomotors when urea was used as vehicle (group 4, *ca*. 2.5 %ID). Contrary, ^{18}F-urease nanomotors administered in water (group 3) and ^{18}F-BSA nanomotors administered both in water and urea (groups 1 and 2, respectively) showed average tumour uptake below 1 %ID.

With the aim of normalising the amount of radioactivity accumulated in the tumour to the tumour volume, values were finally expressed as percentage of injected dose per volume of tumour (% ID/cm^3, Figure 4.5c), the latter determined from MRI images. Values obtained confirm significant uptake increase in the tumour (p = 0.073, 0.0104, and 0.0111 with respect to groups 1, 2, and 3, respectively) for group 4 (*ca*. 150 % ID/cm^3), confirming the positive effect of active motion in tumour accumulation. Interestingly, values for groups 1-3 were statistically equivalent (*ca*. < 20 % ID/cm^3; p values for 1-2, 1-3, and 2-3 > 0.9999) suggesting that the enzyme decoration on the nanomotor surface and the vehicle used for the administration do not have a net effect on tumour uptake.

After the imaging study, and with the objective to corroborate tumour size equality between groups, histopathological assessments using hematoxylin-eosin staining were performed in selected animals. In all the cases, bladders presented a solid mass, which corresponds to the tumour under the *lamina propria* with infiltration of mononuclear and polymorphonuclear inflammatory cells. Moreover, no differences were observed among the groups (Figure 4.5a; groups 1-4).

As previously mentioned, the stability of labelled nanomotors in urine of tumour-bearing animals was 60% after 1 hour. Even though bladders were evacuated before injection, animals can produce fresh urine during the incubation process, and consequently certain detachment of the prosthetic group from nanomotors surface could be expected. To confirm that PET imaging faithfully quantified the amount of nanomotors accumulated in the tumour and taking advantage of the presence of gold (Au) into the surface of nanomotors, ICP-MS was used to quantify the concentration of Au in the tumour. With that aim, selected animals were sacrificed immediately after the PET session, bladders were excised, and after radioactive-decay they were processed to be analysed by ICP-MS (Figure 4.6).

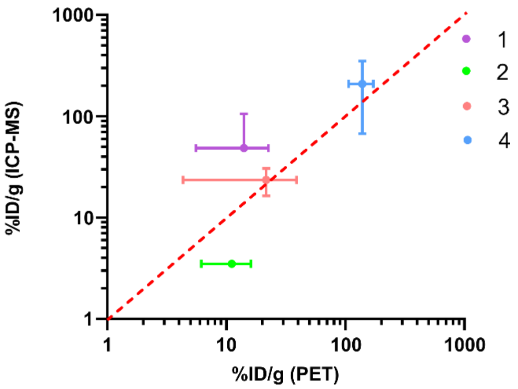

Figure 4.6. Correlation of tumour accumulation obtained by PET imaging and ICP-MS (mean ± SD, *N* = 2 per type of nanomotor and vehicle). 1: BSA nanomotors administered with water; 2: BSA nanomotors administered with 300 mM urea solution in water; 3: urease nanomotors administered with water; and 4: urease nanomotors administered with 300 mM urea solution in water.

A good correlation was achieved between the results obtained by PET and by ICP-MS, confirming that despite it is expected that part of the radiolabel detaches from nanomotors, this does not have a net effect on tumour accumulation. Slight deviations obtained between both techniques could be due to inaccuracies in the delineation of the VOI in the PET images or partial volume effect, as bladder tumours are relatively small when compared to the spatial resolution of the PET system, which is 1 mm in the centre of the field of view.

4.4.3 Distribution within the tumour

One important aspect, beyond absolute values of accumulation, is the regional distribution of the nanomotors within the tumour. The main question remaining was the effect of self-motile properties in tumour penetration. Unfortunately, the resolution of PET imaging was insufficient to obtain in-depth radioactivity profiles in the tumours. Therefore, we decided to complement our studies with confocal fluorescence microscopy using FITC-urease nanomotors to determine the distribution of urease-powered nanomotors within the body of urinary bladder and penetration to the tumour.

With that aim, 10 female mice were inoculated intravesically with MB49 cells, and tumour growth was monitored at days 7 and 14 after cell implantation by MRI, following the same procedure described above. For confocal fluorescence microscopy, animals were randomised in three groups: (1) FITC-urease nanomotors administered in ultrapure water; (2) FITC-urease nanomotors administered in 300 mM urea solution in water; and (3) absence of nanomotors (control). The procedure of administration of FITC-nanomotors was the same described for PET imaging studies (1 h incubation). After 3 h post-administration, animals were sacrificed, and the bladders were collected, frozen and sent to the Neuroimaging and Biomarkers of Inflammation Group at Achucarro (Bilbao, Spain), where confocal fluorescence microscopy studies were performed in collaboration with the group of Dr. Abraham Martín.

Representative confocal tumour bladder images showed a negligible accumulation of nanomotors in the body of urinary bladder for FITC-urease nanomotors administered with either ultrapure water or 300 mM urea solution in water. Moreover, higher tumour penetration was observed for FITC-urease nanomotors administered in 300 mM urea solution as vehicle (Figure 4.7a). These results are in good agreement with the quantification of tumoral fluorescence, where significant tumour uptake was obtained for those tumours administered with FITC-urease nanomotors in urea in comparison to those administered with water and control (*p* = 0.0085 and 0.0053, respectively; Figure 4.7b)

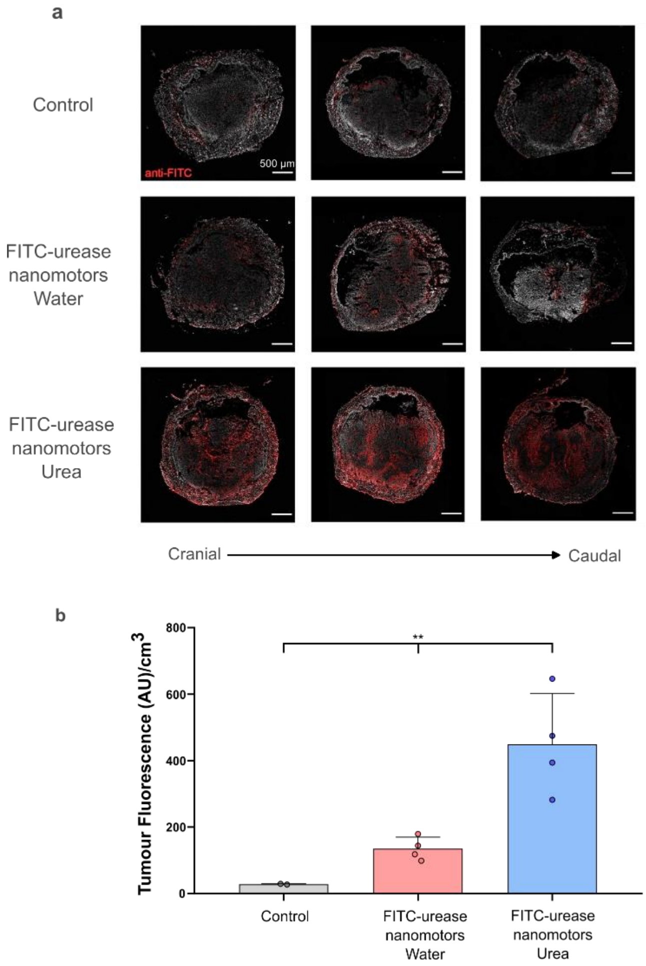

Figure 4.7. a) Representative confocal images obtained from the immunofluorescence labelling of anti-FITC (red) in three different sections of the same untreated tumour (control), treated with FITC-urease nanomotors administered in ultrapure water, and treated with urease nanomotors administered in 300 mM urea solution in water. b) Tumour fluorescence quantification in tumour for untreated group (control, *N* = 2), treated with FITC-urease nanomotors administered in water (*N* = 4), and treated with FITC-urease nanomotors administered in 300 mM urea solution in water (*N* = 4). ***p* < 0.01.

The results obtained by confocal fluorescence microscopy support both *in vivo* PET imaging and *ex vivo* ICP-MS with respect to urease nanomotors tumour accumulation, when urea is used as the vehicle. Furthermore, they clearly show not only a superficial accumulation of the urease nanomotors in the tumour, but also their penetrability within the bladder tumour.

These findings are very promising since the mucosa layer of the bladder is designed to protect bladder surface from therapeutic agents[3]. Therefore, it is not easy to deliver drugs through it. Few examples can be found in the literature using urease-driven nanomotors in the bladder[33]. Choi et al. used urease-powered polydopamine nanomotors to penetrate into the bladder wall by self-propulsion and remain there even after urination due to the mucoadhesive properties of the polymer[31]. Xu et al. described the use of urease-powered liquid metal nanomotors as dual-mode imaging platform. They concluded that these nanosystems showed promise as imaging-guided therapeutic agents for bladder illnesses[34]. Finally, our collaborator (Prof. Samuel Sánchez, IBEC, Barcelona) showed *in vitro* increased penetration (3-fold higher) of urease-powered nanomotors in the presence of urea compared to absence of the fuel in bladder cancer 3D spheroids[19]. The results described in this thesis are in agreement with these previous studies but go one step further, showing that the active motion of nanomotors enhance the penetration in tumour bladder tissue compared to passive particles.

4.5 Summary and conclusions

In this chapter, we used a well-stablish orthotopic model of bladder cancer to evaluate the capacity of urease nanomotors to reach the tumour tissue. MRI was used to monitor the tumour growth within the bladder and randomize animals for subsequent PET imaging studies. The corresponding protein attached to the surface of the nanomotor (either urease or BSA) was labelled with [^{18}F]-FPyTFP, following the same methodology reported in Chapter 3. Finally, PET sessions were performed after intravesical administration of the labelled nanomotors to evaluate tumour accumulation. *Ex vivo* techniques were used to corroborate the results obtained.

The work presented in this chapter shows an increased tumour accumulation for those urease nanomotors administered in urea (5-fold increase) compared to their passive counterparts, thanks to their active motile properties. The results obtained were confirmed by ICP-MS and immunofluorescence. These results add value to the previously reported properties of the nanomotors and position them as promising drug delivery systems for cancer therapy.

4.6 References

(1) Bray, F.; Ferlay, J.; Soerjomataram, I.; Siegel, R. L.; Torre, L. A.; Jemal, A., Global cancer statistics 2018: GLOBOCAN estimates of incidence and mortality worldwide for 36 cancers in 185 countries. *CA Cancer J Clin* **2018,** *68* (6), 394-424.

(2) Siegel, R. L.; Miller, K. D.; Fuchs, H. E.; Jemal, A., Cancer statistics, 2022. *CA Cancer J Clin* **2022,** *72* (1), 7-33.

(3) Richters, A.; Aben, K. K. H.; Kiemeney, L., The global burden of urinary bladder cancer: an update. *World J Urol* **2020,** *38* (8), 1895-1904.

(4) Saginala, K.; Barsouk, A.; Aluru, J. S.; Rawla, P.; Padala, S. A.; Barsouk, A., Epidemiology of Bladder Cancer. *Med Sci (Basel)* **2020,** *8* (1), 15.

(5) Chang, S. S.; Boorjian, S. A.; Chou, R.; Clark, P. E.; Daneshmand, S.; Konety, B. R.; Pruthi, R.; Quale, D. Z.; Ritch, C. R.; Seigne, J. D.; Skinner, E. C.; Smith, N. D.; McKiernan, J. M., Diagnosis and Treatment of Non-Muscle Invasive Bladder Cancer: AUA/SUO Guideline. *Journal of Urology* **2016,** *196* (4), 1021-1029.

(6) Meyer, R. K.; Williams, S. J.; Lee, T. Y., Mycobacterium bovis infection of a femorofemoral bypass graft following intravesical Bacillus Calmette-Guerin (BCG) immunotherapy. *J Clin Tuberc Other Mycobact Dis* **2020,** *19*, 100152.

(7) Volpe, A.; Racioppi M Fau - D'Agostino, D.; D'Agostino D Fau - Cappa, E.; Cappa E Fau - Filianoti, A.; Filianoti A Fau - Bassi, P. F.; Bassi, P. F., Mitomycin C for the treatment of bladder cancer. *Minerva Urologica e Nefrologica* **2010,** *62* (2), 133-44.

(8) Antoni, S.; Ferlay, J.; Soerjomataram, I.; Znaor, A.; Jemal, A.; Bray, F., Bladder Cancer Incidence and Mortality: A Global Overview and Recent Trends. *Eur Urol* **2017,** *71* (1), 96-108.

(9) Svatek, R. S.; Hollenbeck, B. K.; Holmang, S.; Lee, R.; Kim, S. P.; Stenzl, A.; Lotan, Y., The economics of bladder cancer: costs and considerations of caring for this disease. *Eur Urol* **2014,** *66* (2), 253-62.

(10) GuhaSarkar, S.; Banerjee, R., Intravesical drug delivery: Challenges, current status, opportunities and novel strategies. *J Control Release* **2010,** *148* (2), 147-59.

(11) Wirth, M.; Plattner, V. E.; Gabor, F., Strategies to improve drug delivery in bladder cancer therapy. *Expert Opin Drug Deliv* **2009,** *6* (7), 727-44.

(12) Blanco, E.; Shen, H.; Ferrari, M., Principles of nanoparticle design for overcoming biological barriers to drug delivery. *Nat Biotechnol* **2015,** *33* (9), 941-51.

(13) Kou, L.; Bhutia, Y. D.; Yao, Q.; He, Z.; Sun, J.; Ganapathy, V., Transporter-Guided Delivery of Nanoparticles to Improve Drug Permeation across Cellular Barriers and Drug Exposure to Selective Cell Types. *Front Pharmacol* **2018,** *9*, 27.

(14) Xu, X.; Liu, K.; Jiao, B.; Luo, K.; Ren, J.; Zhang, G.; Yu, Q.; Gan, Z., Mucoadhesive nanoparticles based on ROS activated gambogic acid prodrug for safe and efficient intravesical instillation chemotherapy of bladder cancer. *J Control Release* **2020,** *324*, 493-504.

(15) Kaldybekov, D. B.; Tonglairoum, P.; Opanasopit, P.; Khutoryanskiy, V. V., Mucoadhesive maleimide-functionalised liposomes for drug delivery to urinary bladder. *Eur J Pharm Sci* **2018,** *111*, 83-90.

(16) Rieger, C.; Kunhardt, D.; Kaufmann, A.; Schendel, D.; Huebner, D.; Erdmann, K.; Propping, S.; Wirth, M. P.; Schwenzer, B.; Fuessel, S.; Hampel, S., Characterization of different carbon nanotubes for the development of a mucoadhesive drug delivery system for intravesical treatment of bladder cancer. *Int J Pharm* **2015,** *479* (2), 357-63.

(17) Hansen-Bruhn, M.; de Avila, B. E.; Beltran-Gastelum, M.; Zhao, J.; Ramirez-Herrera, D. E.; Angsantikul, P.; Vesterager Gothelf, K.; Zhang, L.; Wang, J., Active Intracellular Delivery of a Cas9/sgRNA Complex Using Ultrasound-Propelled Nanomotors. *Angew Chem Int Ed Engl* **2018,** *57* (10), 2657-2661.

(18) Orozco, J.; Cortes, A.; Cheng, G.; Sattayasamitsathit, S.; Gao, W.; Feng, X.; Shen, Y.; Wang, J., Molecularly imprinted polymer-based catalytic micromotors for selective protein transport. *J Am Chem Soc* **2013,** *135* (14), 5336-9.

(19) Hortelao, A. C.; Carrascosa, R.; Murillo-Cremaes, N.; Patino, T.; Sanchez, S., Targeting 3D Bladder Cancer Spheroids with Urease-Powered Nanomotors. *ACS Nano* **2019,** *13* (1), 429-439.

(20) Xi, W.; Solovev, A. A.; Ananth, A. N.; Gracias, D. H.; Sanchez, S.; Schmidt, O. G., Rolled-up magnetic microdrillers: towards remotely controlled minimally invasive surgery. *Nanoscale* **2013,** *5* (4), 1294-1297.

(21) Hortelao, A. C.; Simó, C.; Guix, M.; Guallar-Garrido, S.; Julián, E.; Vilela, D.; Rejc, L.; Ramos-Cabrer, P.; Cossío, U.; Gómez-Vallejo, V.; Patiño, T.; Llop, J.; Sánchez, S., Swarming behavior and in vivo monitoring of enzymatic nanomotors within the bladder. **2021,** *6* (52), eabd2823.

(22) Abouelkheir, R. T.; Abdelhamid, A.; Abou El-Ghar, M.; El-Diasty, T., Imaging of Bladder Cancer: Standard Applications and Future Trends. *Medicina (Kaunas)* **2021,** *57* (3), 220.

(23) John, B. A.; Said, N., Insights from animal models of bladder cancer: recent advances, challenges, and opportunities. *Oncotarget* **2017,** *8* (34), 57766–57781.

(24) Noguera-Ortega, E.; Rabanal, R. M.; Gomez-Mora, E.; Cabrera, C.; Luquin, M.; Julian, E., Intravesical Mycobacterium brumae triggers both local and systemic immunotherapeutic responses against bladder cancer in mice. *Sci Rep* **2018,** *8* (1), 15102.

(25) Jurczok, A.; Fornara, P.; Soling, A., Bioluminescence imaging to monitor bladder cancer cell adhesion in vivo: a new approach to optimize a syngeneic, orthotopic, murine bladder cancer model. *BJU Int* **2008,** *101* (1), 120-4.

(26) Patel, A. R.; Chan, E. S.; Hansel, D. E.; Powell, C. T.; Heston, W. D.; Larchian, W. A., Transabdominal micro-ultrasound imaging of bladder cancer in a mouse model: a validation study. *Urology* **2010,** *75* (4), 799-804.

(27) Glaser, A. P.; Procissi, D.; Yu, Y.; Meeks, J. J., Magnetic Resonance Imaging Assessment of Carcinogen-induced Murine Bladder Tumors. *J Vis Exp* **2019,** (145), e59101.

(28) Chan, E.; Patel, A.; Heston, W.; Larchian, W., Mouse orthotopic models for bladder cancer research. *BJU Int* **2009,** *104* (9), 1286-91.

(29) Chan, E. S.; Patel, A. R.; Smith, A. K.; Klein, J. B.; Thomas, A. A.; Heston, W. D.; Larchian, W. A., Optimizing orthotopic bladder tumor implantation in a syngeneic mouse model. *J Urol* **2009,** *182* (6), 2926-31.

(30) Tham, S. M.; Ng, K. H.; Pook, S. H.; Esuvaranathan, K.; Mahendran, R., Tumor and microenvironment modification during progression of murine orthotopic bladder cancer. *Clin Dev Immunol* **2011,** *2011*, 865684.

(31) Choi, H.; Cho, S. H.; Hahn, S. K., Urease-Powered Polydopamine Nanomotors for Intravesical Therapy of Bladder Diseases. *ACS Nano* **2020,** *14* (6), 6683-6692.

(32) Zheng, S.; Wang, Y.; Pan, S.; Ma, E.; Jin, S.; Jiao, M.; Wang, W.; Li, J.; Xu, K.; Wang, H., Biocompatible Nanomotors as Active Diagnostic Imaging Agents for Enhanced Magnetic Resonance Imaging of Tumor Tissues In Vivo. *Advanced Functional Materials* **2021,** *31* (24), 2100936.

(33) Lv, J.; Xing, Y.; Xu, T.; Zhang, X.; Du, X., Advanced micro/nanomotors for enhanced bioadhesion and tissue penetration. *Applied Materials Today* **2021,** *23*, 101034.

(34) Xu, D.; Hu, J.; Pan, X.; Sanchez, S.; Yan, X.; Ma, X., Enzyme-Powered Liquid Metal Nanobots Endowed with Multiple Biomedical Functions. *ACS Nano* **2021,** *15* (7), 11543-11554.

CHAPTER 5

PRELIMINARY STUDY OF ^{131}I-UREASE NANOMOTORS AS THERAPEUTIC AGENTS FOR BLADDER CANCER

Chapter 5: Preliminary study of ^{131}I-urease nanomotors as therapeutic agents for bladder cancer.

5.1 Introduction

In recent years, many efforts have been directed to improve the actual diagnosis and treatments of different types of cancer. Ideally, the chosen treatment should eradicate the tumour cells while minimizing possible damage to normal tissues. Radionuclide therapy (RNT) is a therapeutic modality for cancer treatment which provides several advantages when compared to conventional therapeutic approaches[1]. RNT is based on the specific or preferential delivery of a radionuclide to a tumour, minimising possible side effects. The radiation is administered systemically or locally, differing from conventional (or external) radiotherapy, where the radiation is provided from outside the body[2] (Figure 5.1).

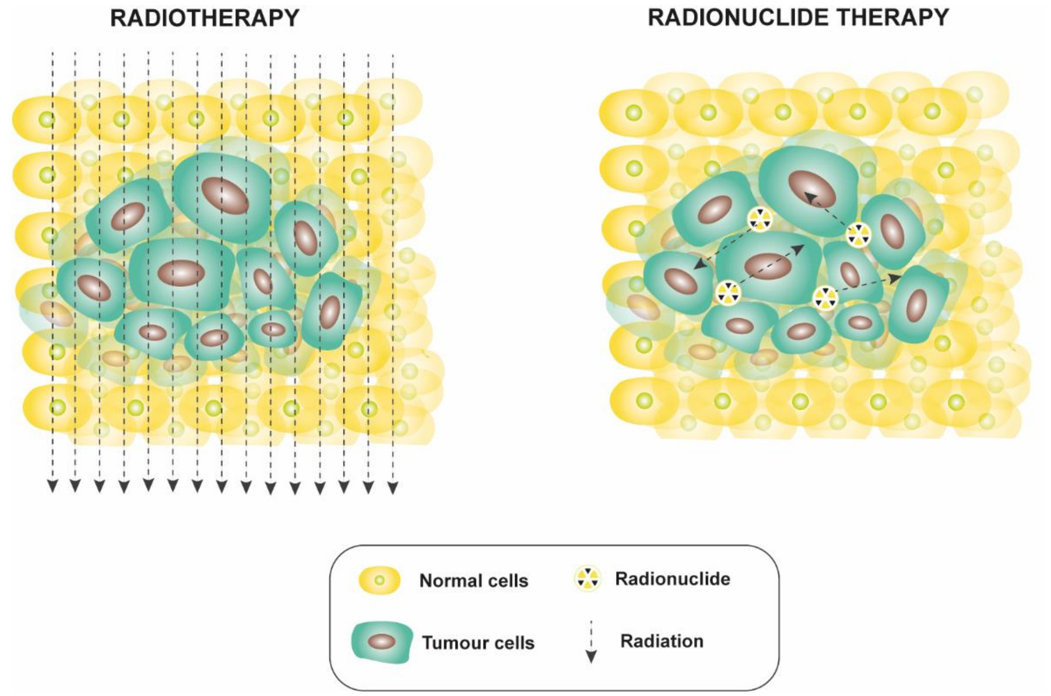

Figure 5.1. Tumour cell irradiation: conventional (external) radiotherapy versus radionuclide therapy.

RNT is based on the delivery of localized cytotoxic radiation in the tumour cells. Because of this, the ideal radionuclides for RNT are alpha (α) and beta (β) emitters. α-Particles are helium nuclei that are emitted from the nucleus of a radioisotope. They are positively charged and are emitted with a high energy than the emission energy of β-particles. Due to the high mass and positive charge, α-particles have a high linear energy transfer (LET) and a short range. Depending on the emitted energy, they can travel 0.05-0.1 mm in tissue[1, 2]. The damage caused by α-particles predominantly affects to the DNA double-strand, making the DNA repair mechanism ineffective[3]. The typical α-emitters used in RNT are astatine-211 (^{211}At), bismuth-212 (^{212}Bi), bismuth-213 (^{213}Bi), lead-212 (^{212}Pb), actinium-225 (^{225}Ac), radium-223 (^{223}Ra) and thorium-227 (^{227}Th) (table 5.1).

β-Particles are electrons emitted from the nucleus of a radioactive atom, and β emitters are the most frequently used radionuclides in RNT. Due to the lower mass (compared to α-particles) β-particles have lower LET and longer ranges in tissue (0.8 to 5 mm in tissue). The mechanism of action is the same described for α-particles, affecting to the double-strand breaks in DNA molecules. The most commonly used β emitters in RNT are samarium-153 (^{153}Sm), lutetium-177 (^{177}Lu), yttrium-90 (^{90}Y), and iodine-131 (^{131}I) (table 5.1), with ^{131}I being the most frequently used.

Table 5.1. Characteristics of the most commonly used alpha (α)- and beta (β)-particles in radionuclide therapy.

Radionuclide	Type of emission	Emission range (mm)	Half-life
^{211}At	α	0.05	7.2 h
^{212}Bi	α/ β^-	0.05	60 min
^{213}Bi	α	0.05-0.08	46 min
^{212}Pb	α/ β^-	0.1	10.6 h
^{225}Ac	α	0.05-0.08	10 days
^{223}Ra	α	0.05-0.08	11.4 days
^{227}Th	α	0.05-0.08	18.7 days
^{153}Sm	β^-	0.4	46.5 h
^{177}Lu	β^-	0.62	6.36 days
^{90}Y	β^-	5.30	64.1 h
^{131}I	β^-	0.8	8.01 days

RNT can be applied to any type of cancer, as the main criterion of this approach is the delivery of the radionuclide selectively or preferentially to tumour cells. Nevertheless, few examples can be found in the literature related to RNT in clinical or preclinical phases[1]. The prototypical example of RNT is ^{131}I to treat thyroid malignancies[4]. Iodine accumulates specifically in thyroid follicular cells and differentiates follicular thyroid cancer cells via sodium-iodine symporter[5]. Despite efficacious, the main limitation of this RNT is that it only works in a single type of cancer.

^{131}I is a routinely used radionuclide in therapy because of its physical properties. It has a long half-life (8.01 days), with two decay modes: β-particles providing therapeutic effect and gamma (γ) rays used for single-photon emission computed tomography (SPECT), making ^{131}I a potential theranostic agent. Nevertheless, some limitations need to be addressed before its application in other types of cancer, including poor targeting ability or non-homogenous distribution in tumour tissue[6].

With the advancement of the nanotechnology, nanoparticles (NPs) have provided new approaches to overcome the limitations of cancer treatment. In fact, radiolabelled NPs with ^{131}I have shown attractive potential to cancer diagnosis and therapy. Currently, the reported studies are based on releasing ^{131}I to cancer cells using small molecules[7], peptides[8], proteins[9] and antibodies[10] that are encapsulated or functionalized in the NPs. A promising approach could be the direct radiolabelling of the NP. In this context, polydopamine NP have been reported as a multimodal vehicle to deliver ^{131}I and the anticancer drug doxorubicin[11, 12], or palladium (Pd) nanosheets have been reported as promising platforms for photoacoustic (PA) imaging and RNT[13].

In Chapter 3, we demonstrated that urease nanomotors could be efficiently radiolabelled with the positron emitter iodine-124 (^{124}I; half-life = 4.2 days) with radiolabelling yield close to 70%[14]. Moreover, we showed that urease nanomotors administered in urea are more prone to accumulate in bladder tumour than their passive (non-self-propelled) counterparts (Chapter 4). Based on these encouraging results, and by replacing the positron emitter ^{124}I by the therapeutic radionuclide ^{131}I, we evaluate in this chapter the potential use of urease nanomotors as RNT agent in an orthotopic mouse model of bladder cancer.

With that aim, female mice were intravesically administered with a bladder carcinoma cell line (MB49). Then, animals were randomized in six groups according to tumour size, monitored using magnetic resonance imaging (MRI). ^{131}I-urease nanomotors and control treatments were administered within the bladder, and single photon emission computerised tomography (SPECT) imaging studies were conducted to confirm their capacity to accumulate in the tumour. Finally, therapeutic effect was monitored following tumour volume by means of post-treatment MRI (Figure 5.2). Our preliminary results suggest a positive impact of self-propelling capacity on therapeutic effect.

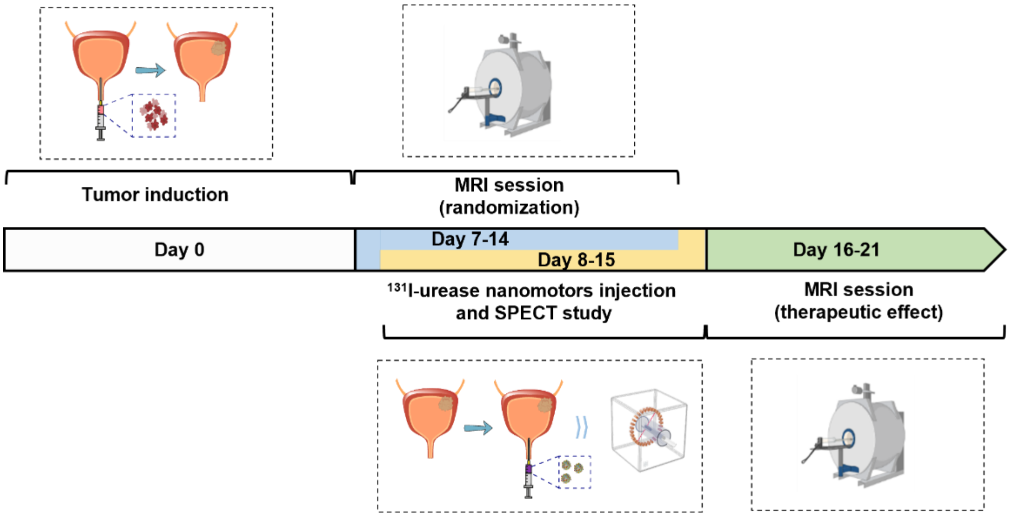

Figure 5.2. Schematic representation and timeline for the radionuclide therapy study to evaluate bladder tumour reduction *in vivo*.

5.2 Objectives

The specific objectives of this chapter are:

1. To radiolabel urease-powered nanomotors using ^{131}I.
2. To evaluate the therapeutic efficacy of ^{131}I-urease nanomotors in a mouse model of bladder cancer.

5.3 Materials and methods

5.3.1 General remarks

As mentioned in Chapters 3 and 4, urease nanomotors were synthetized by Prof. Samuel Sánchez's group at Institute for Bioengineering of Catalonia, IBEC (Barcelona, Spain). As in Chapter 4, the orthotopic animal model used was established with the help of Prof. Esther Julián (Autonomous University of Barcelona, UAB; Bellaterra, Spain).

5.3.2 Radiolabelling of urease nanomotors with ^{131}I (^{131}I-urease nanomotors)

The radioiodination of urease nanomotors was performed by incubation of the nanomotors with injectable [^{131}I]NaI solution (925 MBq/mL), purchased from GE HealthCare (Madrid, Spain). In brief, 400 µL of urease nanomotors solution (1 mg/mL) was centrifugated (13853 g, 5 min), re-suspended in 100 µL of phosphate buffered solution (PBS; 10 mM, pH 7.4), and incubated with 25 µL or 185 µL of injectable [^{131}I]NaI (*ca*. 42.55 and 277.5 MBq, respectively) depending on the final desired activity during 30 min. After incubation, the reaction mixture was purified by centrifugation (13853 g, 5 min). The resulting precipitate was washed three times with water (100 µL). The amount of radioactivity in the supernatant and the precipitate were determined in a dose calibrator (CPCRC-25R, Capintec Inc., NJ, USA), and both fractions were analysed by radio-thin layer chromatography (radio-TLC), using iTLC-SG chromatography paper (Agilent Technologies, CA, USA) and dichloromethane and methanol (2:1) as the stationary and mobile phases, respectively. TLC plates were analysed using TLC-reader (MiniGITA, Raytest, Straubenhardt, Germany).

5.3.3 Stability of ^{131}I-urease nanomotors

The stability of ^{131}I-urease nanomotors was determined using the following media: (i) 300 mM urea solution in water and (ii) ultrapure water. With that aim, 100 µL of ^{131}I-urease nanomotors were incubated with the corresponding solution (1 mL) for 1 h at room temperature. Then, nanomotors and supernatant were separated by centrifugation, collected, and the amount of radioactivity of each fraction was measured in a dose calibrator (CPCRC-25R, Capintec Inc., NJ, USA).

5.3.4 Animal model development

Mice were maintained and handled in accordance with the European Council Directive 2010/63/UE and internal guidelines. All experimental procedures were approved by the ethical committee at CIC biomaGUNE and the local authorities before conducting experimental work. The orthotopic murine model of bladder cancer was generated by intravesical administration of MB49 cells in C57BL/6JRj female mice (8 weeks old, Janvier, $N = 62$).

For tumour establishment, mice were anesthetized by inhalation of 3% isoflurane in pure O_2 and maintained by 1.0-1.5% isoflurane in 100% O_2. Then, the bladder was emptied by abdominal massage, and chemical lesions were induced on the bladder urothelium by intravesically instilling 50 µL of poly-L-lysine (Sigma-Aldrich) through a 24-gauge catheter for 15 min. Subsequently, bladder was again emptied and 100 µL of MB49 cells (10^5 cells) in DMEM high glucose media were instilled and incubated for 1 h. After that time, the catheter was removed, and the bladder was finally emptied by abdominal massage.

5.3.5 Tumour size monitored by MRI

Two MRI studies were performed in each mouse. The first one, used to randomise animals among groups and to have initial tumour volume values (before treatment), was carried out between days 7 and 14 after tumour inoculation; the second one, to evaluate therapeutic efficacy, was carried out between days 16 and 21 after tumour inoculation (after treatment). In both cases, a 7 (70/30 scanner) or 11.7 (117/16 scanner) Tesla Bruker Biospec (Bruker Biospin MRI GmbH, Ettlingen) was used. For the 7 Tesla scanner, a 112/086 QSN resonator was used for radiofrequency (RF) transmission and a rat brain surface coil for RF reception. For the 11 Tesla scanner, a superficial coil was used for the RF transmission and a rat heart surface coil for the RF reception.

Experimentally, animals were anesthetized with isoflurane (4% for induction and 1.5% for maintenance in a mixture 50% O_2/50% N_2) and placed on a MR compatible cradle. Body temperature and respiration rate were continuously monitored using an MR compatible monitoring device (model 1030 SA, Small Animal Instruments, Stony Brook, NY, USA), interfaced to a Small Rodent Air Heater System to maintain body temperature. After acquisition of scout images for reference, a Spin-Echo based Diffusion Weighted Imaging sequence (SE-DWI) was used to image the tumours, using the following imaging parameters: SE-DWI sequence, TE = 22.3 ms, TR = 2500 ms, N = 2 averages, 1 A0 image and on DW image acquired using diffusion gradients in (1, 0, 0) direction, with $\delta = 4.5$ ms and $\Delta = 10.6$ ms, giving a b value of 650 mm-2 s, a field of view = 16 x 16 mm2, image matrix = 160 x 160 points, 20 consecutive slices of 0.5 mm thickness (no gap, acquired in interleaved mode), and a bandwidth of 192.9 Hz/pixel.

To facilitate the visualization of the tumours, images were postprocessed with ImageJ software, dividing the set of images acquired with diffusion gradient (b = 650 mm^{-2} s) by the set of images acquired without diffusion gradients (b = 0 mm^{-2} s), and applying a Gaussian 3D filter (σx ,σy. σz = 0.7) to the resulting image. To determine tumour volume, VOIs were manually drawn on each slice covering the tumour area. For therapeutic study, the values of tumour volume were normalised to the mean value of initial tumour volume of each group.

5.3.6 Radionuclide therapy using ^{131}I-urease nanomotors

Between days 8 and 15 from tumour implantation, animals were divided into six groups (groups 1-6), while trying to keep average tumour volume homogeneous among groups (see table 5.2 for details). Each mouse received one of the following treatments: an intravesical injection of 100 µL of non-labelled urease nanomotors (0.36 mg/mL) administered in 300 mM urea solution in water (group 1, *N* = 9); or either low (1.85 MBq) or high dose (18.5 MBq) of ^{131}I-urease nanomotors (0.36 mg/mL) using either ultrapure water (group 2, *N* = 9; group 4, *N* = 7, respectively) or 300 mM urea solution in water (group 3, *N* = 9; group 5, *N* = 7, respectively). Additionally, tumour-bearing animals not treated with nanomotors were used as extra control (group 6, control, *N* = 9).

The experimental procedure performed was the following: Animals were induced with anaesthesia (5% isoflurane in pure O_2) and positioned in supine position. The bladder was emptied by massaging the abdominal region. Immediately after, the corresponding compound (see table 5.2) was instilled in the bladder through a 24-gauge catheter, using the appropriate vehicle according to the experimental group (water or 300 mM urea solution in water). The solution containing the corresponding specie was allowed to stay in the bladder for 1 h. After that time, the catheter was removed, the bladder was emptied by abdominal massage, and mice were recovered from the anaesthesia in their cages. After 24 h post-treatment, the sawdust of animal cages was replaced to remove radioactive contamination.

5.3.7 SPECT-CT imaging *in vivo*

SPECT-CT imaging studies were conducted in MOLECUBES γ and X-CUBE scanners (MOLECUBES, Gent, Belgium) at t = 3 h post-administration of those animals administered with low and high dose of ^{131}I-urease nanomotors instilled either with ultrapure water (groups 2 and 4, respectively) or 300 mM urea solution in water (groups 3 and 5, respectively). With that aim, animals were re-anaesthetized, bladders were emptied by abdominal massage, and 10-min static SPECT images were acquired. The field of view was selected to cover the lower part of the abdominal region, and a phantom with a known concentration of radioactivity was introduced in the field of view. SPECT imaging was followed by CT acquisitions.

SPECT images were reconstructed using 3D OSEM reconstruction algorithm. SPECT-CT images of the same mouse were co-registered and analysed using PMOD image processing tool. To get the relative concentration of radioactivity, a volume of interest (VOIs) was manually drawn on the bladder on the CT images and translated to the SPECT images. A second VOI was drawn on the phantom with known concentration of radioactivity. The relative quantification of the concentration of radioactivity in both VOIs enabled the determination of the absolute concentration of radioactivity in the VOI positioned in the bladder. The resulting values were normalised to the mean value of initial tumour volume of each group as determined by MRI.

5.3.8 Statistical analysis

For SPECT imaging studies, values of percentage of injected dose per volume of tumour (% ID/cm^3) within each group (low dose or high dose) were compared using unpaired *t*-test. For therapeutic efficacy studies, values of normalised tumour volume for each group were compared using two-way ANOVA. Differences between groups were determined using Turkey's multiple comparisons test. Differences were concluded significant for *p* values < 0.05. Statistical analyses were performed with GraphPad Prism version 8.0.

5.4 Results and discussion

5.4.1 Radiolabelling of nanomotors using ^{131}I

One of the most common radioisotopes for applying RNT is ^{131}I. It remains the radionuclide of choice for therapy because of its physical properties: long half-life (8.01 days) and emitted β-particles (maximum energy of 610 KeV) with penetration range of 0.8 mm in tissue[15]. In chapter 3, we demonstrated an efficient radiolabelling strategy to label urease nanomotors using ^{124}I which could be absorbed on the gold NPs (AuNPs) present on their surface. Therefore, we hypothesized that this methodology could be directly applied to radiolabel the nanomotors using ^{131}I (Figure 5.3a). Our first trial was to apply exactly the same methodology described for ^{124}I-urease nanomotors[14].With that aim, injectable [^{131}I]NaI was incubated with urease nanomotors (200 µg) at room temperature, and the reaction mixture was analysed at different time points (10 and 30 min) by radio-TLC (Figure 5.3b) to assess radiochemical conversion values. The obtained chromatograms showed a lower conversion rate than that obtained for ^{124}I. After purification by centrifugation, radiochemical yield was only 28.5 ± 1.5%, significantly lower than that obtained for ^{124}I, and inferior to previous values reported in the literature in similar nanosystems[16-18]. The abnormal low yield might be a consequence of the composition of the labelling agent. Indeed, [^{131}I]NaI typically used to radiolabel molecules is purchased as a solution in 0.1 M sodium hydroxide (NaOH). Here, and due to availability issues, we performed the radiolabelling using injectable [^{131}I]NaI solution, whose composition contains different sodium salts and a high concentration of ions (e.g. chloride) which may interfere with the labelling process. In view of the results, we decided to double the quantity of nanomotors and perform the incubation with [^{131}I]NaI at room temperature over 30 min (Figure 5.3c). Higher radiochemical conversion values, closer to those previously observed for ^{124}I, were obtained. After purification by centrifugation, ^{131}I-urease nanomotors with super radiochemical purity (≥99%) could be obtained, as determined by radio-TLC (Figure 5.3c). Radiochemical yield was 73 ± 10% similar to that described in Chapter 3[14].

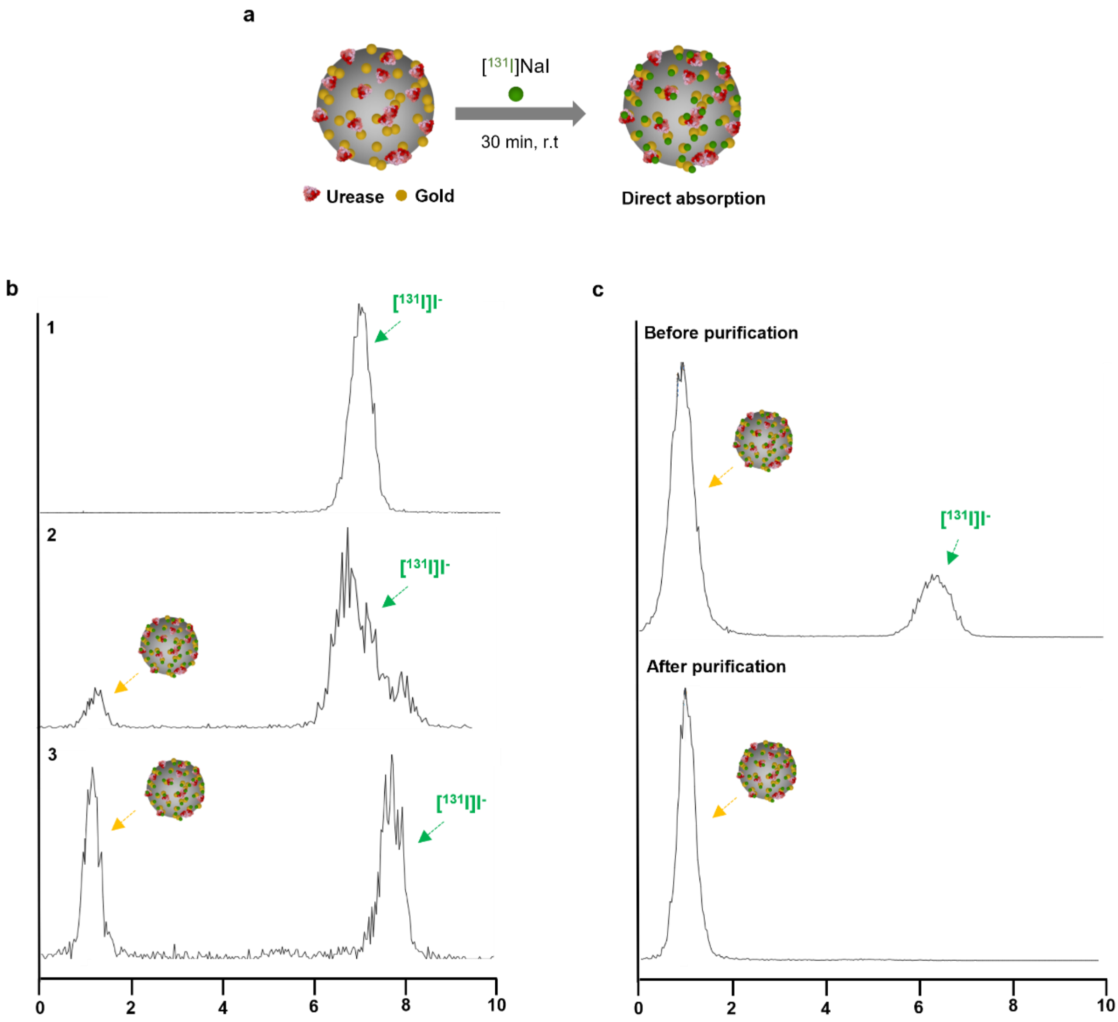

Figure 5.3. a) Schematic representation of radiolabelling of urease nanomotors by direct absorption of [^{131}I]NaI. b) Representative chromatogram of [^{131}I]NaI (1) and of reaction mixtures (using 200 µg of urease nanomotors) obtained at different reaction times: 10 min (2) and 30 min (3) c) Representative radio-TLC chromatograms of ^{131}I-urease nanomotors (400 µg) before (top) and after (below) purification.

Before moving into radiotherapy, studies to assess the radiochemical stability of the labelled nanomotors were performed in water and 300 mM urea solution in water. With that aim, ^{131}I-urease nanomotors were incubated during 1 h with both solutions. Radio-TLC analyses showed radiochemical purity values above 95% in both cases, confirming the stability of the label.

5.4.2 Radioiodination therapy in bladder cancer

Bladder cancer is the most common malignancy of the urinary tract[19]. As previously mentioned, bladder cancer is diagnosed in half a million patients each year worldwide[20]. Depending on the location of the tumour within the bladder, this malignancy can be classified as non-muscle invasive bladder cancer (NMIBC), or muscle invasive bladder cancer (MIBC). For NMIBC cases, transurethral resection of the bladder is the main therapy, followed by intravesical instillations of immunotherapeutic (Mycobacterium bovis bacillus Calmette–Guérin, BCG) and/or chemotherapeutic (mitomycin C, MMC) agents to prevent possible recurrence and progression, whereas radical removal of the bladder is performed in those patients with MIBC[21]. The implemented treatments are not highly effective as recurrence appears in 30-70% of the cases within 5 years[22]. New therapeutic strategies need to be developed to overcome limitations of classical approaches, these mainly related to the low permeability of the urothelium or drug dilution due to the continuous generation of urine.

In the previous chapter, we demonstrated that urease-powered nanomotors accumulate and penetrate further in bladder tissue when administered in 300 mM urea solution in water compared to passive nanomotors, due to their motile capacity. These findings position urease-powered nanomotors as promising drug delivery systems for bladder cancer therapy. Here, we decided to combine the tumour accumulation properties of urease nanomotors administered in urea with the therapeutic effect of ^{131}I. Our study constitutes, to the best of our knowledge, the first example of RNT in an orthotopic model of bladder cancer.

For this study, we used the same animal model described in Chapter 4, where tumour formation was achieved by pre-treatment with poly-L-lysine, followed by intravesical instillation of MB49 tumour cells. To distribute the animals among the different experimental groups for subsequent RNT, MRI sessions were performed to assess tumour volume, following the same protocol employed in Chapter 4.

In total 62 animals were inoculated with MB49 cell line. From them, 50 animals were selected to undergo the therapy study, corresponding to animals that developed tumours with a volume > 1 mm^3. As previously stated, this tumour growing rate is within the expected efficiency of MB49 cell line (ratio of 80-100%)[23, 24]. Animals were randomly classified in six groups as function of their tumour volume obtained by MRI, always ensuring a uniform distribution between the groups.

Five different scenarios were defined to evaluate the efficacy of urease-powered nanomotors to apply RNT. The selection of these five experimental groups was made by trying to answer three questions: (i) Can urease nanomotors administered in urea, due to their self-propulsion, modify tumour progression? (ii) At what dose does ^{131}I have therapeutic effects? and (iii) Does the difference in tumour accumulation between active and passive nanomotors remain the same regardless of the dose of ^{131}I? With that aim, animals were intravesically administered with: (1) non-labelled urease nanomotors using 300 mM urea solution in water as vehicle; (2) and (3) ^{131}I-urease nanomotors administered in a low dose (LD; 1.85 MBq) using either water or 300 mM urea solution in water as vehicle, respectively; (4) and (5) ^{131}I-urease nanomotors administered in a high dose (HD; 18.5 MBq) using either water or 300 mM urea solution in water as vehicle, respectively. One additional control group was included (6), comprising tumour-bearing animals non treated with nanomotors (Table 5.2).

Table 5.2. Summary of the different experimental scenarios performed in the therapy study.

Group	*N*	Compound	Activity (MBq)
1	9	urease nanomotors in urea	0
2	9	^{131}I-urease nanomotors (LD) in water	1.85
3	9	^{131}I-urease nanomotors (LD) in urea	1.85
4	7	^{131}I-urease nanomotors (HD) in water	18.5
5	7	^{131}I-urease nanomotors (HD) in urea	18.5
6	9	Non treated	0

N: number of animals in each group; LD: low dose; HD: high dose

To apply the RNT, irrespective of the study group, all animals with the empty bladder received an intravesical injection of the corresponding compound and vehicle. The solution containing the nanomotors was incubated during 1 h within the bladder, following the same protocol stablished to evaluate tumour accumulation with ^{18}F-nanomotors. After that time, bladders were emptied again, and animals recovered form anaesthesia in their cages without any apparent side effect due to the internal irradiation.

5.4.3 Tumour accumulation determined by SPECT imaging

Labelling NPs with ^{131}I can be used as dual-mode platform for SPECT imaging and RNT. ^{131}I decays with 90% β (610 KeV) and 82% γ (364 KeV) emissions (Figure 5.4), which means that in principle it enables *in vivo* imaging and therapeutic intervention. In spite of this, ^{131}I is typically used only as a therapeutic agent, because its high γ energy is sub-optimal for SPECT cameras (usually resulting in low sensitivity and resolution). In fact, in RNT of thyroid malignancies is accompanied by pre- and post-treatment evaluation using iodine-123 (^{123}I), which is a pure γ emitter with lower γ emissions (159 KeV)[25]. In spite of this, we decided to use the imaging properties of ^{131}I to get an estimation of tumour accumulation of ^{131}I-urease nanomotors (both doses) using SPECT imaging. SPECT is a high-sensitive and non-invasive nuclear imaging technique that enables to detect sub-pharmacological amounts of radiolabelled compounds at the whole-body level. Furthermore, this technique is fully translational to clinics together with CT to obtain anatomical information. SPECT acquisitions were performed 3 h after administration and immediately after bladder evacuation, followed by CT scans. As SPECT cameras detect γ emissions from radionuclides (^{131}I in this case), only animals administered with ^{131}I-urease nanomotors in both doses and media were scanned.

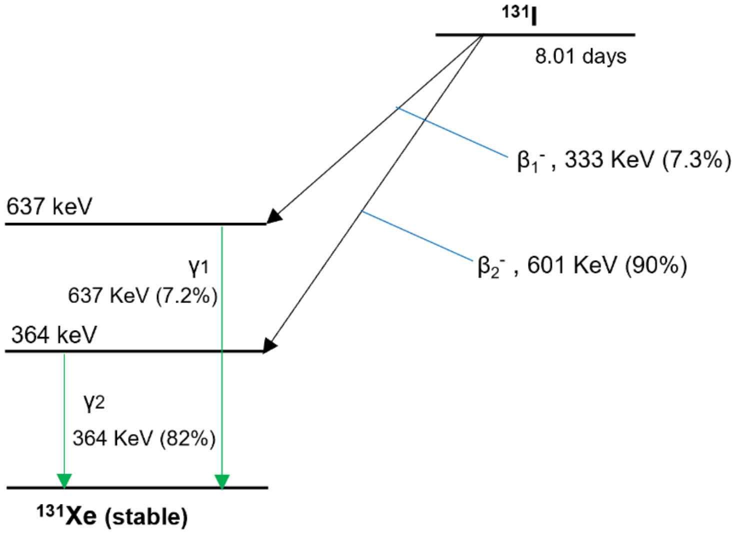

Figure 5.4. Simplified decay scheme of ^{131}I radionuclide. Adapted from Lee, U.[26]

SPECT images showed the presence of radioactive signal within the bladder, corresponding to the location of the tumour according to MRI images (Figure 5.5, left). Comparing the low dose groups (2 and 3), visual inspection of the images revealed a higher radioactive signal when ^{131}I-urease nanomotors were administered using 300 mM urea solution in water as vehicle (group 3; Figure 5.5a). Contrarily, differences between groups could not be detected by visual inspection for ^{131}I-urease nanomotors administered in HD using either water or 300 mM urea solution in water as vehicle (Figure 5.5b).

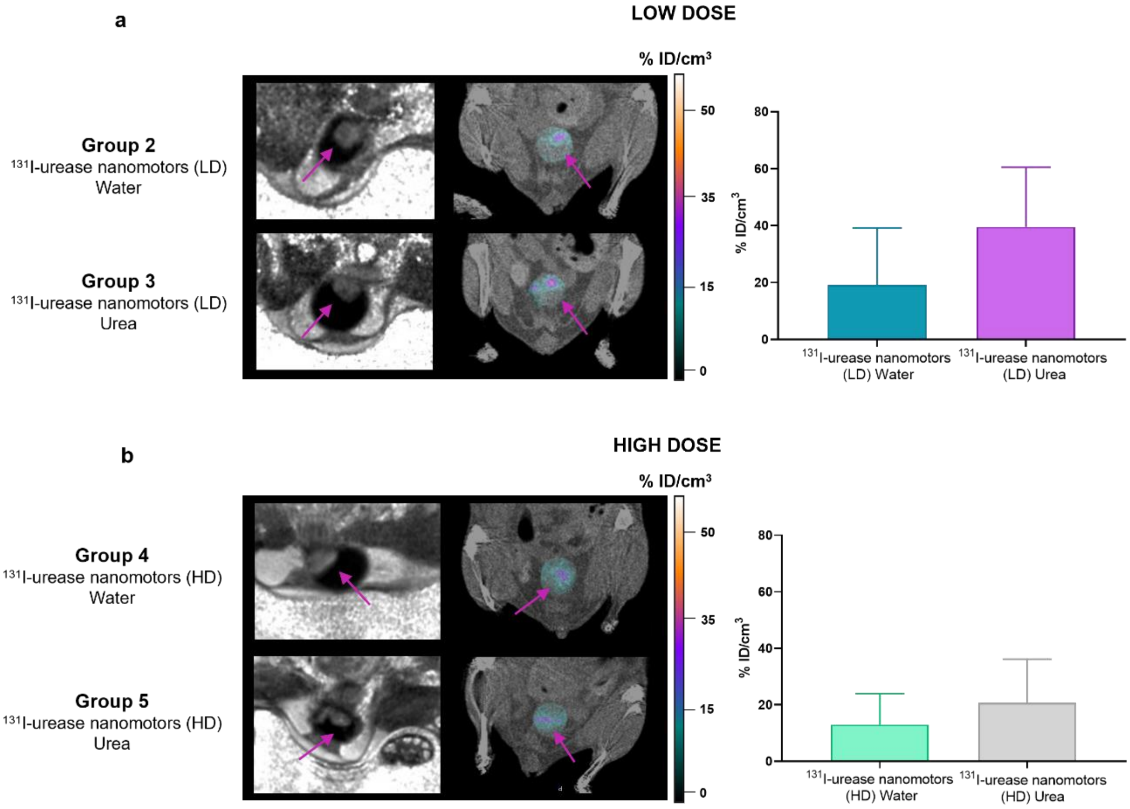

Figure 5.5. Representative MRI and SPECT-CT images and semiquantitative accumulation of radioactivity in the tumour normalised to the mean of tumour volume obtained by MRI, for animals corresponding to group 2 (a), 3 (a), 4 (b), and 5 (b). For SPECT images slices have been corregistered with the corresponding CT slice for anatomical localization of the radioactive signal. Group 2: ^{131}I-urease nanomotors administered with low dose of ^{131}I and water as vehicle; group 3: ^{131}I-urease nanomotors administered with low dose of ^{131}I and 300 mM urea solution in water as vehicle; group 4: ^{131}I-urease nanomotors administered with high dose of ^{131}I and water as vehicle; and group 5: ^{131}I-urease nanomotors administered with high dose of ^{131}I and 300 mM urea solution in water solution as vehicle.

Semiquantitative analysis was performed to obtain the amount of radioactivity accumulated in the tumour in all scenarios. Values were expressed as percentage of injected dose per volume of tumour (% ID/cm^3, Figure 5.5, right), the latter normalised to the mean value of tumour volume of each group. Values obtained confirm an increased uptake in the tumour for group 3 (*ca*. 40 % ID/cm^3) compared to group 2 (*ca*. 20 % ID/cm^3), confirming the positive effect of active motion in tumour accumulation. Nevertheless, the obtained results were statistically equivalent, although p values were close to 0.05 ($p = 0.0654$). No significant difference was observed between groups 4 and 5, whose tumour accumulation values were *ca*. 13 and 20 % ID/cm^3, respectively ($p = 0.3640$). Despite the lack of significant differences, also in this case the results suggest that there is an effect of the vehicle in tumour accumulation, although the variability within the groups is too large to result in statistical significance.

5.4.4 Evaluation of the therapeutic effect

After treatment, patient follow-up is an important parameter in bladder cancer because of the high incidence of recurrence and progression[27]. In clinics, the gold standard protocol for post-treatment monitoring is cystoscopy together with cytology. Nevertheless, these invasive techniques can cause complications, including pain, bleeding, or urinary infections. Non-invasive techniques, such as MRI can be a good alternative for local recurrence detection[28]. This high-resolution and soft-tissue contrast imaging technique can generate three-dimensional anatomical images that can distinguish between tumour mass and the bladder wall.

Normally, therapeutic studies on subcutaneous tumour models are evaluated by weekly monitoring tumour volume using a caliper[29]. Therefore, tumour growth differences between study groups can be easily identified. However, working with orthotopic models, this effect is more difficult to confirm. The most common strategy is the evaluation of weight loss together with survival study of the animals[30]. At the end of the study, animals are sacrificed, tumour removed and analysed by *ex vivo* tools. However, this methodology requires sacrifice of large numbers of experimental animals. As alternative strategy, one can use *in vivo* imaging techniques, which allow visualisation of tumour location, the expression and activity of different biomolecules, cells, and biological processes and/or the tumour response to therapeutic drugs[31]. Among all, we decided to use MRI to follow *in vivo* tumour volume one week after treatment. As we had previously demonstrated in Chapter 4, MRI is good technique to visualize tumour location within the bladder since 95% of the composition of the urine is water. The resulting MRI images show the presence of the tumour as a grey mass while the bladder is black.

Before treatment, in all groups, MRI images showed the presence of tumour in the upper part of the bladder (Figure 5.6a; before treatment). Visual inspection of the images obtained post-treatment revealed an effective tumour reduction for ^{131}I-urease nanomotors administered with a HD of ^{131}I (18.5 MBq) irrespective of the vehicle used (Figure 5.6a; groups 4 and 5), suggesting a non-dependent therapeutic effect of ^{131}I with the nanomotors' motion in the presence of urea. Interestingly, MRI images obtained for ^{131}I-urease nanomotors with LD of ^{131}I (1.85 MBq) revealed a visual difference in tumour growth (Figure 5.6a; groups 2 and 3), demonstrating a larger tumour when water was used as vehicle, while when urea was used, tumour size remained constant (thus suggesting a halt in tumour growth).

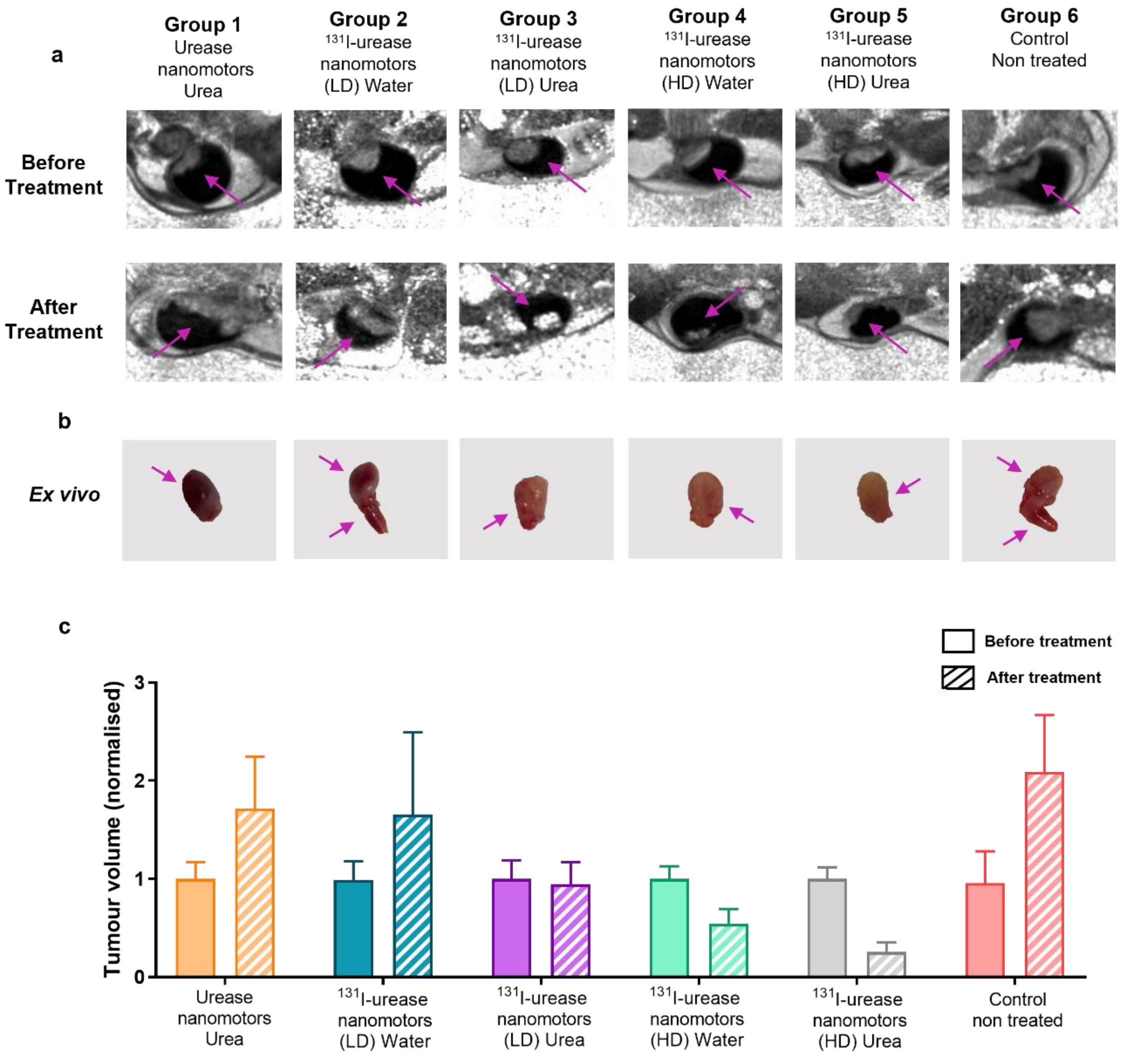

Figure 5.6. a) Representative MRI images of animals corresponding to control and groups 1-5 before and after radionuclide treatment. The position of the tumour is indicated with a pink narrow. b) Representative photo images of bladder tumours corresponding to each group (1-6) at the end of the therapy study. The position of the tumour is indicated with a pink narrow. c) Tumour growth values before and after radionuclide treatment. Tumour volume values were normalised to the mean of the initial tumour values of each group (*N* = 9 per group, except groups 4 and 5 with *N* = 7). Control: tumour-bearing animals in absence of nanomotors; group 1: urease nanomotors administered with 300 mM urea solution; group 2: ^{131}I-urease nanomotors administered with low dose of ^{131}I and water as vehicle; group 3: ^{131}I-urease nanomotors administered with low dose of ^{131}I and 300 mM urea solution in water as vehicle; group 4: ^{131}I-urease nanomotors administered with high dose of ^{131}I and water as vehicle; and group 5: ^{131}I-urease nanomotors administered with high dose of ^{131}I and 300 mM urea solution in water solution as vehicle.

To corroborate the differences observed, MRI images were quantified using Image J software and the resulting tumour values were normalised to the mean initial tumour value of each group (before treatment) to obtain normalised tumour volume (NTV) values (Figure 5.6c). As expected, untreated tumour-bearing animals showed an increase in tumour size over time (group 6, control; *ca*. 2 NTV). A similar trend was obtained for animals instilled with non-labelled urease nanomotors using 300 mM urea solution in water as vehicle (group 1; *ca*. 1.8 NTV), confirming that urease nanomotors do not have therapeutic properties by themselves. For the scenarios where ^{131}I-urease nanomotors were administered with LD of ^{131}I (groups 2 and 3), different trends can be appreciated among groups. While group 2 had a similar behaviour to that observed for the groups 1 and 6 (control) animals, with an increase in tumour size over time (*ca*. 1.8 NTV), group 3 showed tumours with invariable size or with slightly descending trend (*ca*. 0.95 NTV), suggesting a positive impact of active motion on tumour progression. At high doses, ^{131}I-urease nanomotors in both media (water and urea) resulted in a reduction in tumour size after treatment (groups 4 and 5; *ca*. 0.54 and 0.27 NTV, respectively). After the MRI session, animals were sacrificed, and bladders excised to corroborate the results obtained (Figure 5.6b). Tumours were clearly visible in those bladders corresponding to groups 1,2, and 6, which tumours increased over time as determined by MRI. While small tumours within the bladder were observed for groups 3,4, and 5. These results support *in vivo* MRI with respect to tumour growth progression. Nevertheless, histological analysis will be performed in the future to corroborate what has been observed.

Overall, these finding suggest that a LD doses of ^{131}I (1.85 MBq), the self-propulsion properties of urease nanomotors in presence of urea have a net effect on bladder tumour volume reduction, probably due to a higher tumour accumulation. This can be beneficial as administering lower doses means less radiation, and therefore less side effects. Furthermore, the bladder is located close to reproductive organs, which influences in the dose to be administered. On the other hand, using a HD of ^{131}I, both active (administered in urea) and passive (administered in water) urease nanomotors can have a therapeutic effect. It is possible that the contact with this high dose (18.5 MBq) provokes DNA damage in tumour cells. This study is an initial proof-of-concept to evaluate the usefulness of urease nanomotors as carriers of ^{131}I. For the moment, differences among groups are not significant, and because of that only trends can be discussed. Future studies with higher number of animals will shed light on the usefulness of RNT to treat bladder cancer.

5.5 Summary and conclusions

In this chapter, urease nanomotors were radiolabelled using ^{131}I following the same methodology previously described for ^{124}I (Chapter 3) with minor modifications. The orthotopic model of bladder cancer described in Chapter 4 was used to evaluate the therapeutic capacity of ^{131}I-urease nanomotors administered in urea. For this, MRI technique was used both to randomise animals among experimental groups and to evaluate therapeutic efficacy. SPECT imaging was performed to corroborate tumour accumulation after administration of ^{131}I-urease nanomotors.

The work presented in this chapter shows an initial proof-of concept. It gathers results obtained after the intravesical administration of ^{131}I-urease nanomotors under different experimental conditions in a mouse model of bladder cancer. The results obtained with lower dose of ^{131}I-urease nanomotors administered in urea suggest a positive impact of self-propelling capacity on therapeutic effect. Nevertheless, at higher dose of ^{131}I-urease nanomotors, non-self-propelled nanomotors already show a therapeutic effect. Altogether, these results suggest that self-propelling capacity can be used to decrease radioactive dose while preserving therapeutic efficacy. Still, experiments involving more animals are required in the future to identify potential therapeutic use of radiolabelled nanomotors.

5.6 References

(1) Sgouros, G.; Bodei, L.; McDevitt, M. R.; Nedrow, J. R., Radiopharmaceutical therapy in cancer: clinical advances and challenges. *Nat Rev Drug Discov* **2020,** *19* (9), 589-608.

(2) St James, S.; Bednarz, B.; Benedict, S.; Buchsbaum, J. C.; Dewaraja, Y.; Frey, E.; Hobbs, R.; Grudzinski, J.; Roncali, E.; Sgouros, G.; Capala, J.; Xiao, Y., Current Status of Radiopharmaceutical Therapy. *Int J Radiat Oncol Biol Phys* **2021,** *109* (4), 891-901.

(3) Sgouros, G.; Roeske, J. C.; McDevitt, M. R.; Palm, S.; Allen, B. J.; Fisher, D. R.; Brill, A. B.; Song, H.; Howell, R. W.; Akabani, G.; Committee, S. M.; Bolch, W. E.; Brill, A. B.; Fisher, D. R.; Howell, R. W.; Meredith, R. F.; Sgouros, G.; Wessels, B. W.; Zanzonico, P. B., Radiobiology and dosimetry of alpha-particle emitters for targeted radionuclide therapy. *J Nucl Med* **2010,** *51* (2), 311-28.

(4) Varghese, J.; Rohren, E.; Guofan, X., Radioiodine Imaging and Treatment in Thyroid Disorders. *Neuroimaging Clinics of North America* **2021,** *31* (3), 337-344.

(5) Llop, J.; Lammers, T., Nanoparticles for Cancer Diagnosis, Radionuclide Therapy and Theranostics. *ACS Nano* **2021,** *15* (11), 16974–16981.

(6) Dash, A.; Knapp Ff Fau - Pillai, M. R. A.; Pillai, M. R., Targeted radionuclide therapy-an overview. *Curr. Radiopharm.* **2013,** *6* (3), 152-80.

(7) Huang, P.; Zhang, Y.; Wang, W.; Zhou, J.; Sun, Y.; Liu, J.; Kong, D.; Liu, J.; Dong, A., Co-delivery of doxorubicin and (131)I by thermosensitive micellar-hydrogel for enhanced in situ synergetic chemoradiotherapy. *J Control Release* **2015,** *220* (Pt A), 456-464.

(8) Sun, N.; Zhao, L.; Zhu, J.; Li, Y.; Song, N.; Xing, Y.; Qiao, W.; Huang, H.; Zhao, J., (131)I-labeled polyethylenimine-entrapped gold nanoparticles for targeted tumor SPECT/CT imaging and radionuclide therapy. *Int J Nanomedicine* **2019,** *14*, 4367-4381.

(9) Liu, K.; Zheng, D.; Zhao, J.; Tao, Y.; Wang, Y.; He, J.; Lei, J.; Xi, X., pH-Sensitive nanogels based on the electrostatic self-assembly of radionuclide (131)I labeled albumin and carboxymethyl cellulose for synergistic combined chemo-radioisotope therapy of cancer. *J Mater Chem B* **2018,** *6* (29), 4738-4746.

(10) Li, W.; Liu, Z.; Li, C.; Li, N.; Fang, L.; Chang, J.; Tan, J., Radionuclide therapy using (1)(3)(1)I-labeled anti-epidermal growth factor receptor-targeted nanoparticles suppresses cancer cell growth caused by EGFR overexpression. *J Cancer Res Clin Oncol* **2016,** *142* (3), 619-32.

(11) Li, Z.; Wang, B.; Zhang, Z.; Wang, B.; Xu, Q.; Mao, W.; Tian, J.; Yang, K.; Wang, F., Radionuclide Imaging-Guided Chemo-Radioisotope Synergistic Therapy Using a (131)I-Labeled Polydopamine Multifunctional Nanocarrier. *Mol Ther* **2018,** *26* (5), 1385-1393.

(12) Zhong, X.; Yang, K.; Dong, Z.; Yi, X.; Wang, Y.; Ge, C.; Zhao, Y.; Liu, Z., Polydopamine as a Biocompatible Multifunctional Nanocarrier for Combined Radioisotope Therapy and Chemotherapy of Cancer. *Advanced Functional Materials* **2015,** *25* (47), 7327-7336.

(13) Chen, M.; Guo, Z.; Chen, Q.; Wei, J.; Li, J.; Shi, C.; Xu, D.; Zhou, D.; Zhang, X.; Zheng, N., Pd nanosheets with their surface coordinated by radioactive iodide as a high-performance theranostic nanoagent for orthotopic hepatocellular carcinoma imaging and cancer therapy. *Chem Sci* **2018,** *9* (18), 4268-4274.

(14) Hortelao, A. C.; Simó, C.; Guix, M.; Guallar-Garrido, S.; Julián, E.; Vilela, D.; Rejc, L.; Ramos-Cabrer, P.; Cossío, U.; Gómez-Vallejo, V.; Patiño, T.; Llop, J.; Sánchez, S., Swarming behavior and in vivo monitoring of enzymatic nanomotors within the bladder. *Science Robotics* **2021,** *6* (52), eabd2823.

(15) Mumtaz, M.; Lin Ls Fau - Hui, K. C.; Hui Kc Fau - Mohd Khir, A. S.; Mohd Khir, A. S., Radioiodine I-131 for the therapy of graves' disease. *Malays J. Med. Sci.* **2009,** *16* (1), 25-33.

(16) Eskandari, N.; Yavari, K.; Outokesh, M.; Sadjadi, S.; Ahmadi, S. J., Iodine-131 radiolabeling of poly ethylene glycol-coated gold nanorods for in vivo imaging. *J Labelled Comp Radiopharm* **2013,** *56* (1), 12-6.

(17) Pulagam, K. R.; Gona, K. B.; Gomez-Vallejo, V.; Meijer, J.; Zilberfain, C.; Estrela-Lopis, I.; Baz, Z.; Cossio, U.; Llop, J., Gold Nanoparticles as Boron Carriers for Boron Neutron Capture Therapy: Synthesis, Radiolabelling and In vivo Evaluation. *Molecules* **2019,** *24* (19), 3609.

(18) Vilela, D.; Cossio, U.; Parmar, J.; Martinez-Villacorta, A. M.; Gomez-Vallejo, V.; Llop, J.; Sanchez, S., Medical Imaging for the Tracking of Micromotors. *ACS Nano* **2018,** *12* (2), 1220-1227.

(19) Barani, M.; Hosseinikhah, S. M.; Rahdar, A.; Farhoudi, L.; Arshad, R.; Cucchiarini, M.; Pandey, S., Nanotechnology in Bladder Cancer: Diagnosis and Treatment. *Cancers (Basel)* **2021,** *13* (9), 2214.

(20) Richters, A.; Aben, K. K. H.; Kiemeney, L., The global burden of urinary bladder cancer: an update. *World J Urol* **2020,** *38* (8), 1895-1904.

(21) Dobruch, J.; Oszczudlowski, M., Bladder Cancer: Current Challenges and Future Directions. *Medicina (Kaunas)* **2021,** *57* (8), 749.

(22) Antoni, S.; Ferlay, J.; Soerjomataram, I.; Znaor, A.; Jemal, A.; Bray, F., Bladder Cancer Incidence and Mortality: A Global Overview and Recent Trends. *Eur Urol* **2017,** *71* (1), 96-108.

(23) Chan, E.; Patel, A.; Heston, W.; Larchian, W., Mouse orthotopic models for bladder cancer research. *BJU Int* **2009,** *104* (9), 1286-91.

(24) Chan, E. S.; Patel, A. R.; Smith, A. K.; Klein, J. B.; Thomas, A. A.; Heston, W. D.; Larchian, W. A., Optimizing orthotopic bladder tumor implantation in a syngeneic mouse model. *J Urol* **2009,** *182* (6), 2926-31.

(25) Mandel, S. J.; Shankar Lk Fau - Benard, F.; Benard F Fau - Yamamoto, A.; Yamamoto A Fau - Alavi, A.; Alavi, A., Superiority of iodine-123 compared with iodine-131 scanning for thyroid remnants in patients with differentiated thyroid cancer. *Clin. Nucl. Med.* **2001,** *26* (1), 6-9.

(26) Lee, U.; Kim, M. J.; Kim, H. R., Radioactive iodine analysis in environmental samples around nuclear facilities and sewage treatment plants. *Nuclear Engineering and Technology* **2018,** *50* (8), 1355-1363.

(27) Soukup, V.; Babjuk, M.; Bellmunt, J.; Dalbagni, G.; Giannarini, G.; Hakenberg, O. W.; Herr, H.; Lechevallier, E.; Ribal, M. J., Follow-up after surgical treatment of bladder cancer: a critical analysis of the literature. *Eur Urol* **2012,** *62* (2), 290-302.

(28) Sim, K. C.; Sung, D. J., Role of magnetic resonance imaging in tumor staging and follow-up for bladder cancer. *Transl Androl Urol* **2020,** *9* (6), 2890-2907.

(29) Su, W.; Chen, C.; Wang, T.; Li, X.; Liu, Y.; Wang, H.; Zhao, S.; Zuo, C.; Sun, G.; Bu, W., Radionuclide-labeled gold nanoparticles for nuclei-targeting internal radio-immunity therapy. *Materials Horizons* **2020,** *7* (4), 1115-1125.

(30) Noguera-Ortega, E.; Secanella-Fandos, S.; Erana, H.; Gasion, J.; Rabanal, R. M.; Luquin, M.; Torrents, E.; Julian, E., Nonpathogenic Mycobacterium brumae Inhibits Bladder Cancer Growth In Vitro, Ex Vivo, and In Vivo. *Eur Urol Focus* **2016,** *2* (1), 67-76.

(31) Condeelis, J.; Weissleder, R., In vivo imaging in cancer. *Cold Spring Harb Perspect Biol* **2010,** *2* (12), a003848.

CHAPTER 6

GENERAL CONCLUSIONS

Chapter 6: General conclusions

1. Urease nanomotors can be efficiently radiolabelled with fluorine-18 (^{18}F), by reaction between the free amino groups present on the enzyme at the surface of the nanomotors and a pre-labelled prosthetic group, and iodine-124 (^{124}I), *via* direct absorption of the radionuclide on the gold nanoparticles present at the surface of nanomotors.

2. Nuclear imaging techniques, particularly Positron Emission Tomography (PET), are appropriate to investigate the collective behaviour of radiolabelled nanomotors both *in vitro* and *in vivo*. *In vivo*, the motile properties of the nanomotors lead to the formation of a homogeneous phase in the bladder, after intravesical administration in healthy mice.

3. Magnetic Resonance Imaging (MRI) techniques enable the longitudinal monitoring of tumour volume in a mouse model of bladder cancer.

4. ^{18}F-urease nanomotors intravesically administered using urea as the vehicle show an increased accumulation in the tumour (5-fold increase) and enhanced penetration capacity in a mouse model of bladder cancer.

5. Urease nanomotors can be efficiently radiolabelled using iodine-131 (^{131}I) *via* direct absorption of ^{131}I on the gold nanoparticles at the surface of the nanomotors.

6. Preliminary studies of radionuclide therapy in an orthotopic model of bladder cancer using ^{131}I-urease nanomotors, suggest a positive impact of active motile properties on therapeutic effect.

ACKNOWLEDGEMENTS

Acknowledgements

En primer lugar, quiero agradecer al Prof. Manuel Martín Lomas, al Prof. Luis Liz-Marzán y a la Prof. Aitziber López Cortajarena, anteriores y actual directora científica de CIC biomaGUNE por darme la oportunidad de desarrollar el trabajo experimental de esta tesis en las instalaciones del centro. Ha sido un placer poder trabajar en un ambiente tan multidisciplinar y multicultural, además de aprender una gran variedad de técnicas.

Mi más sincero agradecimiento a mi director de tesis Dr. Jordi Llop, no solo por darme la oportunidad de realizar esta tesis doctoral en su grupo, sino por enseñarme tantísimo sobre el mundo de la imagen molecular. Gracias a la confianza que has mostrado en mi durante todo este tiempo, he descubierto de lo que soy capaz. Para mí no solo has sido un jefe, sino también un mentor. Moltes gràcies.

Agradecer también al Dr. Sergio Moya, ya que gracias a él he podido realizar esta tesis doctoral y he podido formar parte de diferentes proyectos de colaboración.

Me gustaría aprovechar y agradecer a todo el consorcio que forma parte del proyecto de los nanomotores. Al Prof. Samuel Sánchez y todo su equipo por dejarme formar parte de este maravilloso proyecto, y enviarme todas las muestras que he necesitado. A la Prof. Esther Julián y su grupo de investigación, por enseñarnos y ayudarnos con todo lo necesario. Ha sido fantástico poder ver cómo empezó el proyecto y en lo que se ha convertido.

Esta tesis no solo ha implicado un enorme crecimiento científico sino también personal, y muchas personas han contribuido a ello. Agradecer a la Dra. Vanessa Gómez-Vallejo por su apoyo durante toda la tesis y ayudarme en todo lo posible. A la Plataforma de Radioquímica, en la que he pasado muchísimas horas durante estos cuatro años, especialmente a Víctor y Aitor. No sé qué hubiera hecho sin vosotros, gracias por vuestra paciencia e infinita ayuda, sé que no siempre es fácil contener este torbellino de nervios. Al Dr. Unai Cossío por estar siempre que se le necesita y por todos los buenos consejos que me has dado durante este camino. También agradecer a las Plataformas de Animalario y Resonancia Magnética por todo el soporte ofrecido.

Agradecer a todos los miembros, actuales y anteriores, del grupo de Radioquímica e Imagen Nuclear, ya que ha sido un placer trabajar y compartir todo este tiempo juntos. A la que llamamos Muchitanga de Radioquímica, por todas las risas y momentos vividos, pero sobre todo a mis neskitas (Ana, Pilar y Rossana) por el apoyo mutuo y los recuerdos imborrables que hemos creado. He tenido una suerte infinita de coincidir con vosotras.

Después de tantos años en Donosti, he podido conocer a muchísimas personas que de alguna forma han contribuido a esta experiencia. Especialmente me gustaría agradecer a Leire, porque a veces sólo hace falta un paseo con helado para poder desconectar, y seguir con más ganas que nunca.

A la que ha sido mi familia durante este tiempo en Donosti, Inés, Laura, Anna y después Rocío. Nuestro palacete ha sido el hogar perfecto cuando he echado de menos el mío. No tendría suficientes líneas para poder describir todo lo que hemos vivido ahí dentro, pero lo que, sí que tengo claro, es que no he podido tener más suerte de compartirlo con vosotras. Muchísimas gracias por todo el apoyo, el cariño y sobre todo las risas, que han sido curativas. Y Laura a ti, gracias por estar conmigo contra todo, eres sin ninguna duda, lo más bonito que me llevo de Donosti.

Agrair als que han estat amb mi abans de tot això, als del màster perquè l'últim sopar mai arribi. A les de sempre, tornar a Vinaròs sempre significa casa i més si es per desconnectar amb vosaltres. Gràcies a Inés, per compartir juntes el que ha significat Donosti i ser un pilar fonamental en aquesta etapa. A Júlia, perquè no se pot ser més artista que tu, gràcies per aquesta magnifica portada.

Però sobretot gràcies a tu, Jaume. Aquesta tesi significa tantes coses, però la més important és que el nostre camí comença a partir d'aquí.

Per últim als que són el meu suport constant, la meva família. Sense vosaltres tot això no seria possible. Gràcies per creure en mi i estar al meu costat a la distancia que sigui i en qualsevol moment. Mamà i papà, no he pogut tindre uns millors referents, aquesta tesi està totalment dedicada a vosaltres.